Journal
International I J M E of Modern
Engineering
WWW.IJME.US
Print ISSN: 2157-8052
Online ISSN: 1930-6628

INTERNATIONAL JOURNAL OF MODERN ENGINEERING

Spring / Summer 2013
Volume 13, Number 2

The Leading Journal of Engineering, Applied Science and Technology

Industrial

Electronics

Biomedical

Civil

Aerospace

Computer

Electrical

Chemical

Mechanical

ENGINEERING

THE LEADING JOURNAL OF ENGINEERING, APPLIED SCIENCE, AND TECHNOLOGY

Print ISSN: 2157-8052
Online ISSN: 1930-6628

www.ijme.us

www.iajc.org

INTERNATIONAL JOURNAL OF MODERN ENGINEERING

ABOUT IJME:

- IJME was established in 2000 and is the first and official flagship journal of the International Association of Journal and Conferences (IAJC).
- IJME is a high-quality, independent journal steered by a distinguished board of directors and supported by an international review board representing many well-known universities, colleges and corporations in the U.S. and abroad.
- IJME has an impact factor of **1.63**, placing it among the top 100 engineering journals worldwide, and is the #1 visited engineering journal website (according to the National Science Digital Library).

OTHER IAJC JOURNALS:

- The International Journal of Engineering Research and Innovation (IJERI)
  For more information visit www.ijeri.org
- The Technology Interface International Journal (TIIJ).
  For more information visit www.tiij.org

IJME SUBMISSIONS:

- Manuscripts should be sent electronically to the manuscript editor, Dr. Philip Weinsier, at philipw@bgsu.edu.

  For submission guidelines visit
  www.ijme.us/submissions

TO JOIN THE REVIEW BOARD:

- Contact the chair of the International Review Board, Dr. Philip Weinsier, at philipw@bgsu.edu.

  For more information visit
  www.ijme.us/ijme_editorial.htm

INDEXING ORGANIZATIONS:

- IJME is currently indexed by 22 agencies. For a complete listing, please visit us at www.ijme.us.

Contact us:

Mark Rajai, Ph.D.

Editor-in-Chief
California State University-Northridge
College of Engineering and Computer Science
Room: JD 4510
Northridge, CA 91330
Office: (818) 677-5003
Email: mrajai@csun.edu

www.tiij.org

www.ijeri.org

INTERNATIONAL JOURNAL OF MODERN ENGINEERING

The INTERNATIONAL JOURNAL OF MODERN ENGINEERING (IJME) is an independent, not-for-profit publication, which aims to provide the engineering community with a resource and forum for scholarly expression and reflection.

IJME is published twice annually (Fall and Spring issues) and includes peer-reviewed articles, book and software reviews, editorials, and commentary that contribute to our understanding of the issues, problems, and research associated with engineering and related fields. The journal encourages the submission of manuscripts from private, public, and academic sectors. The views expressed are those of the authors and do not necessarily reflect the opinions of IJME or its editors.

EDITORIAL OFFICE:

Mark Rajai, Ph.D.
Editor-in-Chief
Office: (818) 677-2167
Email: ijmeeditor@iajc.org
Dept. of Manufacturing Systems Engineering & Management
California State University-Northridge
18111Nordhoff Street
Northridge, CA 91330-8332

THE INTERNATIONAL JOURNAL OF MODERN ENGINEERING EDITORS

TABLE OF CONTENTS

IN THIS ISSUE (P.78): VISION AND VISUAL PERCEPTION

Philip Weinsier, IJME Manuscript Editor

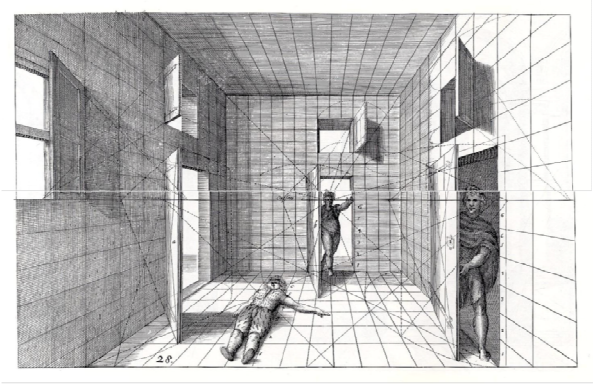

Perspective Diminution and Foreshortening
(Vredeman de Vries, J. (1968). *Perspective*. Dover Publications)

Having taught a few courses in mechanical design many years ago, I found this article particularly interesting as it provides both technical content and a connection to subconscious learning and a bit of history pertaining to 2D and 3D vision and media. I also find fascinating being able to learn about the ways our senses interpret our surroundings. Lest you think that this is only a fun article to read, keep in mind that understanding perspective analysis of distortion—including factors of diminution and foreshortening, depth calculation and inference—is important in the fields of machine vision, unmanned vehicles and robotics.

If our ultimate, if only short-sighted (I couldn't help the pun), goal is to give vision to machines, then it behooves us to evaluate both the capabilities our machines—including robots—will need to have, and our technological capabilities in order to determine if, in fact, we are able to re-create in our machines a real ability to "see". And since not all industrial applications require machines with the same capabilities, for the sake of argument let us assume that we wish to develop the most vision-capable machine possible.

Before we are able to think about creating real vision (3D perception) for machines, we need to take stock of what we know about our own, human capabilities. Humans are able to perceive the spatial relationship between objects even though we really only see in 2D; that is, we have depth perception, also called 3D perception. In order to accomplish this amazing task, we have to consider the fact that we have two eyes for providing slightly separate images; this is called *stereoscopic* or *binocular vision*, which helps us distinguish objects that are relatively close to us.

Next are *accommodation* and *size familiarity*, two tools necessary for determining how far away an object is and being able to distinguish between objects at the same distance. Accommodation is where the lenses in your eyes physically change shape in order to provide you with information about how far away an object is. Size familiarity tells us that if we know the approximate size of an object, we can determine about how far away it is. This is also useful when comparing objects at the same distance but with different sizes. In cases where objects are moving and have to be physically approached and picked by a machine, it will be necessary to consider additional tools such as *parallax*. Here, closer objects appear to move more than distant ones. At the risk of stating the obvious, these are all tools necessary for machine vision. So can we, then, just take this knowledge and build perfect vision into our machines? Probably not (yet), as no one has been able to simulate all of these and the many other tools needed for accurate and conclusive decision making.

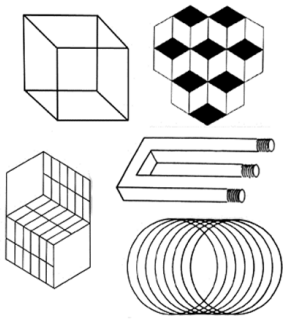

Just because we might be able to define and build such tools into our machines, it does not necessarily translate into accuracy. Consider *depth ambiguity*, where fixating on an object or image causes a spontaneous depth reversal. Again, this is a case where your mind tries to add depth to a 2D image. Look at the classic images shown here and you'll see what I mean. And though this might be fun for us as humans, it could be disastrous for a machine or robot, especially if it cannot consistently come to the same conclusion about similar objects or parts.

Artists are also able to take advantage of depth perception occurring in the brain (as opposed to the eye). Another classic image shown here is from Adelbert Ames' famous 1946 room (based on the ideas of L. Hermann). You can probably guess that the children are really the same height and that the lines of the room are distorted in order to trick your mind.

Editorial Review Board Members

Listed here are the members of the IAJC International Review Board, who devoted countless hours to the review of the many manuscripts that were submitted for publication. Manuscript reviews require insight into the content, technical expertise related to the subject matter, and a professional background in statistical tools and measures. Furthermore, revised manuscripts typically are returned to the same reviewers for a second review, as they already have an intimate knowledge of the work. So I would like to take this opportunity to thank all of the members of the review board.

As we continually strive to improve upon our conferences, we are seeking dedicated individuals to join us on the planning committee for the next conference—tentatively scheduled for 2014. Please watch for updates on our website (**www.IAJC.org**) and contact us anytime with comments, concerns or suggestions.

If you are interested in becoming a member of the IAJC International Review Board, send me (Philip Weinsier, IAJC/IRB Chair, philipw@bgsu.edu) an email to that effect. Review Board members review manuscripts in their areas of expertise for all three of our IAJC journals—IJME (the International Journal of Modern Engineering), IJERI (the International Journal of Engineering Research and Innovation) and TIIJ (the Technology Interface International Journal)—as well as papers submitted to the IAJC conferences.

Isaac Chang	Cal Poly State University SLO (CA)
Michael Coffman	Southern Illinois U-Carbondale (IL)
Brad Deken	Southeast Missouri State U. (MO)
David Domermuth	Appalachian State University (NC)
Mehran Elahi	Elizabeth City State University NC)
Ahmed Elsawy	Tennessee Tech University (TN)
Morteza Firouzi	University Techn. (MALAYSIA)
Rod Flanigan	Univ of Nebraska/Kearney (NE)
Nitish Gupta	Bhagwan Parshuram (INDIA)
Mohsen Hamidi	North Dakota State University (ND)
Bernd Haupt	Penn State University (PA)
Youcef Himri	Safety Eng. Sonelgaz (ALGERIA)
Dave Hunter	Western Illinois University (IL)
Pete Hylton	Indiana University Purdue (IN)
Reza Karim	North Dakota State University (ND)
Satish Ketkar	Wayne State University (MI)
Doug Koch	Southeast Missouri State U. (MO)
Ronald Land	Penn State University (PA)
Shiyoung Lee	Penn State University Berks (PA)
Chao Li	Florida A&M University (FL)
Dale Litwhiler	Penn State University (PA)
Guoxiang Liu	University of North Dakota (ND)
G.H. Massiha	University of Louisiana (LA)
Sam Mryyan	Excelsior College (NY)
Arun Nambiar	California State U. Fresno (CA)
Hamed Niroumand	Universiti Teknologi (MALAYSIA)
Reynaldo Pablo	Indiana Univ-Purdue Univ. (IN)
Jose Pena	Purdue University Calumet (IN)
Karl Perusich	Purdue University (IN)
John Rajadas	Arizona State University (AZ)
Ahmad Sleiti	UNC-Charlotte (NC)
Abram Walton	Purdue University (IN)
Haoyu Wang	Central Connecticut State U. (CT)
Liangmo Wang	Nanjing U. Science&Tech (CHINA)
Pao-Chiang Yuan	Jackson State University (MS)

DESIGN OF AN APPARATUS TO DETECT SMALL CHANGES IN THE MASS OF ROTATIONAL MACHINE COMPONENTS

Jonathan R. A. Maier, Clemson University; M. Laine Mears, Clemson University; Joshua D. Summers, Clemson University

Abstract

In this study, an apparatus was designed to detect changes on the order of grams in the mass of test samples subject to accelerations approaching 275g. The apparatus incorporated a surface speedometer, displacement transducer and on-board data-logging device in order to correlate mass loss events with changes in rotational speed and acceleration. An accessory was also designed to allow for on-board video recording to validate the findings and to better understand the mechanics of mass loss events. Such mass loss events are of interest for high-speed rotating machinery (e.g., manufacturing equipment, turbine rotors and automotive drivetrains), where material can build up and be dislodged, or other mass loss events can occur that currently cannot be measured directly. Results of such a design will allow for identification of mass loss in service for improved equipment diagnostics and control.

Motivation: Measurement of Mass Loss Events in Rotating Machinery

Mitigation of Safety Risks

Rotating machinery, including industrial machines, automobiles, aircraft turbines, etc., pose a serious safety hazard. According to the U.S. Department of Labor Bureau of Labor Statistics, 458 people were killed in the United States by machinery in the year 2005. This is 8% of the 5,743 total fatal occupational injuries for that year. Of the 458 deaths involving machinery, 105 involved some kind of rotating machinery [1]. Meanwhile, the National Highway Traffic Safety Administration (NHTSA) estimates that about 400 fatalities were the result of tire failures between the years 1994 and 2004, or an average of about 40 tire-failure-related deaths per year [2]. The Bureau of Labor Statistics also reports that between the years 1995 and 2002, 459 people were killed in helicopter-related incidents. About 2% of these deaths involved the decedent being struck by the rotating helicopter blades [3]. Loss of turbine blades in aircraft engines is an additional source of fatalities. For example, flight GA865 in 1996 aborted its take-off attempt after a turbine blade separated from one of the three engines. The resulting crash killed 3 of the 260 passengers on-board [4].

High-speed rotating machinery is commonplace in manufacturing, power generation and transportation. The high rotational speeds induce high centripetal acceleration, particularly at larger radii. As the centripetal acceleration increases with speed, so does the force necessary to hold anything attached to the equipment. Failure to retain screws, rivets, coatings or, in particular, debris can lead to rotational imbalance and equipment failure. Moreover, the loss of objects at speed poses a safety risk from the projectile motion of the ejecta.

Difficulties in Measuring Mass Loss on Rotating Machinery

Observing rotating machinery from a fixed standpoint is difficult as the speed of rotating machinery quickly outpaces video speed and capabilities (e.g., trying to film the tips of helicopter blades), and protective enclosures often obscure a direct view of equipment. The observation of mass loss events from high-speed rotating machinery *in situ* is very difficult for a number of reasons. Detection equipment itself, if mounted to the rotating element, will tend to cause imbalance (such as sensors on a turbine blade) and, therefore, is difficult to attach safely to equipment. If detection equipment is attached, then data must be recorded on the rotating machine since wires cannot be connected to a stationary data logger without twisting the wires or introducing electrical noise and wear through a slip coupling. Wireless transmission is complicated by the electromagnetic effects induced by the rotation of antennae and large power sources typical of such equipment. On-board data logging cannot involve moving parts (such as a hard drive or tape heads) since the large centripetal accelerations would cause these parts to malfunction.

Fortunately, recent advances in data-logging capability, particularly involving solid-state memory, do not have any moving parts and, thus, are ideally suited for recording on-board a dynamically moving machine. A test apparatus was

designed that incorporated commercially available data-logging to solid-state memory, and a displacement transducer to record mass loss events. The apparatus provides for on-board data collection and video recording at much lower cost compared to conventional approaches to outfitting a machine in service.

The conventional approach to identifying failure is to measure vibrations in the stationary part of the machine (e.g., the mounts) and to correlate anomalies in the vibrations to some reference model or signature of "normal" operation. In this way, imbalances can be potentially detected and failures—such as a cracked shaft, parts rubbing, worn bearings, etc.—diagnosed. However, expert knowledge is needed to correlate vibration data with the various causes of mechanical failure [5]. Specifically, a challenge to identification techniques is the excitation of the rotating structure where it is not easy to access the rotor to measure the forces.

In response to the urgency of studying rotating machinery, and in light of the problems inherent in the conventional approach, the aim of this design was to produce a dedicated apparatus on which mass loss events on the order of single grams could be detected and recorded from individual parts affixed and spun at speeds sufficient to achieve centripetal accelerations on the order of hundreds of g's. The means for recording the resulting data are discussed in subsequent sections.

Design Approach

A project sponsor presented the design team with the need for a machine capable of detecting mass loss events on the order of single grams at rotational accelerations of up to 274g. Additional constraints pertained to the accommodation of proprietary test samples, as well as the safety and location of the machine. Critical design constraints and criteria are shown in Table 1.

The design phase of the project lasted four months and included requirements evaluation, technology assessment and preliminary simulations, candidate design development, a Preliminary Design Review (PDR), detail design proposal with integrated subsystems, development of testing protocols and a Comprehensive Design Review (CDR). The fabrication phase of the project lasted another four months and included ordering components, fabricating the system, control design, programming and calibration procedures, initial functional testing and prototype demonstration to the project sponsor. The validation phase of the project lasted a final four months and included statistical Design of Experiments (DoE), validation testing using proprietary test samples, performance evaluation, repeatability and reproducibility characterization and training of operating personnel.

Table 1. Design Constraints and Criteria

Constraints	Criteria
Test samples will have mass of 1.5 kg	Repeatability of tests
Test samples must be held at a radial distance of 0.4 meters	Ability to test different sample geometries
Mass loss events on the order of single grams must be detected	Ability to test samples under different physical conditions
Voids created in the sample by loss of mass on the order of single grams must be detected	Cost of machine
Maximum centripetal acceleration encountered by the samples must be 274g	Safety of machine operation

Early in the design phase, free-body diagrams of the sample and mass loss events were drawn (see Figure 1). The free body diagram shows a hypothetical part before it is released from the rotating sample. The forces shown in the free body diagram act to hold the particle to the sample and to push it out of the sample. The forces acting to hold the particle in the sample (i.e., acting to the right in Figure 1) are chemical or mechanical bonding between the particle and sample, $F_{bonding}$, spring action from two or more sides if the particle is wedged, F_{spring}, friction force between the particle and the sample, $F_{friction}$, and suction created by any trapped air between the particle and the sample, F_{air}. The forces acting to push the particle out of the sample (i.e., acting to the left in Figure 1) are centrifugal effects, F_{cent}, punch from the sample flexing as it rotates, F_{punch}, and gravity when the sample is facing downward, $F_{gravity}$.

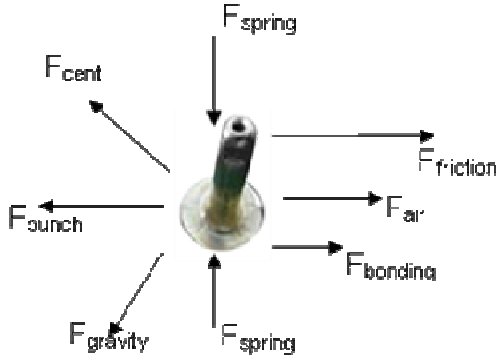

Figure 1. Free-Body Diagram of Mass Events

Continuing in the design phase, a systematic engineering design process was followed [6]. In particular, a high-level functional model of the prototype system was generated (see Figure 2), and system concepts were explored using a morphological matrix (see Table 2).

Feasible system concepts were discussed during the PDR leading to the selection of the final concept for prototype development. In particular, it was decided that the sample would be attached to the machine using a clamping assembly that would clamp on to geometrical features embedded in each sample. The sacrificial mass was to be loaded in discrete batches by hand. The rotational movement of the sample was to be accomplished through accelerating up through multiple rotations rather than a single rotation or by linear motion. The forces were to be measured directly using a displacement transducer as well as indirectly through video recording. Voids created in the sample as a result of testing were to be measured by weighing the sample before and after each test.

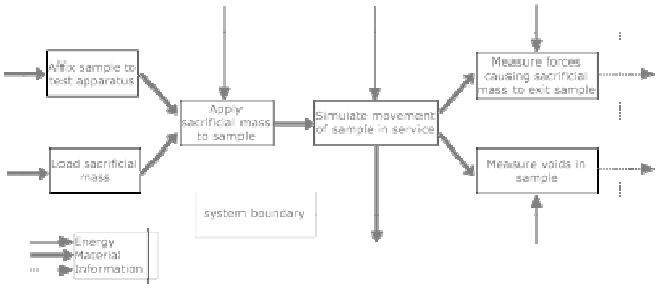

Figure 2. System Functional Diagram

Following the PDR, solid models were developed using computer-aided-design (CAD) software and the details of the prototype design were discussed at the CDR prior to prototype fabrication and validation. Details of various aspects of the prototype are described in subsequent sections, including how data displacement transducer data and video data are recorded on board the rotating machine, the primary sensing strategy involving the displacement transducer and additional sensing capabilities, the control strategy for achieving specific rotational speeds, and how the rotating machine is balanced.

Table 2. Morphological Matrix. Shaded Concepts Were Chosen for Prototype Development

Functions	**Solution Concepts**								
Affix sample to test apparatus	Apply normal force to top	Radially	Clamps	Adhesives	Screws / bolts	Suction pressure	Strings / Rubber bands / straps	Embedded feature in sample	Magnetic
Load sacrificial mass	Pan (discrete)	In a track / conveyor (continuous)	In a bottle						
Apply sacrificial mass to sample	Raise pan vertically	Conveyor belt	Spray	Move pan horizontally	Move sample vertically	Pack by hand			
Simulate movement of sample in service	Rotate sample through multiple rotations	Rotate sample through one rotation	Rotate sample through partial rotation	Radial or linear movement to impact a stop	Deflect sample by applying simulated road	Deflect sample directly with actuators			
Measure forces causing sacrificial mass to exit sample	Spring scales	Strain gauges / displacement transducers	Load cells / force transducers	Indirectly through measuring velocity optically / radar / ultrasonic / x-ray / etc.	Accelerometers	Rotary encoder	Sensors (nano) in sacrificial mass	Sensors (nano) in sample	Measure embedded traceable particles (metal / radioactive / etc.)
Measure voids in sample	Measure weight after packing and then after movement	Calculate void indirectly based on forces and density of sacrificial mass	Measure directly volume / height of mud between grooves	Directly through optically / radar / ultrasonic / x-ray / etc.	Measure traceable particles (metal / radioactive / etc.) embedded in mud and / or tire				

Similar prototype machine designs have recently been reported in the literature, including the design of a gripper with a spherical parallelogram mechanism [7], the design and prototyping of a partially decoupled 4-DOF 3T1R parallel manipulator with high-load carrying capacity [8], and the design of a microrobotic wrist for needle laparoscopic surgery [9]. Similar to the design of these mechanisms, the design of the apparatus to detect small changes in mass of machines at high rotational speeds described in this paper serves to fulfill a critical industrial need.

System Overview

The system designed and built in this study is illustrated in Figure 3. This system generally is composed of a test-sample mounting fixture, a blast shield for personnel and equipment protection, a high-resolution camera for event visualization, a data logger and a motor-control system. The sensing and control systems were of particular interest in this study and are discussed in subsequent sections.

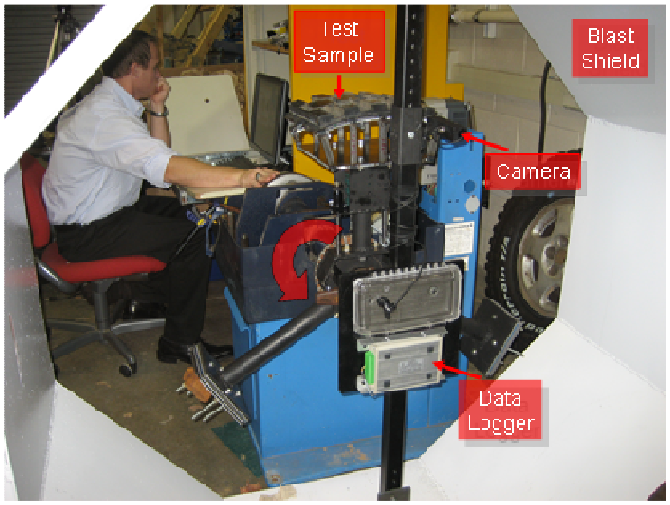

Figure 3. System Physical Architecture

The test sample fixture is a key mechanical element in this system (Figure 4).

The clamping assembly includes the surface on which samples may be placed from which a fly-off event will be measured. This clamping assembly is connected to a system of roller guides to allow for radial extension that is force controlled with an internal compression spring. Further, two balancing arms are included to ensure that the loads on the motor and shaft system are continuous. Dimensions for the system were redacted to adhere to the proprietary wishes of the sponsoring organization.

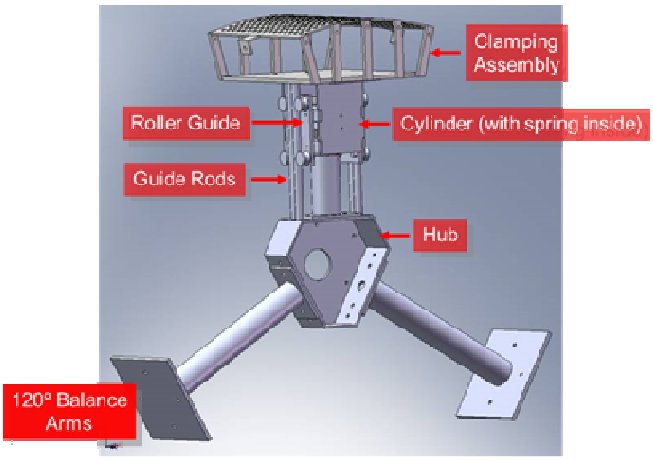

Figure 4. Fixture Assembly

The next section explains the data-logging challenges and solutions integrated into this system. The following section presents the video recording strategy employed. Finally, the sensing and control strategies necessary to realize this system are explained.

Recording Data on a Rotating Machine

Data loggers such as hard disk drives and tape drives that rely on moving parts will fail in situations where they will suffer shock loading or the similar effects of hundreds of g's of centripetal acceleration. A recent finite element analysis of hard disk drives by Lin [10] found that accelerations as low as 260g's will cause physical damage at the interface between the rotating plates and the fixed sliders.

The advent of flash memory in the last decade has revolutionized memory storage on a wide range of platforms including cellular phones, digital cameras, hand-held computers and even household thermostats [11]. Robust yet inexpensive high-speed data loggers are now available which are capable of operating on low-voltage battery power and record onto standard flash memory cards. Such data loggers are immune to the effects of centripetal acceleration since they do not have any moving parts. Similar data loggers are now commonly used in environments where high-voltage power is not available and harsh conditions, such as for data logging on board race cars, are present. For the prototype machine, the Dataq DI-710 with data sampling speeds of up to 14.4 KHz and a high-speed Secure Digital flash memory card with 1 GB capacity was selected. The data logger was mounted near the center of the testing apparatus in order to minimize the forces on the mounting hardware and wire connections.

Recording Video on a Rotating Machine

In addition to the ability to record mass loss events using the data logger described in the previous section, video recording can yield additional information relevant to the mechanics of how mass loss events occur. Frame-by-frame analysis can reveal the originating location and trajectory of ejecta and events precipitating mass loss, such as crack propagation or initial plastic failure of components. Video recorded on-board the rotating machinery enables superior image capture capability compared to video recorded from a stationary location, because the configuration is not as sensitive to sampling rate, and rotation of the machinery itself does not obscure the view of the component of interest, which appears fixed in the frame.

However, recording video data on board the rotating machine poses the same challenges as recording data from the displacement transducer—namely, the recording must be on solid-state memory (no moving parts) and must operate on low-voltage battery power. Whereas most video recorders, whether analog or digital, utilize magnetic tapes or hard disk drives, digital video recorders (DVRs) have recently been introduced that compress the video signal in real time and record onto solid-state flash memory. When paired with a fixed-lens digital CCD camera, the DVR system contains no moving parts and is well suited to video recording on board the rotating machine. This type of solid-state recording setup has found popularity with sporting enthusiasts, for example, in sturdy helmet cameras that can record "first person" action during motorcycle racing, open-cockpit auto racing, and even sky-diving, kayaking and skiing. These systems are robust enough to withstand not only the rigors of racing but also high-acceleration impact events such as crashes.

For the prototype machine in this study, a Sony bullet-style camera with 560-line resolution paired with a mini DVR that records at 320x240 resolution and 30 frames per second was chosen. Both the camera and DVR were mounted within protective enclosures. Both devices ran off of the same battery pack that powered the separate Dataq data logger.

Sensing Strategies

Primary Sensing Strategy

The machine was designed to detect changes in mass of a test sample while the sample rotates at speed. The on-board data logger discussed above provides a means for recording electrical signals. The choice was, therefore, for a transducer that would detect mass loss events and convert those events to an electrical signal for the data logger to record. The simplest concept for the apparatus was to have a rigid arm with a strain gauge attached that would be able to resolve changes in the axial deflection of the arm as individual mass loss events occur. However, the arm would have to be very thin in order to get significant strain for mass loss events on the order of single grams.

As noted in Table 1, the test sample under study had a mass of 1.5 kg, was held at a radial distance of 0.4 meters, and the machine had to detect a change in mass on the order of 1 gram at a maximum centripetal acceleration of 274g. The centrifugal force on the sample at maximum speed can be calculated as follows, taking 300g as a worst-case scenario rather than 274g:

$$a = F / m \tag{1}$$

$$300 \cdot 9.81 = F / 1.5 \tag{2}$$

$$F = 300 \cdot 9.81 \cdot 1.5 \tag{3}$$

$$F = 4414.5 \text{ N} \tag{4}$$

where the maximum radial speed is:

$$F = m \cdot \omega^2 \cdot r \tag{5}$$

$$4414.5 = 1.5 \cdot \omega^2 \cdot 0.4 \tag{6}$$

$$\omega^2 = 4414.5 / (1.5 \cdot 0.4) \tag{7}$$

$$\omega^2 = 7357.5 \tag{8}$$

$$\omega = 85.8 \text{ radians/second} \tag{9}$$

and the change in force for the loss of one gram is:

$$F = m \cdot \omega^2 \cdot r \tag{10}$$

$$F = 0.001 \cdot 85.8^2 \cdot 0.4 \tag{11}$$

$$F = 2.94 \text{ N} \tag{12}$$

A typical strain gauge will not detect changes in strain ε below 0.01%, or ε=0.0001. For aluminum, with a Young's modulus of $E = 69 \cdot 10^9$ N/m^2, the cross section of the arm, A_{xc}, can be calculated to detect events at maximum radial speed, ω:

$$\varepsilon = F / (A_{xc} \cdot E) \tag{13}$$

$$0.0001 = 2.94 / (A_{xc} \cdot 69 \cdot 10^{9}) \tag{14}$$

$$A_{xc} = 2.94 / (0.0001 \cdot 69 \cdot 10^{9}) \tag{15}$$

$$A_{xc} = 4.26 \cdot 10^{-7} \text{ m}^2 \tag{16}$$

$$A_{xc} = 0.426 \text{ mm}^2 \tag{17}$$

In order to support a strain gauge one centimeter wide, the arm would only be 0.04 mm thick, far too thin to be structurally feasible. To detect mass loss events at lower speeds would require the arm to be thinner still. The conclusion is that a strain gauge acting alone is not sensitive enough to detect mass loss events on the order of single grams.

Consequently, a spring system to mechanically amplify length changes was developed. A compression spring rather than an extension spring was selected for two reasons. First, compression springs are available with shorter lengths and higher stiffness (in particular, die springs) than available extension springs. Second, if the machine is overloaded, a compression spring will fully compress and then act as a rigid cylinder, whereas an extension spring would over extend and potentially fail.

An overview of the chosen sensing strategy is shown in Figure 5. A computer workstation controls a motor which accelerates the apparatus up to speed. The test sample is held on a compression spring. When mass loss events occur, the decrease in the sprung mass causes the centrifugal force on the spring to decrease; the compression spring then extends (on the order of millimeters for mass loss events on the order of grams). A linear potentiometer acts as a displacement transducer, converting changes in the piston length of the potentiometer into changes in electrical resistance. A separate battery back supplies DC voltage to the linear potentiometer. The data logger finally records the difference in voltage across the linear potentiometer over time.

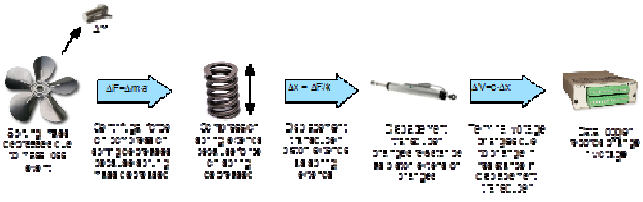

Figure 5. Working Principles in the Apparatus

The time at which events occurred can be extrapolated based on the sampling frequency set on the data logger. The rotational speed, and therefore centripetal acceleration, at which events occur can be inferred based on the speed profile supplied to the motor, or via a second speedometer channel recorded on the data logger. The use of recorded speedometer data is particularly helpful as the speed profile on the motor controller may not actually be achieved by the motor due to slip and friction losses. The data analysis can be performed in any commercially available analysis package such as Matlab, DaDisp or DIAdem.

Spring Selection

The dimensions of the spring must match the capabilities of the displacement transducer; however, another important consideration is that the spring stiffness must exceed the natural frequency of the sprung load. The sprung load consists of not only the test sample, but also the clamping apparatus necessary to hold it. The combined mass of the sprung load in the prototype was approximately 9 kg. The frequency of the machine at maximum speed is:

$$f = \text{rotational speed (Hz)} = \text{rotational speed (radians/second)} / (2\pi \text{ radians/rotation}) \tag{18}$$

$$f = 85.8 / (2\pi) \tag{19}$$

$$f = 13.7 \text{ Hz} \tag{20}$$

The minimum stiffness of the spring can then be calculated:

$$f_n = 0.5\pi\sqrt{k/m} \tag{21}$$

$$2 \cdot f_n = k / (4\pi 2m) \tag{22}$$

$$k = 4\pi^2 f_n^2 m \tag{23}$$

$$k = 4\pi^2 \cdot (13.7 \text{ rot/sec})^2 \cdot 9 \text{ kg} \tag{24}$$

$$k = 66687 \text{ kg/sec}^2 \tag{25}$$

$$k = 66687 \text{ N/m} = 381 \text{ pounds/inch} \tag{26}$$

To be above the natural frequency of the machine running at top speed, the spring must be stiffer than 381 pounds/inch. In addition, the spring must be able to carry the sprung load at maximum speed:

$$F = m \cdot a \tag{27}$$

$$F = 9 \text{ kg} \cdot 300 \cdot 9.81 \text{ m/sec}^2 \tag{28}$$

$$F = 26487 \text{ N} = 5954 \text{ pounds} \tag{29}$$

The current spring in use in the machine has a maximum load of 2,000 pounds and a spring rate of 2,900 pounds/inch. The current spring was, therefore, 7.6 times the stiffness necessary to be above the natural frequency of the system; however, it was undersized by about two thirds relative to the maximum load at speed. In the current test setup, it was presumed that much of the mass (which was artificially added to the test sample) will have dislodged by maximum speed, such that the spring would not need to carry the whole 5,954 pounds of maximum load. Using an undersized spring with respect to maximum load allows for greater resolution at lower rotational speeds.

To match the chosen spring, which has a maximum deflection of 23% of 3 inches overall height, which is 0.69 inches or 1.75 cm, a displacement transducer with 2.5 cm stroke length was selected. A linear motion potentiometer was chosen because they have essentially unlimited resolution. The effective resolution is limited only by the data logger which, for the Dataq DI710, is 14 bits.

Additional Sensing Capabilities

Besides the record of mass loss events captured on-board in the data logger, mass loss events can be detected by other means, both on-board and off-board the machine. On-board the machine, the video camera captures a video record of every particle that leaves the test sample within the field of view, within the resolution and frame rate capabilities of the camera. Off-board the machine, stationary video and audio capture is also possible, which is particularly effective in capturing the audible signature of ejecta hitting the safety shield, which is in place around the machine. Another means for detecting mass loss events is using the conventional approach, where sensors detect increasing vibration in the drive shaft. Sample data recorded using each sensing strategy are presented in the section on sample data.

Control Strategy

An industrial three-phase motor turns the prototype. The motor is controlled by a Telemechanique Altivar 71 motor drive. The motor drive can be deactivated manually using a shut-off switch. The motor drive is itself controlled by a computer running LabVIEW software and a proprietary motor-control software. Different motor states are actuated using a set of hardware relays which are switched on and off by the LabVIEW software through a National Instruments USB-6009 DAQ interface. In addition to spinning the prototype, the motor is also connected to a quadrature encoder and to piezo-electric sensors. The quadrature encoder signal and piezo-electric sensor signals are inputted to LabVIEW through the DAQ interface.

The LabVIEW software running on the computer presents the user with real-time speed data based on the quadrature encoder signal. The speed data are also stored to a data file which may be accessed and viewed after the test to see the details of the actual speed and behavior of the motor. Examining the actual motor behavior is important because while the control software may be programmed for any arbitrary speed profile, the motor has physical limitations such that it may not be able to fully achieve programmed accelerations, decelerations and set speeds.

The ability of the user to see in real-time the rotational speed of the prototype is important because, for safety reasons, the operator may not be in the same room as the prototype during a test; that is, the computer and operator may be located remotely. Thus, via the speedometer reading, the LabVIEW software allows the user to know when the test starts and when it has come to an end. In the case that there was an initial setting that was set incorrectly and the motor does not behave as the user intended, it will also show this and the user will then be able to make the appropriate changes to conduct another test with corrected settings. Also located on the front panel were “start” and “stop” buttons for beginning and, if necessary, prematurely ending a test. The LabVIEW program was designed to shut itself off after conducting the appropriate functions for any given test.

Also located in the LabVIEW block diagram were the controls for the relays that control the starting, stopping and other speed changes of the motor. The time for which the relays will change the output of the motor was controlled from the front panel when LabVIEW is running and can be set in milliseconds. Each change in relay state can be programmed for a corresponding change in step-wise or ramp acceleration (or deceleration) of the motor.

Balance Strategy

The sample was held at a radial distance from the center of the drive axle to increase the centripetal load. That load had to be balanced in order not to place large and potentially detrimental unbalancing forces on the machine which will ultimately cause fatigue and excessive vibration, both potential safety hazards.

Since mass will be lost from the sample during testing, unless the balance mass adjusts, the machine will have some amount of imbalance. In order to minimize complexity in the machine, a variable-balance mass was not integrated. Rather, two balance arms were placed at 120° from the in-

strumented arm, rather than one balance arm at 180° from the instrumented arm. The imbalance caused by mass loss events is thereby a smaller proportion with respect to two balance arms than it would be compared to a single balance arm.

The hub geometry necessary to accommodate one instrumented arm and two balance arms is fundamentally an equilateral triangle. However, in order to minimize the mass and stress risers of the hub, the three "points" of the triangle are truncated, resulting in a hexagonal design (Figure 6).

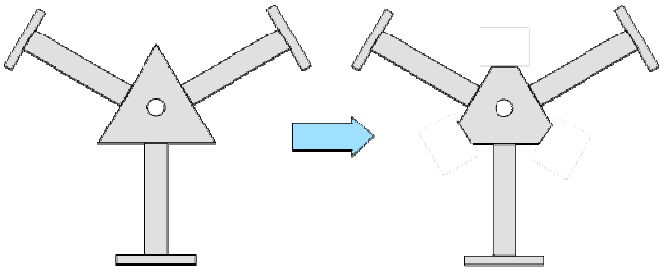

Figure 6. Triangular Hub Design versus Hexagonal Hub Design

Meanwhile, the video camera, which is held at a longer radial distance than the test sample, must also be balanced. Since the camera does not lose mass, it would not benefit from balance mass at 120°. Therefore the camera was held on a separate mount with balancing at 180°. The mount allows for the camera to move radially from 0.4 to 0.6 meters in order to provide for different video angles of the sample, from edge-on to nearly top-down showing the whole sample within the field of view. In the prototype, the data logger, digital video recorder and battery pack were mounted on a plate at the center of the camera arm. The finished prototype system is shown in Figure 7. The various components of the assembly shown in the images include the central hexagonal hub, balance arms, main cylinder with spring, roller guides and guide rods, and the clamping assembly holding the test sample. Note that the camera arm mounts to the central hexagonal hub. The physical prototype shown in Figure 7 is placed within a radially protective shield made of 6mm-thick steel.

Analysis Strategies

Analyzing Displacement Transducer Data

The principal challenge in the analysis of the data is to distinguish individual mass loss events. Ideally, mass loss events should appear as stepwise decreases in the displacement transducer data (highlighted by the red arrows in Figure 8).

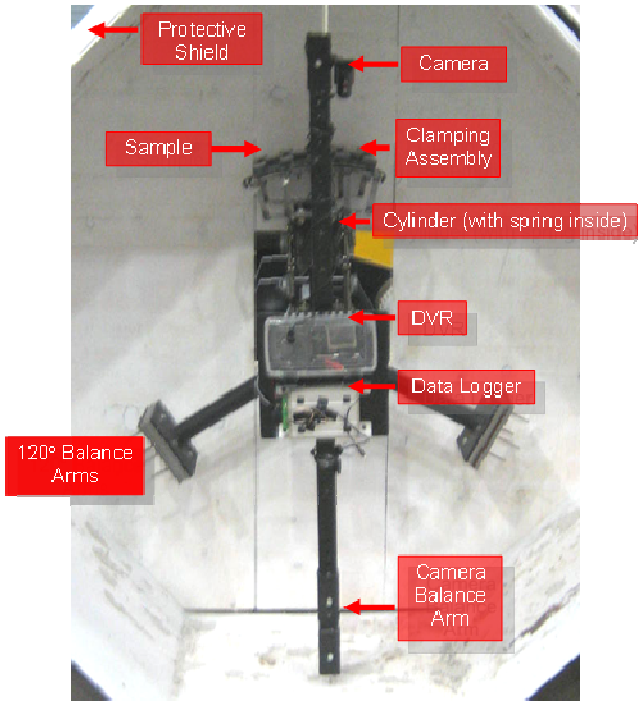

Figure 7. Physical Prototype

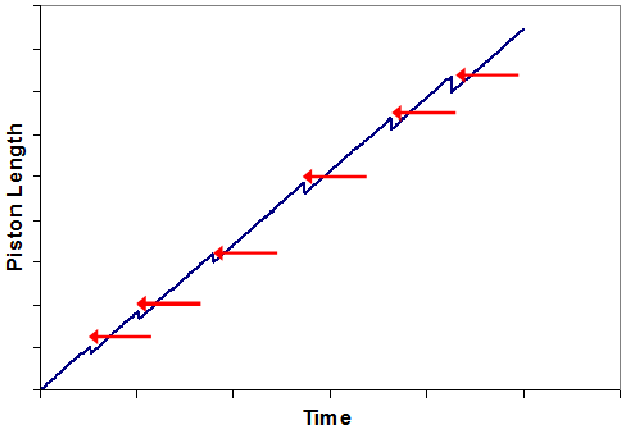

Figure 8. Theoretical Plot Showing Piston Length of the Displacement Transducer Versus Time for a Ramp Input to the Motor. Mass Loss Events Appear as Down-Steps

Several effects on the machine act to make the real data more noisy and mass loss events more difficult to distinguish. One such effect is gravity. Since the apparatus rotates in a vertical plane, directionality of the gravitational force affects the sensor readings. Fortunately, this is predictable at low speeds, and as the speed of the apparatus increases, the effect of the gravity force is proportionally smaller com-

pared to the centrifugal force. The effect of gravity can be removed from the data by calculating the gravity force and consequential displacement for the given rotation angle at any time. The angle of rotation is accurately synchronized with the angle at which the gravity force is calculated through the LabVIEW real-time engine.

Another effect is electrical noise. Since the data logger runs off battery power, which is not well conditioned, the signal through the displacement transducer exhibits noise, even when at rest (see Figure 9). The noise occurs at a higher frequency than either the gravity effect or the frequency of mass loss events, so the electrical noise can be effectively removed using a low-pass filter without significantly affecting sensing of mass loss events. Figure 10 shows the transducer data at rest filtered using a running average with n=398.

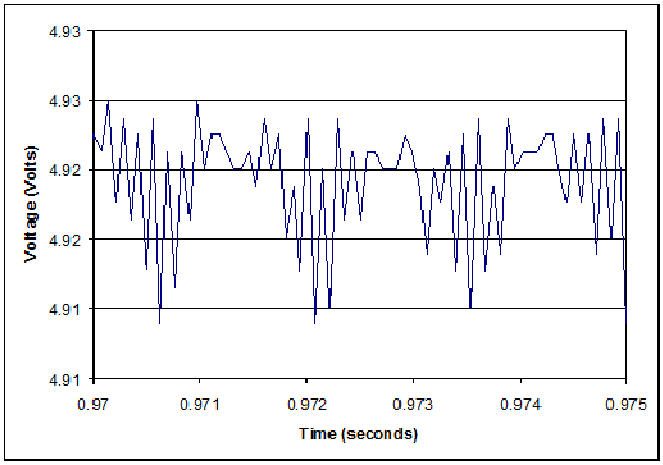

Figure 9. Transducer Signal at Rest (Unfiltered)

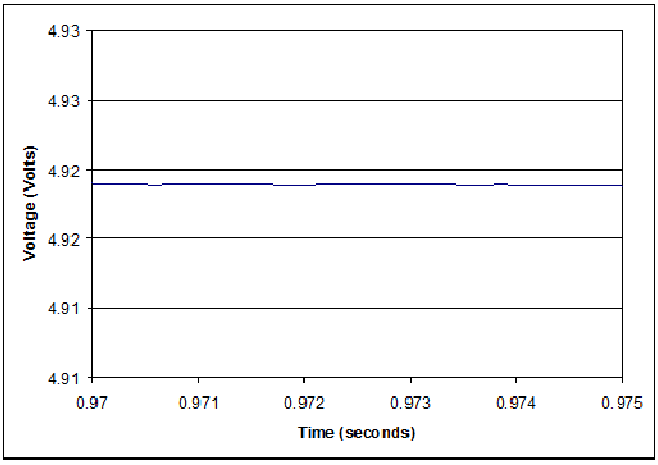

Figure 10. Transducer Signal at Rest (Filtered)

Friction and clearances in the moving components can also introduce noise into the data through excessive stick-slip phenomena. For this reason, precision roller guides were used in place of sliding linear guides, which helped to eliminate lateral movement and constrained the test sample more closely to move radially as the spring compressed and decompressed.

Smallest Mass Loss Event Discernible using Primary Sensing Strategy

Using the primary sensing strategy of the analog displacement transducer connected to the digital 14-bit data logger, and a range of displacement of 1.75 cm, and taking into account the manufacturer's specification of the data logger of a noise floor of 2 bits, changes in displacement must result in a change of at least 3 bits. The smallest detectable change in length of the displacement transducer is therefore:

$$(1.75\ \text{cm}/2^{14}\ \text{bits})\cdot 3\ \text{bits/event} = 0.000320\ \text{cm/event} \quad (30)$$

An event causing that change in length of the spring would be due to a change in force on the spring of:

$$F = k\cdot x \quad (31)$$

$$x = 0.000320\ \text{cm} = 0.000000320\ \text{m} \quad (32)$$

$$k = 2900\ \text{pounds/inch} = 508000\ \text{N/m} \quad (33)$$

$$F = 508000\cdot 0.000000320 = 0.163\ \text{N} \quad (34)$$

A change in centrifugal force of that magnitude at top speed would be due to a mass loss of:

$$F = m\cdot\omega^2\cdot r \quad (35)$$

$$m = F/(\omega^2\cdot r) \quad (36)$$

$$m = 0.163/(85.8^2\cdot 0.4) \quad (37)$$

$$m = 0.0000553\ \text{kg} = 0.055\ \text{g} \quad (38)$$

Alternately, one can compute the minimum speed at which a mass loss of 1 gram is detectable:

$$F = m\cdot\omega^2\cdot r \quad (39)$$

$$\omega = \sqrt{\frac{F}{m\cdot r}} \quad (40)$$

$$\omega = \sqrt{\frac{0.163}{0.001 \cdot 0.4}} \tag{41}$$

$$\omega = 20.2 \text{ radians / second} \tag{42}$$

For comparison, the equivalent tangential speed of the sample at the specified radius of 0.4 meters at a top radial speed of 85.8 radians/second is:

$$\frac{85.8 \text{ radians}}{\text{second}} \cdot \frac{1 \text{ revolution}}{2\pi \text{ radians}} \cdot \frac{2\pi \cdot 0.4 \text{ meters}}{1 \text{ revolution}} = 34.3 \frac{\text{meters}}{\text{second}} = 76.8 \frac{\text{miles}}{\text{hour}} \tag{43}$$

And, the equivalent tangential speed of the sample at the minimum speed of 20.2 radians/second necessary to detect a mass loss event of one gram is:

$$\frac{20.1 \text{ radians}}{\text{second}} \cdot \frac{1 \text{ revolution}}{2\pi \text{ radians}} \cdot \frac{2\pi \cdot 0.4 \text{ meters}}{1 \text{ revolution}} = 8.04 \frac{\text{meters}}{\text{second}} = 18.0 \frac{\text{miles}}{\text{hour}} \tag{44}$$

In order to distinguish mass loss events at lower speeds, a less stiff spring can be used; however, this will also decrease the highest speed at which the apparatus can be run before the spring fully compresses. Initial screening experiments can be used to determine the characteristic range of speeds over which mass loss events are expected to occur, and a suitable spring rate can be chosen.

Another practical consideration relating to the primary sensing strategy is the DC voltage range over which the data logger detects changes on any given channel. For example, if the data logger is configured for a range of 0-5 volts, then the DC voltage used to excite the displacement transducer must be carefully matched such that the actual range of displacement (in this case, from 0-1.75 cm) corresponds to a voltage change of 0-5 volts. Hence, the DC voltage used to supply the displacement transducer in order to maximize its resolution:

$$1.75 \text{ cm} / 5 \text{ V} = 2.5 \text{ cm / excitation V} \tag{45}$$

$$\text{excitation V} = 2.5 / (1.75 / 5) = 7.14 \text{ V} \tag{46}$$

The precise excitation voltage can be achieved using DC batteries and a simple voltage-divider circuit.

Alternate Analysis Strategies

As discussed above, the video camera captures a video record of every particle that leaves the test sample within the field of view. Frame-by-frame analysis of the video recording using, for example, the freely available VirtualDub software package reveals individual mass loss events. Correlating the time of each video frame with the recorded speed of the apparatus results in the speed and accelerations experienced during each mass loss event.

The smallest detectable mass loss event using this method is determined by the resolution of the video camera, distance from the sample and density of the ejecta. In the setup, the field of view at the depth of the sample in the video frame is approximately 33 cm wide by 25 cm high. The on-board DVR records at a resolution of 320x240 pixels. The effective resolution of the on-board video system is therefore:

$$\frac{33 \text{ cm} \cdot 25 \text{ cm}}{320 \text{ pixels} \cdot 240 \text{ pixels}} = 0.0107 \frac{\text{cm}^2}{\text{pixel}^2} \tag{47}$$

or about 1 mm per pixel in either direction.

Assuming ejecta density of 1 gram/cubic centimeter, the video setup is capable of detecting mass loss events three orders of magnitude smaller than the primary sensing strategy, and is not limited to any particular speed range. However, the frame rate of the video must be fast enough to capture mass loss events at a particular speed. The DVR in the setup records at 30 frames per second. If a particle of ejecta travels across half of the vertical video frame to be detectable, that is approximately a distance of 15 cm. The video speed of 30 frames per second means a particle of ejecta has 0.0333 seconds to be captured in a video frame. Therefore, if the particle is traveling at more than 15 cm/0.0333 second = 450 cm/second = 4.5 meters/second = 10 miles/hour, it will not be shown traveling in the video frame. At higher speeds, a mass loss event will only be discernible by the presence of the ejecta particle on the sample in one frame and its absence in an adjacent frame. Other principal drawbacks of the video analysis method include the time involved in frame-by-frame video analysis, and the possibility that an event may be occluded by another event in the video frame.

To augment the video analysis, audio data recorded off-board the apparatus can also be used to detect mass loss events. The smallest mass loss event discernible using this method depends on the rigidity of the surface on which the ejecta impacts, the rigidity of the ejecta itself, the noise produced by the apparatus and other ambient noise. Using a radial protective shield made of 6mm-thick steel around the machine, the system is able to distinguish mass loss events using this method. Applying a high-pass filter to the data (greater than the rotational speed of the machine) helps to reduce noise in the data. Limitations of this method include difficulty in synchronizing the audio data with the start of the machine rotation, the time lag between when ejecta leave the sample and impact the blast shield, inability to distinguish the position from which ejecta leave the sample,

inability to distinguish the sizes of individual particles of ejecta, and confounding of the signal by secondary impacts (ejecta striking the radial wall, then falling to strike again).

Sample Data

An interesting trend in data obtained using the primary sensing strategy is related to the mass loss from the sample over time. As mass is lost from the sample, the sprung mass decreases and, therefore, the amplitude of the oscillations caused by gravity decreases as the sample rotates around from pointing straight up to pointing straight down. This effect is shown graphically in Figure 11. The region where the amplitude of the oscillations decreases helps to identify the time interval during which the mass is being lost.

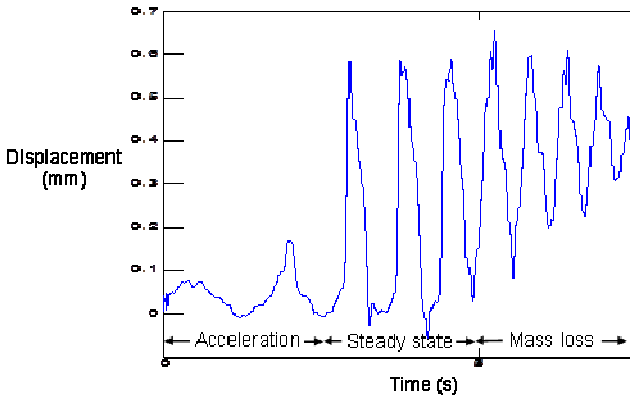

Figure 11. Sample Data from the Displacement Transducer Showing Change in Amplitude Induced by Mass Loss Events

Sample data obtained using the video analysis is shown in Table 3. The analysis proceeds from the frame number of a noticeable event, the time corresponding to that video frame, an estimate of the mass of the ejecta based on the size in the video frame, a running total of the accumulated mass loss over time, the computed tangential speed at which each event occurred, and computed force and acceleration experienced by each particle of ejecta. The same data are plotted versus time and versus tangential speed in Figure 12.

The plots in Figure 12 illustrate how most of the mass loss events occur over a narrow critical speed range where enough force is experienced by the ejecta to dislodge them from the test sample. Note that the smallest estimated particle of ejecta is 4.8 grams. Thus, the principle goal for the device, to detect mass loss events on the order of single grams from individual parts spinning at speeds sufficient to achieve centripetal accelerations on the order of hundreds of g's, has been achieved.

Table 3. Sample Data from Video Analysis

frame #	time (s):	mass estimate (g):	accumulated mass loss (g):	speed (mph):	total force (N):	force on chunk (N):	accel. (m/s^2):	accel. (g's):
254	8.47	0	0					
255	8.50	38.4	38.4	24.3	1787	8.93	233	23.7
263	8.77	4.8	43.2	24.5	1845	1.15	240	24.5
274	9.13	4.8	48.0	24.6	1927	1.20	251	25.6
278	9.27	4.8	52.8	24.7	1907	1.19	248	25.3
280	9.33	76.7	129.5	24.7	1989	19.88	259	26.4
281	9.37	9.6	139.1	24.7	1957	2.44	255	26.0
283	9.43	14.4	153.5	24.8	1951	3.47	241	24.6
284	9.47	38.4	191.9	24.8	1954	9.26	241	24.6
285	9.50	19.2	211.0	24.8	1904	4.76	248	25.3
286	9.53	76.7	287.7	24.8	1967	19.66	256	26.1
288	9.60	9.6	297.3	24.8	1981	2.47	258	26.3
291	9.70	38.4	335.7	24.8	1959	9.28	242	24.7
292	9.73	48.0	383.6	24.8	1899	11.86	247	25.2
293	9.77	9.6	399.2	24.8	1984	2.45	258	26.1
298	9.93	4.8	398.0	24.9	1867	1.17	243	24.8
305	10.17	4.8	402.8	24.9	1873	1.17	244	24.9
323	10.77	4.8	407.6	25	2035	1.27	265	27.0
327	10.90	4.8	412.4	25	1888	1.18	246	25.1
328	10.93	0.0	412.4					
	2.47 Total	412.4 Total	412.4 Total	24.8 Avg.	1909 Avg.		248.6 Avg.	25.3 Avg.

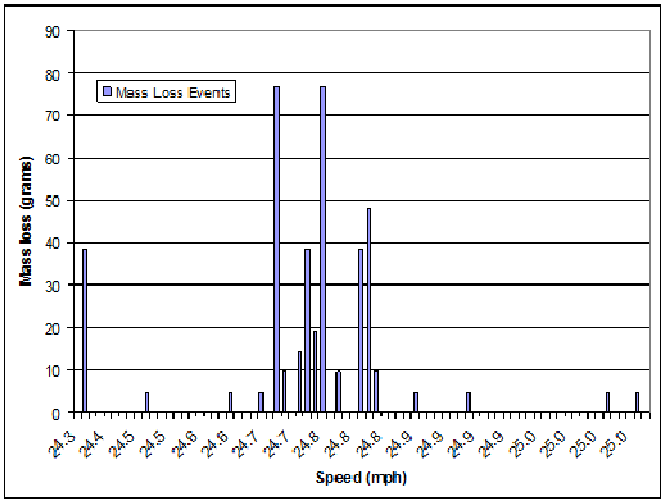

Figure 12. Mass Loss Events Based on Analysis of Video Data

Finally, a plot of the off-board audio data for one test is shown in Figure 13. A high-pass filter of 4,015 Hz was applied to the data using the freely available Audacity software package. Individual impacts of ejecta against the steel blast shield are clearly visible (highlighted with red arrows in Figure 13) in the data and correlate with the times of mass loss events recorded using the video analysis method.

Conclusion

The development of an apparatus and associated sensing strategies and analysis methods as reported in this paper allow test engineers to study the speeds, accelerations and forces at potentially dangerous mass loss events that occur on rotational machinery. While the video analysis produced the most useful data for the proprietary tests conducted,

given another situation, one of the other analysis strategies described may well produce more relevant data. The experimental apparatus has also been used to study the mechanics at the interface between various ejecta materials and different substrates, as the apparatus allows for experiments to be conducted at high acceleration levels in controlled laboratory conditions. Future work should include the application of the apparatus and analysis strategies to additional physical phenomena at high acceleration levels.

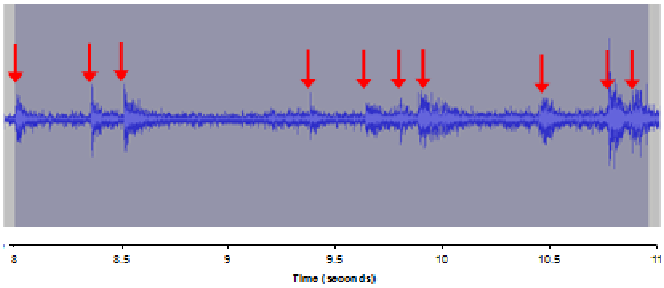

Figure 13. Processed Audio Signal from Off-Board Recording

References

[1] Bureau of Labor Statistics. (2006). Fatal occupational injuries by primary and secondary source of injury by major private industry sector. *Technical Report.* United States Department of Labor, pp. 1–17. Retrieved February 11, 2013, from http://www.bls.gov/iif/oshwc/cfoi/cftb0208.pdf.

[2] National Highway Traffic Safety Administration. (2007). Research Report to Congress on Tire Aging. *Technical Report.* NHTSA. Washington, DC.

[3] Pegula S. M. (2004). Fatal Occupational Injuries Involving Helicopters, 1995-2002. *Technical Report.* Bureau of Labor Statistics. Retrieved February 11, 2013, from http://www.bls.gov/opub/cwc/old/sh20041022ar01p1.asp.

[4] Takeuchi K. (1997) Aircraft Accident Investigation Report: Garuda Indonesia, Douglas DC-10-30, PK-GIE Fukuoda Airport. Aircraft Accident Investigation Commission, Technical Report, Tokyo, Japan.

[5] Nordmann R. (1994). Identification techniques in rotordynamics. Diagnostics of Rotating Machines in Power Plants: *Proceedings of the CISM/IFToMM Symposium*, October 27-29, 1993, Udine, Italy, Springer, p. 1.

[6] Pahl G., Beitz W., Wallace K., & Blessing, L. (2007). *Engineering Design: A Systematic Approach*, Springer-Verlag London Limited, London.

[7] Kocabas H. (2009). Gripper design with spherical parallelogram mechanism. *Journal of Mechanical Design*, 131 (7), .

[8] Arakelian V., & Guégan S. (2008). Design and prototyping of a partially decoupled 4-DOF 3T1R parallel manipulator with high-load carrying capacity. *Journal of Mechanical Design*, 130 (12), pp. 122301–122303.

[9] Zoppi M., Sieklicki W., & Molfino R. (2008). Design of a Microrobotic Wrist for Needle Laparoscopic Surgery. *Journal of Mechanical Design*, 130 (10), p. 102306.

[10] Lin C. (2002). Finite element analysis of a computer hard disk drive under shock. *Journal of Mechanical Design*, 124 (1), pp. 121–125.

[11] Yoshikawa K. (1999). Embedded flash memories-technology assessment and future. *VLSI Technology, Systems, and Applications, 1999. International Symposium on*, IEEE, (pp. 183–186).

Biographies

JONATHAN R. A. MAIER is a lecturer in General Engineering at Clemson University. He received his BS from Georgia Tech and his MS and PHD at Clemson University. His research is centered on affordance based design, establishing it as both an explicative theory for design and evolving design methods based on the theory. Dr. Maier may be reached at jmaier@clemson.edu.

M. LAINE MEARS is an Associate Professor of Automotive Engineering at Clemson University. He received his BS from Virginia Tech and his MS and PHD from Georgia Tech. His research interests include manufacturing process control. He is an NSF CAREER award recipient and his work has been funded by the US Army, DOE, NIST, and several automotive industry corporations. Dr. Mears may be reached at mears@clemson.edu.

JOSHUA D. SUMMERS is a Professor of Mechanical Engineering and a College IDEaS Named Professor at Clemson University. He received his BS and MS degrees from the University of Missouri and his PHD from Arizona State University. His research interests are centered on understanding the design process in order to develop new design enabling tools and methods. He may be reached at jsummer@clemson.edu.

THERMAL MODELING AND ANALYSIS OF AN ON-BOARD INTERNAL-COMBUSTION-ENGINE-BASED POWERTRAIN

Abdelraouf Mayyas, Arizona State University; Mohammad Omar, Clemson University; Pierluigi Pisu, Clemson University;
A. M. Kannan, Arizona State University

Abstract

In this study, the authors developed a three-dimensional (3D) thermal model of an internal-combustion-engine-propelled powertrain using a Finite Element (FE) analysis complemented with experimentally extracted boundary conditions. The experimental work included full-field and discrete temperature measurements of an engine-based powertrain system under a wide range of road loads (vehicle speed and road grades). This paper presents a complete analysis of an inline 6-cylinder, 3.0L, 255hp powertrain's thermal characteristic and its relationship to vehicle speed and road loads. This study adopted the approach of combining both simulation and experiment in order to determine the time-dependent boundary conditions, heat sources and heat sinks in a powerful thermal-solver "RadTherm". The proposed 3D thermal model was used to perform transient and steady-state thermal analyses. A four-wheel-drive (4WD) chassis dynamometer was used to implement various driving scenarios during testing, while a network of thermo-couples and a micro-bolometric detector were used to acquire the temperature maps. The results of the thermal analysis from the model were compared with experimental results to provide a valuable conclusion. The developed model was also further utilized to optimize thermal packaging design of some powertrain parts through, but not limited to, rerouting of the heat sources and heat sinks in the vehicle design, applying thermal shields, replacing materials and increasing cooling.

Introduction

Recent governmental regulations pressing for improved fuel economy in terms of miles per gallon (MPG)—e.g., the CAFÉ standards—forced automakers to revisit and further improve their vehicular thermal management systems. At the same time, current studies of the vehicular thermal management systems still rely on simulating the heat transfer of as-built automotive parts using a Computer Aided Design (CAD) tool to describe the geometries and topologies, followed by a Computational Fluid Dynamics (CFD) tool to solve the heat transfer equations. Typically, thermal modeling assists in analyzing thermal loads of underhood components for better thermal packaging schemes that might lead to reductions in exhaust emissions and an increase in thermal efficiency. In addition, new packaging concepts might also result in weight and cost savings, and might allow engineers to devise new control strategies for cooling. Such new strategies might include electrically driven cooling systems or the use of materials with improved thermal properties. This paper describes the development of a 3D Finite Element (FE) thermal model for an internal-combustion-engine -propelled powertrain along with its exhaust system components.

Literature Review

Several vehicle thermal models have focused on investigating vehicular underhood components; Fluent Inc. developed a comprehensive simulation tool for underhood thermal management [1] with the aim of analyzing thermal performance and characteristics of the automobiles' different underhood packaging designs. A dual-cell heat exchanger model was used to simulate the underhood non-uniform heat rejections at different ambient temperatures. However; a uniform temperature map was assumed at the exhaust manifold surface, while assuming that the exhaust pipes were the heat source. Furthermore, in this study, the 3D model surface domain was discretized using a tetra-mesh scheme, which—depending on the solver scheme used to solve the heat conduction and radiation equations—may result in non-uniform element local heat conduction.

Additionally, other commercial CFD simulations might suffer in terms of accuracy because they incorporate several assumptions and approximations, due to the fact that results for a given simulation might be applied as a boundary condition for the next run, and/or basic thermodynamic calculations or ideal cycles might be used for the sub-models. Priya et al. [2] presented a thermal model of as-built automotive parts using a software platform, MuSES, with a set of thermographic detectors for extracting the needed boundary conditions. This study focused only on the engine under idling conditions; no other loading schemes were applied. Andreas et al. [3] discussed the use of a reverse-geometry approach using thermal acquisitions from thermography to

model the vehicle components as 3D topologies, which would be used in the FE model. However, these acquired thermal maps were not 3D scans of a real-world object, but were instead surface fabrics derived from the thermal images. These thermal images, or thermograms, should first be corrected for lateral heat conduction and emissivity and material variations. Moreover, such thermal images provide a surface fabric without representing a precise surface geometrical shape, especially when intricate geometries are involved. Omar et al. [4] introduced an approach to correct the thermograms for lateral heat conduction and emissivity effects using a Thermal Point Spread Function (T-PSF) and emissivity maps, respectively.

Methodology

Understanding the boundary conditions for the underhood components is vital to be able to guarantee modeling accuracy; hence, in this study, a set of thermographic detectors were employed in order to capture the underhood components' boundary conditions under different road load conditions. The infrared detectors, with their contactless, real-time temperature measurement capability, can provide accurate temporal and spatial temperature maps, when corrected for emissivity and environment contributions [5], [6]. This study employed two different thermal imagers: 1) a micro-bolometric focal plane array operating in the Long Wave Infrared LWIR 8–13 micron spectra; and, 2) a cooled, Indium Antimonite InSb detector with sensitivity in the Mid-Wave MWIR 3–5 spectra.

To mimic the different road loads and driving conditions under the controlled environment, a 4-wheel-drive, 4-roller chassis dynamometer (Renk Labeco, 500HP) was used along with a 500HP FEV engine dynamometer. The test vehicle in this study was a BMW 35i with a 6-cylinder in-line, 3.0L, 255HP engine.

The uncooled micro-bolometric detector (commercial name A40M, a product of FLIR Systems, Inc.) is capable of a 33Hz acquisition rate with a resolution of 1.3mrad, and a thermal sensitivity of 0.08C^{o} at 30C^{o}. It is capable of detecting a temperature range from -40C^{o} to 500C^{o} with an accuracy of 2% or 2C^{o}. The cooled detector is a Phoenix DTS package able to acquire up to 20kHz with the sub-window option; its Noise Equivalent Temperature Difference (NETD) is 0.1mK. The two-camera system was used to neutralize the emissivity effects using the multi-color pyrometery calculations. Additionally, a network of thermocouples was deployed to acquire a reference temperature signal to help correct the detectors' readings. Figure 1 illustrates the experimental setup of the vehicle inside the chassis dynamometer chamber. The acquired boundary conditions were then deployed into a finite differencing code environment for thermal analysis. The 3D CAD model for the test vehicle was constructed from actual 3D scans of the objects using a stereo-based, hand-held scanner (with a resolution of 0.05mm and a depth of field of 300mm) and a Zeiss full-size Coordinate Measuring Machine CMM (commercial name Zeiss Pro-T). The surface geometries were first acquired in a stereo-lithographic (.STL) CAD file. Then, it was post-processed through rapid-forming to reverse-engineer the CAD file into each target's dimensional features, which were then meshed.

Figure 1. Renk Labeco Chassis Dynamometer

Experimental Procedures

The engine's thermal maps were monitored under various power demands at the wheels, while the chassis dynamometer was used to simulate the representative road loads (i.e., vehicle speed and road grades) by controlling wheel resistance. The infrared detectors were set up to measure the surface temperature profiles for the engine, the exhaust manifold, the catalytic converter and the muffler. These specific components were thought to represent the main heat sources under the hood and under the body. Each thermal imager field was adjusted to cover the target locations for each run, in addition to removing all of the non-value-added features or background contributions through software or hardware filters. In addition, within each Field of View (FoV), a set of Regions of Interests (ROIs) were initiated in order to collect the maximum, minimum and average temperatures to improve the acquisition accuracy. In some instances, the un-cooled detector's dynamic range was adjusted in order to capture the target peak temperature [7], [8]. Figure 2 displays the configuration of the detectors during the underhood testing.

Figure 2. Infrared Detector Setup While Detecting the Heat Emissions from Under the Hood

The thermocouples network employed a high-speed, 8-channel Thermo Couple Interface Card (TCIC) with the I/O set up through a high-speed USB interface; the TCIC DAQ was calibrated with the sample rate adjusted to 10Hz. Figure 3 shows the thermocouples mounted using an epoxy bonding agent on the catalytic converter surface.

Figure 3. Thermocouple Mounted using an Epoxy Bonding Agent on the Surface of the Catalytic Converter

Testing Behavior

The main heat source in a conventional (internal combustion propelled) vehicle is its engine, with the generated heat raising the temperature of the underhood structural components. Thus, the engine and the exhaust system—including the exhaust manifold, the catalytic converter and the muffler—were targeted in the boundary condition extraction process.

The surface temperatures for each part were captured over a 42-minute period during which the vehicle speed was set to increase by 10MPH every six minutes up to a final speed of 70MPH. However, to ensure that the test included applying representative combinations of road loads, i.e., speed and grade, the temperature acquisition tests were repeated for the grades of 3, 6, 9 and 12%, with an external draft of airflow applied to prevent engine overheating. Table 1 illustrates the vehicle speed and the associated cooling air flow rates in Cubic Foot per Minute (CFM) as applied during the test. Table 2 shows the road grades applied in each run.

Table 1. Vehicle Speeds and Associated Airflow Applied for Cooling

Load Interval	0-6	7-12	13-18	19-24	25-30	31-36	37-42
Speed	10	20	30	40	50	60	70
Air flow (cfm)	4500	4500	4500	4500	9000	9000	9000

Subsequently, the experimental data included all of the transient temperature curves from the thermocouples and the 2D spatial thermal images from the thermal cameras for each test run.

Table 2. Road Grade (%) Applied in the Test

Capture No.	I	II	III	IV
Grade %	3	6	9	12

3D Thermal Model Design

This section describes the development of the 3D FE model for the complete conventional vehicle powertrain. The current investigation utilized a Finite Differencing platform (commercial name RadTherm, product of Thermo-Analytics) as the main solver. This code included an optimized thermal solver that can provide an image viewer in wireframe, in addition to an animated thermal display [9-11]. Additionally, the RadTherm solver has the capability to address steady-state and transient scenarios. Also, the code has a 3D graphic editor to allow the user to define material properties for each of the geometrical elements or group of elements. Following the properties assignment, the solver discretizes the element for each part by breaking them into thermal nodes [12].

Since radiation is a dominant mode of heat transfer, and since the underhood geometry is rather complicated, some modeling tools may combine assumptions and proximity for

radiation. The RadTherm solver, on the other hand, delivers a complete temperature distribution and heat rates for radiation. The net radiation heat exchange between two different surfaces can be computed using Equation (1) [11]:

$$Q_{net} = A_1 F_{1-2} \sigma (T_1^4 - T_2^4) \quad (1)$$

where T_1 and T_2 are the surface temperatures in K; F_{1-2} is the view factor; A is area m^2; and, σ is the Stefan-Boltzmann constant $Wm^{-2}K^{-4}$. View factor, F_{ij} , is defined in Equation (2) [2]:

$$F_{ij} = \frac{1}{A_i} \int_{A_i} \int_{A_j} \frac{\cos\theta_i \cos\theta_j}{\pi R^2} dA_i dA_j \quad (2)$$

where A_i and A_j are the areas of the surfaces i and j, respectively, and θ_i and θ_j are the angles between the position-dependent normal vectors to surfaces i and j and a line of length R connecting the points of the normal.

For accurate radiation heat transfer, the mesh quality of the CAD model was a crucial part of this model. The FE model was constructed in this study using deployed elements with an aspect ratio (width-to-length ratio) less than 4; and, in order to guarantee the uniformity of lateral heat conduction between the connected vertices within the each element, only Tri's or Quads were used with element sizes that ranged from 5–25mm. This size range was enough to resolve the thermal spatial geometry, yielding high convergence criteria at lower tolerances [9].

Other mesh quality issues were also improved by taking into consideration connectivity, duplicate, overlapping and penetrating criteria of the radiated elements. Figure 4 shows the principal quality of the required mesh used in this model.

Figure 5 displays the 3D vehicle model. The multi-layer materials for each part can be represented theoretically by a grid of nodes, spatially defined within the same part. In this study, user thermal nodes were established in order to link the fluid streams to their bounding parts. Figure 6 shows the fluid nodes used to link the exhaust gas fluid streams to the backside of the exhaust manifold ports through the exhaust tail pipe.

The design of this model required that the heat sources in the model be defined; in other words, the experimentally obtained exhaust gas temperature curve was assigned, which represented the exhaust gas upstream inside the cylinders in a way that would simulate the combustion process inside the cylinder. Knowing that this fluid is linked with a thermal node to the back (inner) side of the cylinder block (specifically the combustion chamber) was required in order to predict the exhaust gas temperature curve experimentally. Consequently, and in order to predict the exhaust gas temperature, the exhaust gas temperature curves inside the exhaust manifold ports were predicted using the experimental data measurements.

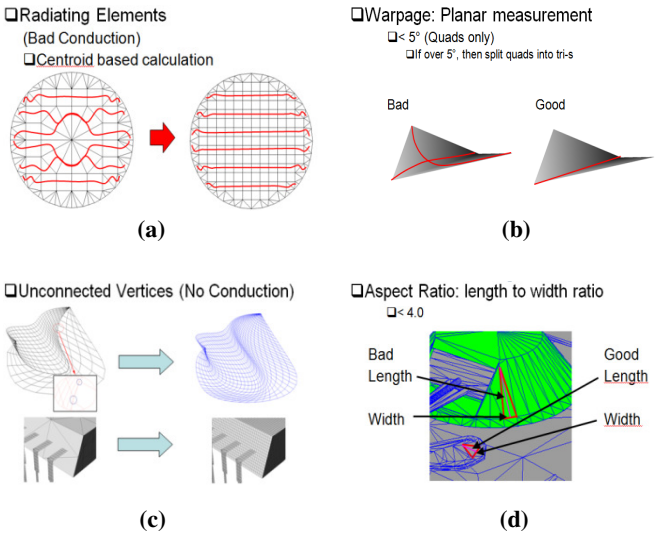

Figure 4. Meshing Requirements (a) Centroid (b) Vertices (c) Warpage (d) Aspect Ratio [9]

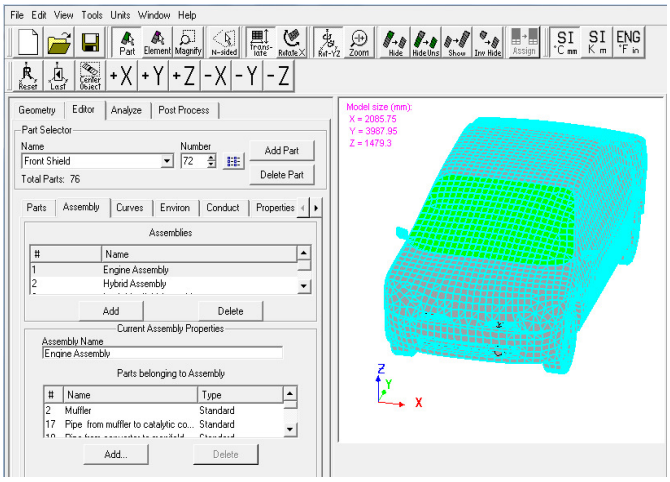

Figure 5. RadTherm Graphical User Interface

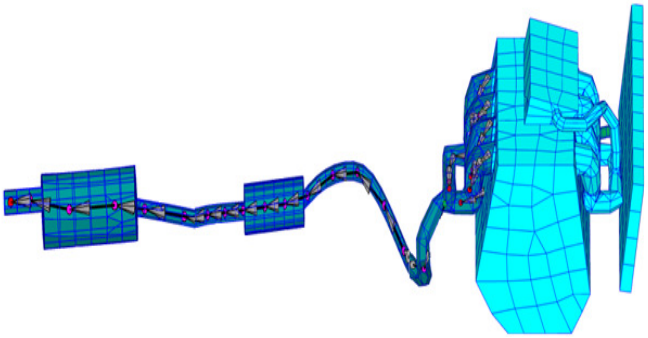

Figure 6. Exhaust Gas Fluid Streams Bounded by Exhaust System Components

The ambient air surrounding the underhood area and the underbody components was also considered in the model; a fluid node (ambient air) with an initial room temperature as recorded by the experiments was linked to the parts' front (outer) side. Finally, the lubrication and the cooling systems were simulated as a group of internal gaps created inside the cylinder block FE model; the lubricant and coolant fluid flow through these designed paths. This was done to simulate the heat rejections through these two fluids, which also aids in capturing the thermal performance of the cooling system. The coolant was then forced to circulate in and out of the cylinder block inner shell and pass through the coolant radiator. In setting up the boundary conditions process, the only assigned temperature curves were those for fluid nodes to simulate the combustion process inside each combustion chamber. These time-dependent temperature curves were synchronized with the combustion process occurrences, as obtained from the engine RPM. The exhaust gas fluid stream through the exhaust system towards the tail pipe was linked to the combustion chamber fluid nodes. The rest of the boundary conditions included an initial temperature assignment for all parts of the model.

Finally, after all boundary conditions were set up, the model was executed for all of the test runs implemented in the chassis dynamometer under the prescribed loading schemes. The model was run in 1-minute time steps, while the tolerance slope was set to a minimum. Then, the temperature curves for the different parts in the powertrain were extracted and compared against the experimental data.

Results and Discussion

The accuracy of the proposed 3D thermal model was analyzed by comparing its predicted temperature curves (spatial and transient) against the experimental data. The main goal of this simulation model was to predict the thermal signature of the underhood and underbody components under different loading profiles in terms of road loads which included vehicle speed and road grades. Figure 7 illustrates the rise in the average surface temperature for the exhaust manifold, as recorded by the un-cooled infrared detector. One can observe the high rise in temperature over time, which might lead to pixel saturation at certain temperature range settings—an integration time of the Focal Plane Array. Also, it was noticed that the components' surface temperatures increased with an increase in vehicle speed, as compared to an increase in road grade. In other words, vehicle speed causes more thermal load on the powertrain than does road grade. For instance, an increase in speed from 0–70MPH leads to a rise in exhaust manifold surface temperature to about 553K for the same 3% grade over 42 minutes. However, an increase in the grade from 3% to 12% causes an increase of only 140K in the surface temperature over the same period.

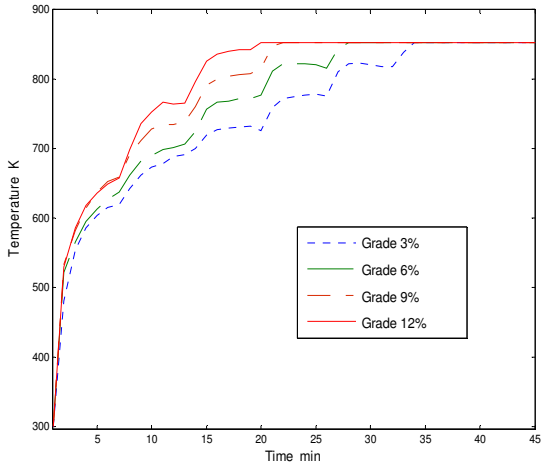

Figure 7. Exhaust Manifold Surface Temperature Curves as Recorded by the Infrared Detector

The parts' surface temperatures were plotted as a function of load; e.g., vehicle speed and road grade, as shown in Figure 8. Figure 9 illustrates the exhaust manifold surface temperature as predicted by the model in comparison with the actual temperature for the 3% and 9% road grades; the two curves were in agreement up to the point where the pixels of the infrared detector reached the saturation point. The temperature curve for the exhaust manifold surface indicated that this saturation took place after 28 and 34 minutes for road grades of 6% and 9%, respectively.

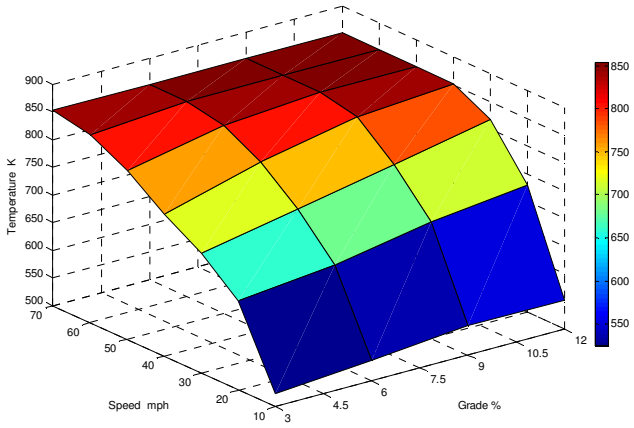

Figure 8. Exhaust Manifold Actual Surface Temperature Obtained by the Infrared Detector

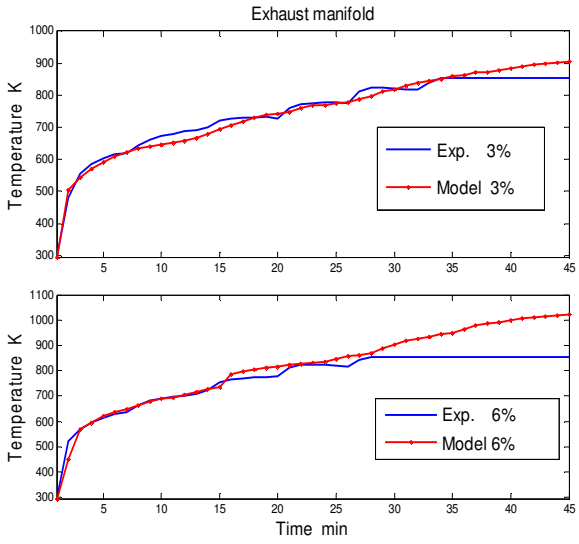

Figure 9. Exhaust Manifold Surface Temperatures as Predicted by the Model versus Actual for 3% and 6% Road Grades

In order to measure the uncertainty associated with the temperature measurements, an uncertainty analysis of both thermocouples and IR detector measurements were conducted. The input signal from the thermocouples was within the range of 0-500mV with a resolution of 0.019. The accuracy of the thermocouple acquisition was found to be ±1.5Cº. With automatic emissivity correction and a thermal sensitivity of 0.08Cº, the accuracy of the infrared detector was found to be ± 2Cº.

Subsequent to model validation, the model was utilized in optimizing the powertrain components' thermal design; several design manipulations can be tested in order to obtain better thermal performance in terms of heat rejection or insulation. These manipulations included material replacement, rerouting heat sources and heat sinks, shielding, apply different cooling at specific locations and/or load conditions, among others [13]. Consequently, several possible changes were implemented in the model; Table 3 summarizes these design modifications.

Table 3. Modifications Applied to the Current Design

Part	Current design	New design
Under Body	Steel	Aluminum, Magnesium
Engine Cylinder Block	Steel	Aluminum and Magnesium
Splash Wall	Steel	Titanium, Aluminum
Catalytic Converter	Un-shielded	Apply shielding

The automobile underbody—like other Body-in-White "BiW" panels—was made of several steel grades; at the same time, many automakers tried to replace the steel with other less dense materials such as aluminum and/or Poly-Metal Hybrids (PMH) for light-weight engineering purposes, which in turn affects the vehicle's thermal signature and impacts its thermal management system [14]. The modifications from Table 1 were implemented in the model with their thermal characteristics captured and then analyzed. For instance, Figure 10 displays the physical heat flux for a steel underbody, compared with that from an aluminum underbody. The results show that more heat is conducted through aluminum because of the higher thermal diffusivity, which allows for more heat to be rejected to the surrounding air.

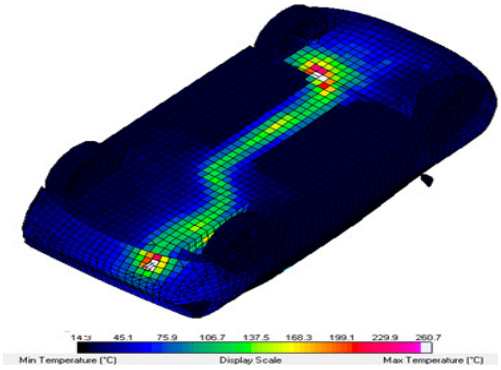

(a)

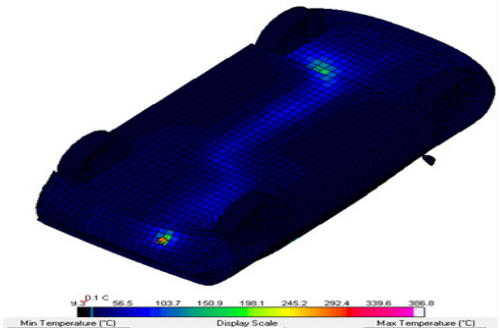

(b)

Figure 10. Heat Flux Through the Underbody: (a) Al 5083 (b) Mild Steel

Nevertheless, other packaging and thermal utilization strategies might also assist in optimizing the vehicle's thermal management system and/or its thermal signature. For example, rerouting heat sources and sinks in the vehicle might disturb the thermal management system, but packaging techniques such as applying selective shielding between the heat sources and other components can reduce the load on the underhood, temperature-sensitive components and

enhance their thermal performance; such techniques will assist in applying fewer thermal loads on specific components with sensitivity to temperature such as the electronics and the electric machines' wiring network. Also, shielding with different reflectivity grades can be tested. An test run showed how the model can predict shielding performance in preventing heat emitted by the exhaust system (see Figure 11) from being transferred into the underbody packaged components, such as the battery packs in hybrid vehicles. Nonetheless, this also assists in the improvement of the in-cabin passenger thermal comfort.

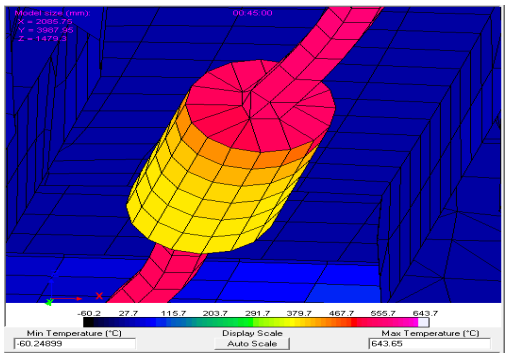

(a)

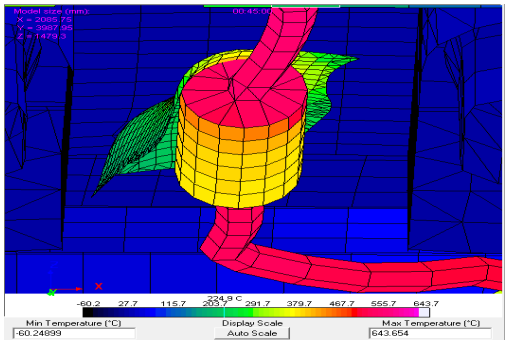

(b)

Figure 11. Heat Flux within the Catalytic Converter (zoomed): (a) Shielded (b) Un-shielded

Conclusions

This study developed a 3D FE-based model for an internal-combustion-engine-propelled vehicle, with a focus on its underhood and underbody components. The study utilized an in-house experimental setup that tested the powertrain using a 4WD chassis and engine dynamometers, in addition to using full-field and discrete-temperature measurement approaches using infrared imagers and a thermocouple network. The tests tried to imitate different road loads by changing the road grades and speed combinations for the powertrain. The 3D model utilized a multi-heat transfer and one-dimensional fluid-flow commercial thermal solver that can assign fluid streams and thermal nodes of the components' CAD surface geometries, while linking all of the model parameters to simulate actual conditions. The results showed that the results from the model are in agreement with experimental results. Also, the results exposed the effect of vehicle speed and road grade on the exhaust system thermal loads, further showing that speed has a bigger impact. Additionally, the study showed the potential of the developed model in testing different design concepts in terms of shielding characteristics and vehicle powertrain thermal repackaging.

References

[1] Application series from Fluent, (2003, June). *Under Hood Thermal management*. Fluent Inco, EX201-2003.

[2] Govindasamy, V. P. M. (2004), *Thermal Modeling and Imaging of As-built Automotive Parts*. Thesis, University of Tennessee, Knoxville.

[3] Koschan, A. F., Govindasamy, P., & Sreeenivas, S. (2006). Thermal Modeling and Imaging of as-Built Vehicle Components. *SAE* 2006-01-1167.

[4] Omar, M. A. (2010). *Dedicated processing routines for industrial thermograms*. (1st ed.). Wiley.

[5] Zhou, Y., Mayyas, A., & Omar, M. A. (2011). Principal Component Analysis-Based Image Fusion Routine with Application to Automotive Stamping Split Detection. *Research in Nondestructive Evaluation, 22*, 76-91.

[6] Korukçu, M. Ö., & Kilic, M. (2009). The Usage of IR Thermography for the Temperature Measurements Inside an Automobile Cabin. *International Communications in Heat and Mass Transfer*, *36*, 872-877.

[7] Astarita, T., Gardone, G., & Carlomango, G. M. (2006). Infrared thermography: an optical method in heat transfer and fluid flow visualization. *Optics and Lasers in Engineering, 44*, 261–281.

[8] Chevrette, P. (1986). Calibration of Thermal Imagers. Proceedings of the SPIE. *The International Society for Optical Engineering*, *661*, 372-382.

[9] Schwenn, T. (2008, July). *Discretization Primer and Modeling Discussion*. Presentation at RadTherm Training.

[10] Johnson, K., Curran, A., & Less, D. (1998). MuSES: A new heat and signature management design tool for virtual prototyping. *Proceedings of Ninth Annual Ground Target Modeling and Validation Conference*. Houghton, Michigan.

[11] Curran, A. R., Johnson, K., & Marttila, R. (1995).

Automated radiation modeling for vehicle thermal management. *SAE International Congress & Exposition*, *Underhood Thermal Management Session, Paper No. 950615*.
[12] Valisetty, R. R., Namburu, R. R., & Petit, G. (2004). Parallel MuSES for Infrared Signature Modeling of US Army Vehicles and Targets. *Army Research Laboratory ARL-TR*-328.
[13] Mayyas, A. (2010). *Comprehensive Thermal Modeling for Power Split Hybrid Power Train and Power Electronics*. Dissertation, Clemson University.
[14] Grujicic, M., Sellappan, V., & Omar, M. A. (2008). An Overview of the Polymer-to-Metal Direct-Adhesion Hybrid Technologies for Load-Bearing Automotive Components. *Journal of Materials Processing Technology*, *197*, 363-373.

Biographies

ABDELRAOUF MAYYAS is an Assistant Professor of Automotive Engineering at Arizona State University. He earned his B.S. degree from Mu'uta University, Jordan, MS Computer Engineering, 2006 from Yarmouk University, Jordan, and Ph.D. in Automotive Engineering, 2010 from Clemson University-International Center for Automotive Research "CU-ICAR", SC, USA. Dr. Mayyas is currently teaching at Arizona State University. His interests are in energy management control of hybrid electric vehicles, advanced propulsion systems and energy storage systems for renewable energy sources. Dr. Mayyas may be reached at amayyas@g.clemson.edu

MOHAMMAD OMAR is an Associate Professor of Mechanical Engineering at Clemson University. He earned his B.S. degree from University of Jordan, and Ph.D. Mechanical Engineering, 2005 from the University of Kentucky, USA. Dr. Omar is currently teaching at Clemson University-International Center for Automotive Research. His research interests are in the area of Manufacturing, Materials and Design; specifically, knowledge based manufacturing systems and light-weight design, non-destructive testing of materials and structures. His work is published in 5 book manuscripts, 4 US and Japanese Patents, and more than 90 refereed journal publications, conference proceedings and keynote presentations. Dr. Omar may be reached at momar@Clemson.edu.

PIERLUIGI PISU is an Assistant Professor of Electrical Engineering at Clemson University. He earned his M.S. (Computer Engineering1996) degree from University of Genoa, Italy, and Ph.D. (Electrical Engineering, 2002) from the Ohio State University. Dr. Pisu is currently teaching at Clemson University-International Center for Automotive Research CU-ICAR. His interests are in the model-based diagnostics and prognostics, modeling and control of hybrid electric vehicles, and energy storage systems. Dr. Pisu may be reached at Pisup@Clemson.edu.

A.M. KANNAN is an Associate Professor of Alternative Energy Technology at the Arizona State University. He earned his B.S. and M.S. from Madurai Kamaraj University (India) and Ph.D. (Fuel Cells, 1990) from the Indian Institute of Science, Bangalore, India. Dr. Kannan is teaching courses on Alternative Energy Technologies at the Arizona State University. His interests are fuel cells systems, advanced batteries and solar cells. Dr. Kannan may be reached at amk@asu.edu

EFFICIENT DRIVES FOR SINGLE-PHASE AC MOTORS: ANALYSIS AND APPLICATIONS

Juan F. Gallego-Calderon, California State University Fresno; Nagy Bengiamin, California State University Fresno

Abstract

In this paper, the authors present an energy efficiency study of Variable-Speed Drives for Single-Phase Induction Motors. The objective was to evaluate popular variable-speed drive schemes as they operate in their most efficient mode under different loading conditions. The considered schemes included phase control, variable-frequency drives and voltage control. This study focused on the development of experimental test methodologies to characterize motors and implement desired control schemes. Mathematical modeling and computer simulations were also utilized for engineering design and analysis. The fan load application was considered for further illustration of the developed methodology. This study provides a general framework for the evaluation and selection of variable-speed drives.

Introduction

Speed control of AC motors evolved very rapidly with advances in power electronics technology [1]. Applications that were dominated by DC motors became most suited for AC motors as a more economical alternative. Three-phase motors, however, were the prime candidates for initial developments for their more significant impact on high-power industrial applications. With the maturing of three-phase motor drives, technologies started to find their way to single -phase motor applications which constitute the largest percentage of electric power consumption in commercial and residential applications. AC Single-Phase Induction Motors (SPIMs) are popular for their low cost and versatility. Compared to three-phase induction motors, single-phase motors lack the self-starting capabilities and they are more sensitive to loading conditions.

For applications with varying loads, a variable-speed drive is a must since it can achieve up to 50% in energy savings. This principle often applies to machines that need to be constantly starting. By means of variable-speed drives, it is possible to regulate the starting current of such machines and, therefore, save more energy [2]. There are three commonly known techniques for AC motor drives; namely, variable frequency [3], voltage control [4], [5] and variable rotor resistance. Several studies have been conducted to analyze the performance of the different drives.

Nomenclature

R_1, X_1	Resistance and reactance of the stator
R'_2, X'_2	Resistance and reactance of the rotor
X_m	Mutual reactance
τ_{ind}	Induced torque
V_{TH}, R_{TH}	Thévenin voltage and resistance
ω_m, ω_{sync}	Motor speed and synchronous speed in rad/sec
I	Stator current
Z_F, Z_B	Forward and backward impedance
P_{in}, P_{out}	Input and output power
P_{AG}, $P_{AG,F}$, $P_{AG,B}$	Air-gap power: total, forward and backward
P_{conv}	Converted power
P_{RCL}	Core losses
P_{rot}	Rotational losses
P_s	Power savings
f	Line frequency in Hz ($\omega=2\pi f$)
V	Phase voltage
τ	Torque
n_m, n_{sync}	Motor speed and synchronous speed in rpm
s	Slip
$p.f.$	Power factor
η	Efficiency

In this paper, the theory behind the steady-state operation of SPIM is presented and was used for the mathematical models development in this study. Experimental tests were then performed in order to determine the motor parameters. The torque-speed motor characteristic was used to validate experimental results of the motor-winding parameters. Power consumption under different loading conditions was ana-

lyzed experimentally and via modeling techniques for different control schemes under varying loading conditions to find the optimal mode of operation. Moreover, the fan application was analyzed in order to provide a real-life application where this kind of analysis is important for energy efficiency.

Induction-Motor Model

In applications where there is insufficient information available about the motor parameters, such as winding resistance and inductance, it is necessary to execute the following three classical tests: DC test, locked-rotor test and the no-load test. These experimental tests are based on the single-phase induction-motor static RC equivalent circuit model presented in Figure 1. This model is based on the double-revolving-field theory. This theory states that a stationary pulsating magnetic field can be expressed as two rotating magnetic fields (forward and backward) of the same magnitude but with different direction. The effective torque that is produced is then practically equal to the resultant sum of the torque components due to each of the two magnetic fields [6].

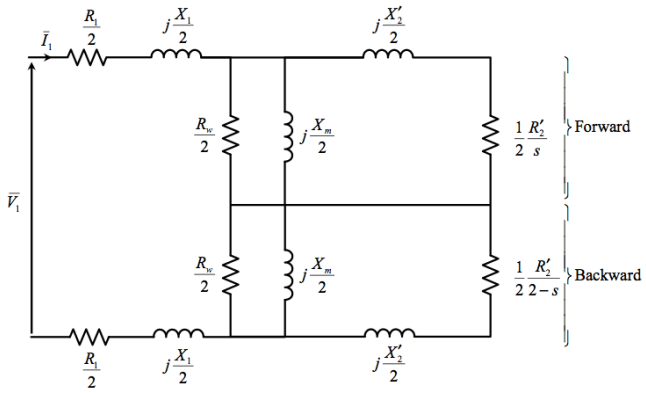

Figure 1. Equivalent Circuit of a Single-Phase Induction Motor

Since the purpose of this study was to analyze the energy efficiency of the drives discussed earlier, it was not necessary to analyze the dynamics of the induction motor. This is where the d-q model would have been necessary. The motor -winding parameters found experimentally are shown in Table 1.

This section describes the relationship of the motor's torque, power and speed. Chapman [6] derived the formula that describes the induced torque from an analysis of the three-phase motor's equivalent circuit. This formula can be applied to the single-phase motor using a 1/3 scaling factor since the torque is additive. Thus, this formula was applied here using the parameters presented in Table 1. In addition, the ideal torque-speed characteristic was compared with experimental data for validity.

Table 1. Induction-Motor Parameters

Parameter	Value
Main winding stator resistance (ohms)	15.8971
Main winding stator/rotor reactance (ohms)	17.9800
Main winding stator/rotor inductance (H)	0.0477
Main winding rotor resistance (ohms)	12.7190
Main winding mutual reactance (ohms)	223.1849
Main winding mutual inductance (H)	0.5920

It should be noted from Equation (1) that the produced torque is dependent on the slip (motor speed), operating frequency as it affects the reactance ($X=j\omega L$), and the phase voltage, V_ϕ. The resistance also plays a role, but it was assumed constant for purposes of this study. Most economical SPIMs are of the squirrel-cage type, where the rotor resistance is practically fixed. Wound-rotor motors may provide access terminals to change their effective rotor resistance. The dependence of τ_{ind} on n_m, V_ϕ, f and R_2 permits the reverse logic of adjusting n_m for a given τ_{ind} (load) using V_ϕ and f.

$$\tau_{ind} = \frac{\frac{V_{TH}^2 R_2}{s}}{\omega_{sync}\left[\left(R_{TH} + \frac{R_2}{s}\right)^2 + (X_{TH} + X_2)^2\right]} \quad (1)$$

where

$$V_{TH} \approx V_\varphi \frac{X_M}{X_1 + X_M}$$

$$R_{TH} \approx R_1 \left(\frac{X_M}{X_1 + X_M}\right)^2$$

Equation (1) was utilized to create the torque-speed characteristic curve presented in Figure 2, where $s = (n_m - n_{sync})/n_{sync}$. In physical experiments, the motor was operated under a variable load and the torque was measured at the corresponding speeds (see Figure 2). The rated motor voltage (115 V) and nominal frequency (60 Hz) were used in this test. Figures 3 and 4 show the simulation results for the same motor for variable f and $V\phi$, respectively.

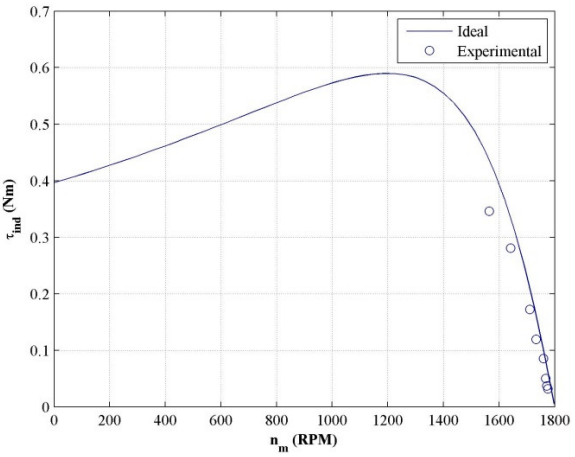

Figure 2. Induction-Motor Torque-Speed Characteristic

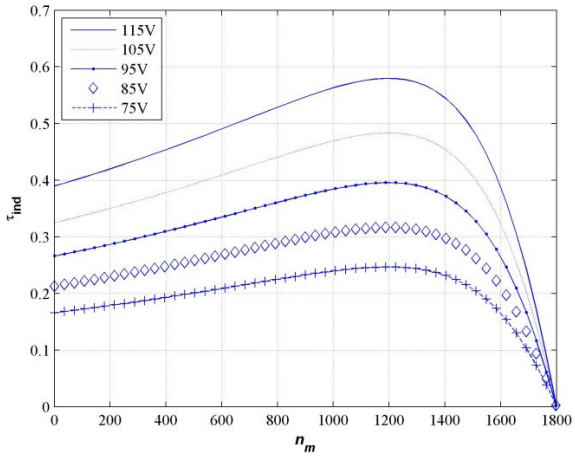

Figure 3. Torque-Speed Characteristic for Different Voltages

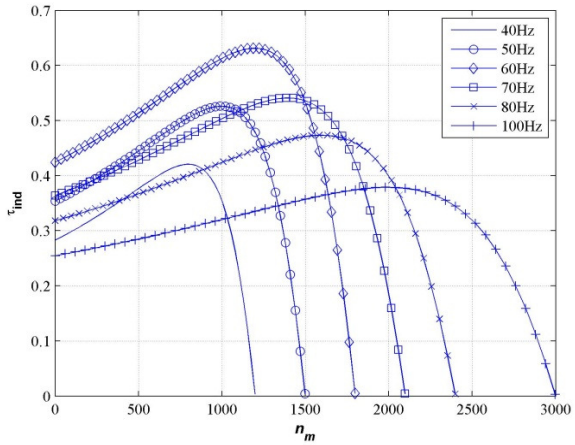

Figure 4. Torque-Speed Characteristic for Different Frequencies

System Setup and Experimental Data

In order to validate the simulation results, it is usually necessary to create an experimental setup capable of operating the motor at different load conditions, while monitoring the corresponding variables. A Hysteresis Brake was used for loading the motor. This device requires a regulated current source to produce a linearly proportional torque. Torque and speed sensors were used with their proper signal conditioning.

A variable-voltage AC power supply was an important piece of equipment in the setup. The Fluke-41B power analyzer provided an effective means to monitor voltage, current, power (real and reactive) and *p.f.* It provided valuable harmonic analysis data. Data acquisition and control were automated via traditional computer interface capabilities using LabVIEW software. Figure 5 shows a block diagram of the system and its physical setup.

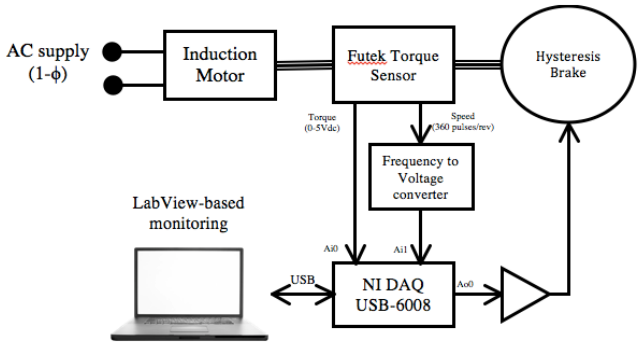

Figure 5(a). Block Diagram of the Experimental Setup

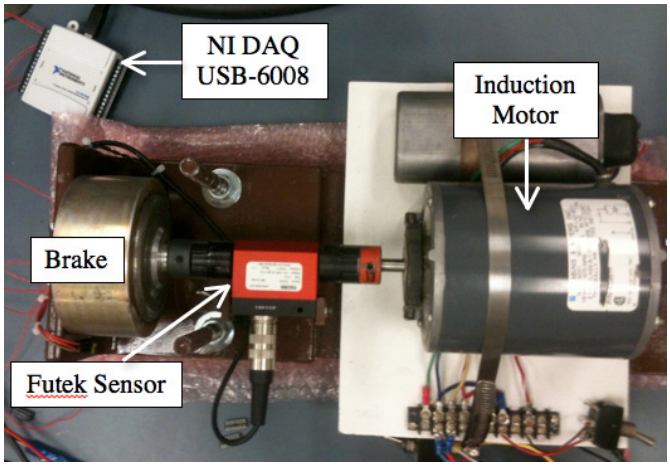

Figure 5(b). Motor-Brake Experimental Setup

Power Consumption

With the model of Figure 1 in mind, it is important to understand the power flow of a single-phase induction motor in order to analyze the data collected experimentally and validate simulation results. The calculated input power from Equations (2) and (3) corresponds to the power consumption of the motor, where V is the input voltage. Then, the first type of loss appears as stator copper loss, which corresponds to the power dissipated through the stator resistance, R_1. The power present in the air-gap is dissipated through the rotor resistance and is defined as P_{AG} in Equation(4). After some power is lost in the rotor, P_{RC}, the remaining power corresponds to the power converted from electrical to mechanical (P_{conv}); see Equations (5) and (6). The output and rotor powers are then given by Equations (7) and (8). Using the induction-motor parameters presented in Table 1, the motor was simulated under three different loading conditions in order to find the power consumption, the output power and the power converted from electrical to mechanical. These simulations were compared with the results obtained experimentally for model verification and are presented in Figure 6. These results demonstrate the validity of the mathematical model including the identified motor parameters.

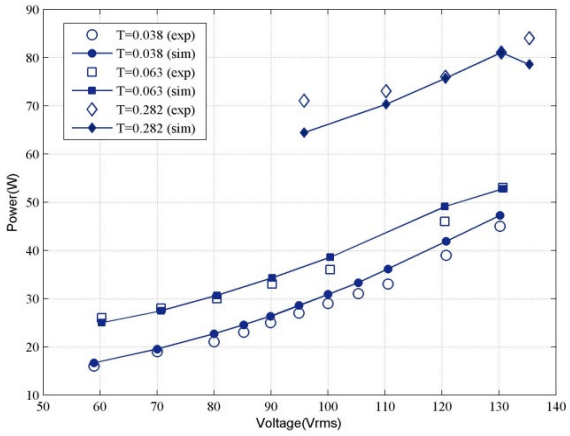

Figure 6. Power Consumption under Different Loading Conditions

Moreover, the model was validated through the experimental results obtained for the 120V, 100V and 80V voltage levels. Each voltage condition was tested over the torque range allowed by the motor. As the load increases, the speed and the slip change. Using these conditions, the values of R and L were determined for each case to conduct the simulations. The speed was measured experimentally and was then used to calculate the output power generated by the motor. In addition, the speed was used to calculate the slip used for the simulations. The results are presented in Figures 7-10.

$$P_{in} = VI\cos\theta \tag{2}$$

$$I = \frac{V}{R_1 + jX_1 + 0.5Z_F + 0.5Z_B} \tag{3}$$

$$P_{AG} = P_{AG,F} - P_{AG,B} \tag{4}$$

$$P_{conv} = P_{in} - P_{RCL} \tag{5}$$

$$P_{conv} = (1 - s)P_{AG} \tag{6}$$

$$P_{out} = \tau_{load}\omega_m \tag{7}$$

$$P_{rot} = P_{conv} - P_{out} \tag{8}$$

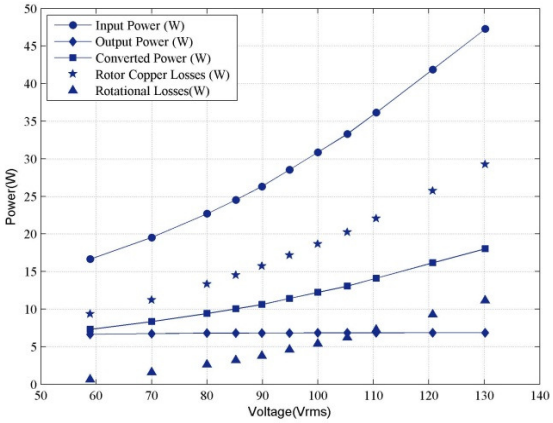

Figure 7. Power-Flow Representation over the Speed Range of Operation when Load is 0.038Nm

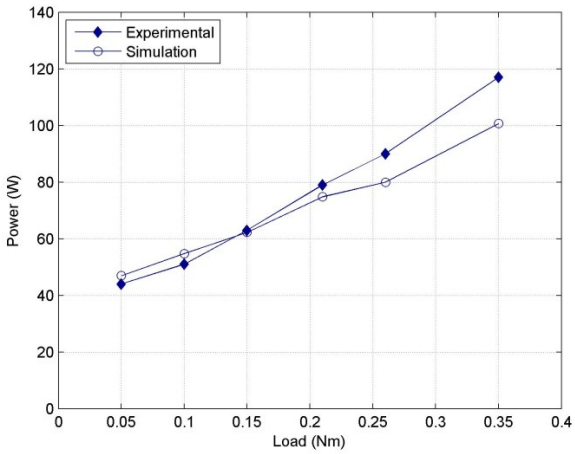

Figure 8. Power Consumption at 120Vrms

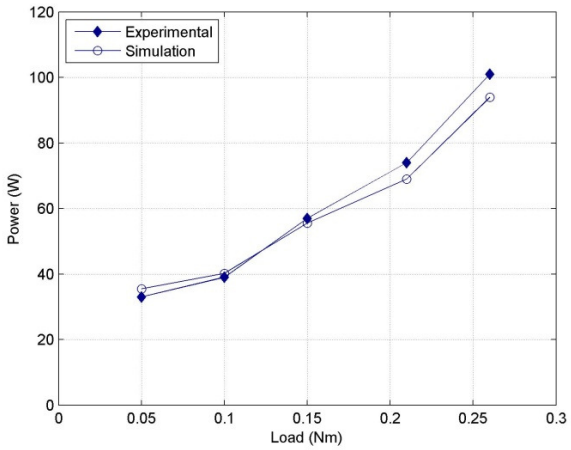

Figure 9. Power Consumption at 100Vrms

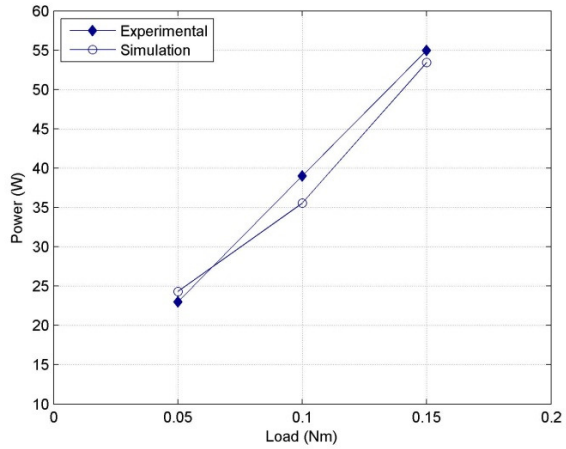

Figure 10. Power Consumption at 80Vrms

Energy Efficiency

The efficiency of the induction motor depends on several design parameters and factors that are part of the manufacturing process [7]. The motivation for producing high-efficiency motors is to reduce the operational costs of the machines over time. This study intended to develop a strategy for characterizing induction motors through simulations and experimental results, with the ultimate goal of finding the efficiency of the motor over a possible range of operation. In the previous section, the results showed the performance of the motor from a power-consumption point of view.

The efficiency results, experimental and simulated, obtained for a variation of the supply voltage and maintaining the operating frequency at 60Hz, are presented in Figure 11. Under these conditions, when the motor is operated near its rated condition (higher load and rated voltage), it achieves the most efficient mode of operation, as expected. Thus, notice that once again the steady-state model is a good approximation of the induction motor.

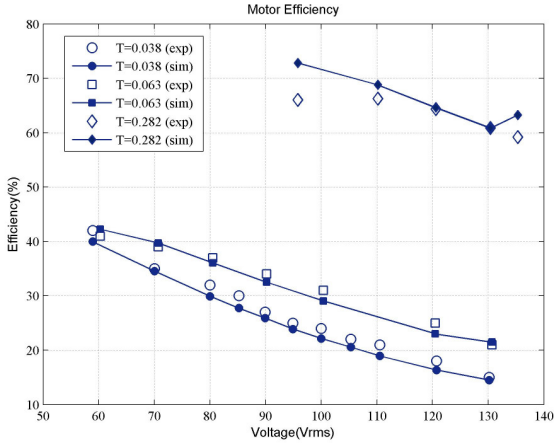

Figure 11. Efficiency under Different Loading Conditions (Operating at 60Hz)

Optimum Mode of Operation

The phase-control technique (control of the conduction angle) has a negative impact on the performance of the system due to the inherent presence of harmonics [8]. The Total Harmonic Distortion Ratio (THD-R) increases with the increment of the conduction angle. In addition, it was observed that when the motor was operating at certain voltages, and the load was increased, the THD-R also increased and the overall performance of the system diminished. Experimental tests were carried out to find the effects of this degradation on the efficiency of the motor under different loading conditions. The data presented in Table 2 show the experimental results using phase control over a range of loads, while operating at 100V.

Table 2. Experimental Results – Phase Control Operating at 100 V

Load (Nm)	n_m (rpm)	P_{out} (W)	P_{in} (W)	η (%)	THD-R (%)
0.05	1706	8.9326	36	24.81276	29.0
0.10	1674	17.5301	49	35.77569	29.2
0.15	1642	25.7925	62	41.60077	29.9
0.21	1606	35.3178	76	46.47077	30.7
0.26	1528	41.6031	104	40.00295	32.5

Notice the increase in THD-R as the load increases. Also, at the higher load (0.26Nm), there is a decrease in efficiency. This is because this loading condition is beyond the appropriate loading of the motor when operating at 100V. The results are shown in Figures 12 and 13 for the motor operating at 120V and 100V, respectively. In this configuration, the magnitude of the voltage is controlled by the input AC signal before it is passed through the rectifier. The frequency of the voltage applied to the motor after the full-bridge inverter depends on the modulating signal used for the PWM generator.

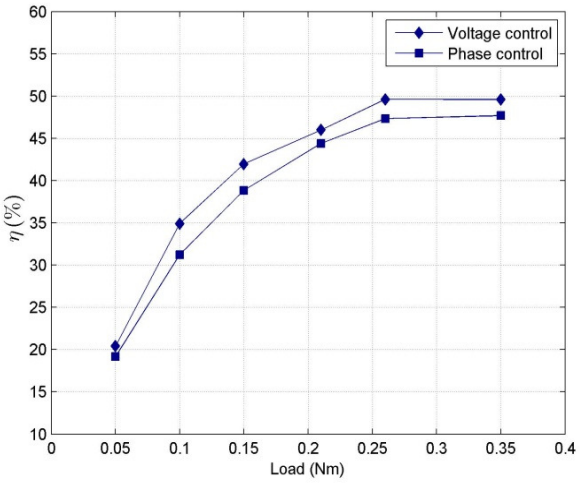

Figure 12. Efficiency at 120V

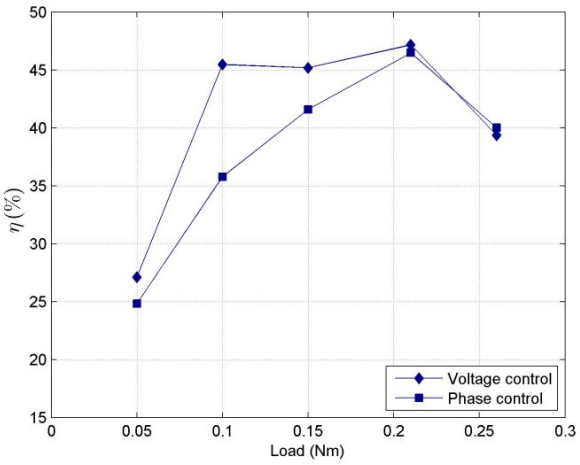

Figure 13. Efficiency at 100V

Finally, the three control schemes were compared by means of simulation (see Figure 14). It was found that the most efficient technique over the range of loading conditions, at rated values, was the variable-frequency scheme, where an inverter was employed. The PWM signal of the inverter can be modified depending on the application. If the frequency of the modulating signal is changed, the range of motor speed can be changed as well. This is a characteristic that is not possible via phase-control or voltage-control schemes. Matlab/Simulink was used to simulate the full-bridge inverter where the power devices were switched using PWM signals (see Figure 15). The inverter produces AC signals of a frequency dependent on the PWM signal. The amplitude of the AC signal was controlled by the magnitude of the DC signal at the input of the inverter [1]. The motor was modeled as an RL circuit, since the purpose of the study was to analyze the performance in the steady state. The resistor, R, corresponds to the losses in the stator and rotor losses, and the inductance corresponds to the main winding inductance [9], [10]. The resistor, R, would depend on the slip at which the motor is operated. The slip depends in the voltage and load applied to the motor. To analyze the motor using this model was necessary in order to define the operating conditions (speed and load) in order to find the slip through the torque-speed characteristic of the motor.

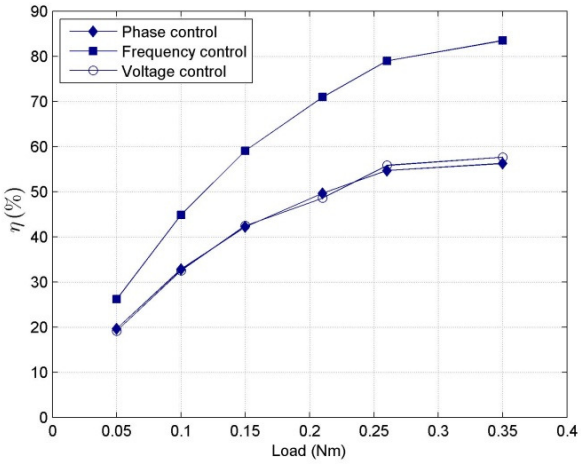

Figure 14. Efficiency under Different Loading Conditions

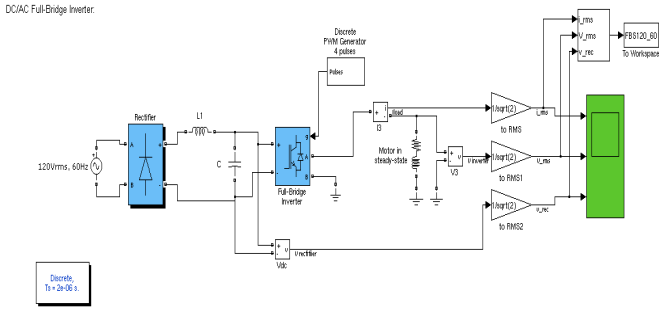

Figure 15. Full-Bridge Inverter Implementation in Simulink

The signals presented in Figure 16 show an example of the current and voltage output from the inverter to the motor in the steady state.

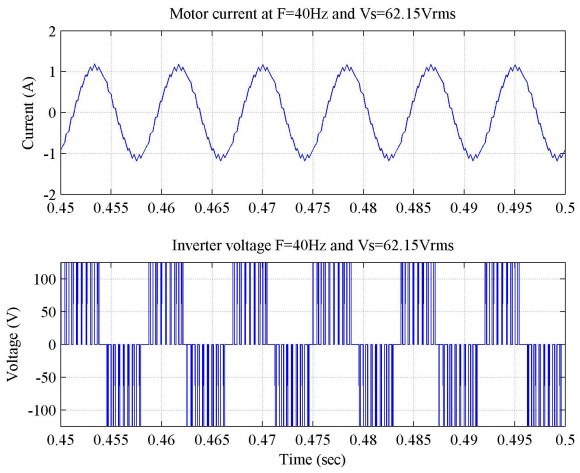

Figure 16. Example of AC Signals Generated by the Inverter

Fan Application

In variable airflow applications, it is common to use mechanical control devices like dampers while the motor continues to run at its rated power. This mode of operation is not efficient from an energy savings point of view since the power consumed is always constant, regardless of the desired airflow. As presented by Mohan et al. [1], the load torque in a fan application is proportional to the square of the speed, according to Equation (9), and the power consumed is proportional to the cube of the speed:

$$T_L = k_1 n_m^2 \tag{9}$$

where $k_1$is proportionality constant.

For this current study, a fan curve was assumed to be $k_1=8.546x10^{-8}$. Figure 17 illustrates the torque-speed characteristic of the motor at different operating voltages as well as the fan load curve. The intersection points of the fan curve with each of the corresponding motor curves signify the operating points for the fan at particular speeds. Each speed produces a specific air flow.

The theoretical results presented in Table 3 show the torque, speed, corresponding slip, power consumed and generated along with the efficiency of the motor at each of the intersecting points (fan operating points) (see Figure 17). In addition, the power savings compared to the use of dampers is calculated using Equation (10) and included in Table 3.

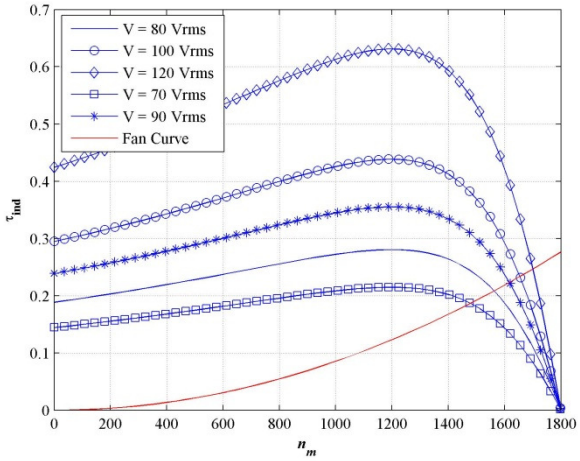

Figure 17. Variable-Voltage Motor Characteristic and a Fan Load

$$P_s = \frac{P_{rated} - P_{control}}{P_{rated}} x100 \tag{10}$$

Table 3. Operating Conditions of Fan at Different Speeds due to Voltage Control

V (V)	T (Nm)	n_m (rpm)	s (%)	P_{in} (W)	P_{out} (W)	η (%)	Pf	P_s (%)
70	0.186	1476	0.180	56.93	28.780	50.55	0.73	32.76
80	0.209	1576.4	0.132	65.04	34.147	52.50	0.75	23.19
90	0.224	1617.1	0.101	71.34	37.848	53.06	0.73	15.76
100	0.234	1654.2	0.081	76.41	40.534	53.04	0.70	9.77
120	0.247	1700.2	0.055	84.68	44.047	52.01	0.64	0

The data presented in these tables makes it abundantly clear that operating the motor at lower speeds, when less air flow is called for by the application, yields energy savings. Notice that the torque levels at each operating point is within the 100% load range of the motor. This is the reason why the efficiency and the power factor of the motor maintain an almost constant level, with minimum differences among the operating points.

Likewise, the variation of line frequency for speed control can be evaluated using the same methodology; this time, though, using the torque-speed characteristic curve of the motor at different operating frequencies versus the fan curves (see Figure 18). Table 4 contains the obtained theoretical results. It was found that the performance of the motor using the variable- frequency drive was superior to voltage control (see Figure 19). However, beyond the synchro-

nous speed, the motor consumes more power and, therefore, the power savings are negative (see Table 4).

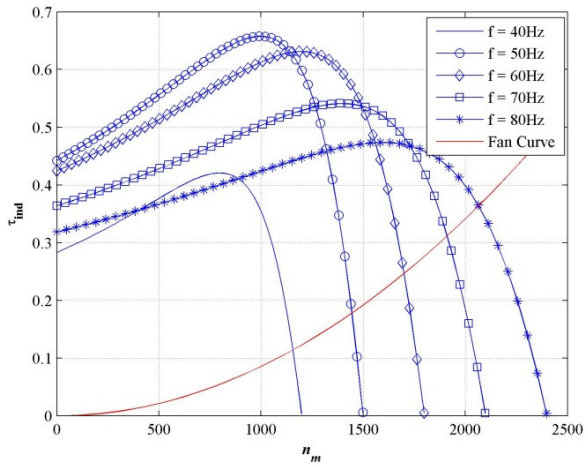

Figure 18. Variable-Frequency Motor Characteristic and a Fan Load

Table 4. Operating Conditions of Fan at Different Speeds due to Frequency Control

f (Hz)	V (V)	T (Nm)	n_m (rpm)	s (%)	P_{in} (W)	P_{out} (W)	η (%)	Pf	P_s (%)
40	80	0.114	1156	0.036	15.72	13.825	85	0.59	81
50	100	0.179	1445	0.036	37.7	27.012	64	0.70	55
60	120	0.247	1700	0.055	69.88	44.047	63	0.64	17
70	120	0.312	1911	0.090	101.3	62.443	62	0.70	-20
80	120	0.365	2065	0.139	116.1	78.813	68	0.76	-37

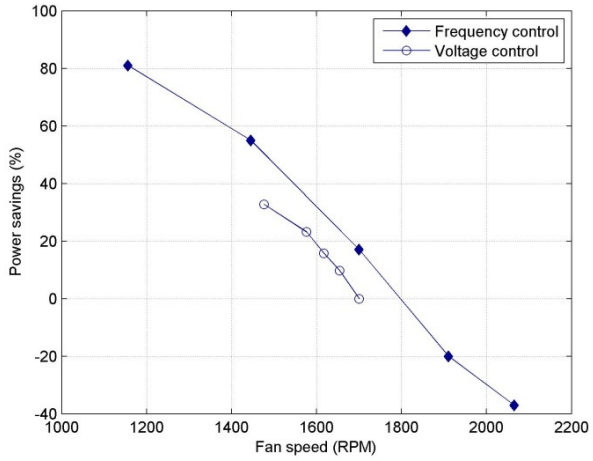

Figure 19. Power Savings Comparison: Voltage Control and Frequency Control

It is important to emphasize that the mathematical model presented here does not include the effects of harmonics. When the motor is operated using the variable-frequency drive, some harmonics are present in the voltage and current signals. The result of this is the mismatch in the power consumption of the motor at rated values (120V, 60Hz) for the two cases presented in Tables 3 and 4. However, it was also noticed that the calculated power factor using the mathematical model, and the one found through simulations, was the same. Therefore, the mismatch on power consumption was due to a lower current present in the motor.

Conclusion

The SPIM was successfully modeled for its steady-state operation in using the equivalent circuit method and experimentally determining the motor parameters. Test methodologies were developed and utilized to further validate the model and utilize it as an assessment tool for the efficiency of control schemes.

Three different speed-control schemes were considered when studying the performance of the motor under different loading conditions. It became evident that the high THD produced by the phase controller had a significant negative impact on motor performance, due to excessive power losses. Moreover, using the steady-state model, the full-bridge inverter was simulated as a variable-frequency drive and compared to the phase and voltage control schemes. It was found that the efficiency of the overall system was improved by approximately 25% at high loading conditions. However, at low loading conditions, the three techniques yielded a low efficiency of about 30%. It became clear that operating conditions may require changing the control scheme.

It is worth emphasizing that while PWM methodologies are usually embedded in numerous motor drives for their positive impact on the efficiency of the drives, the overall control scheme still needs to be evaluated carefully for its overall efficiency.

The fan application was studied for voltage control and variable-frequency control. These two schemes were chosen because of their higher efficiency compared to phase control. The variable-frequency drive yielded better results from an energy efficiency point of view. In addition, it is important to note that the variable-frequency drive works for a wider range of speeds, resulting in more versatility for the fan application. Thus, in some applications it might be necessary to have several options for the airflow and a wider range of speed would be needed. However, very high speeds may require changing the control scheme.

References

[1] Mohan, N., Undeland, T., & Robbins, W. (1998). *Power Electronics: Converters, Applications, and Design*. New York: John Willey & Sons, Inc.

[2] Schneider Electric. Unlocking Energy Efficiency - Management and Control is the Key. Retrieved from http://www.schneider-electric.co.il/documents/solutions/146-root-8-ee_white-paper.pd

[3] Latt, A. Z., & Win, N. N. (2009). Variable Speed Drive of Single Phase Induction Motor Using Frequency Control Method. *Proceedings of International Conference on Education Technology and Computer ICETC ,* (pp. 30-34, 17-20).

[4] Ahmed, N., Amei, K., & Sakui, M., (2000). AC chopper voltage controller-fed single-phase induction motor employing symmetrical PWM control technique. *Electric Power Systems Research*, *55*, 15-25.

[5] Yildirim, & Bilgic, M., (2008). PWM AC Chopper Control of Single-Phase Induction Motor for Variable -Speed Fan Application. Proceedings of *Industrial Electronics, IECON 34th Annual Conference of IEEE*, (pp. 1337-1342).

[6] Chapman, S. (2005). *Electric Machinery Fundamentals.* New York: McGraw-Hill.

[7] Amin, B. (2002). *Induction Motors: analysis and torque control*. New York: Springer.

[8] Sankaran, C. Effects of harmonics on Power Systems. EC&M Magazine. Retrieved from http://ecmweb.com/mag/electric_effects_harmonics_power_2

[9] Hamad, S. H., Bashi, S. M., Aris, I., & Mailah, N. F. (2004). Speed Drive of Single-Phase Induction Motor. *National Power & Energy Conference (PECon). Proceedings, Kuala Lumpur, Malaysia,* (pp. 121-125, 29-30).

[10] Li, H., & Curiac, R. (2010). Motor Efficiency, Efficiency Tolerances and the Factors That Influence Them. *Petroleum and Chemical Industry Conference (PCIC). Record of Conference Papers Industry Applications Society 57th Annual,* (pp. 1-6, 20-22).

Biographies

JUAN GALLEGO-CALDERON is currently a Ph.D. student at the DTU Wind Energy department, The Technical University of Denmark. He received his MS degree (Electrical Engineering, 2012) from California State University Fresno, CA. His present research interests are in electromechanical modeling, control systems, simulation of dynamical systems, multi-body dynamics and power systems in wind energy. He can be reached at jugc@dtu.dk

NAGY BENGIAMIN is a Professor of Electrical Engineering at California State University Fresno, CA, MEngr (Systems Engineering, 1976) from Carleton University, and Ph.D. (Electrical Engineering, 1979) from The University of Calgary, Canada. Dr. Bengiamin's current interests are in power systems, power electronics, and control systems. He is a senior member of IEEE. He can be reached at bengiami@csufresno.edu

INFLUENCE OF LOCAL SOIL CONDITIONS ON GROUND RESPONSE: SITE AMPLIFICATION IN SHARJAH, UNITED ARAB EMIRATES

M. Omar, University of Sharjah (U.A.E.); A. Shanableh, University of Sharjah (U.A.E.); M. Balwan, Sharjah Department of Public Works (U.A.E.); M.Y. Fattah, University of Technology (U.A.E.); K. Hamad, University of Sharjah (U.A.E.)

Abstract

Site amplification increases the intensity of ground shaking that can occur due to local geological conditions. It does not depend only on the magnitude of the earthquake and the distance from the epicenter, but mainly on local soil properties that can vary considerably due to local geological conditions that act as a filter, thereby affecting the seismic waves that come from the bedrock all the way to the ground surface. Good design of a seismic resistant structure requires an estimation of the ground amplification intensity during earthquakes.

This research study was part of a comprehensive seismic risk assessment puzzle put together by the Hazards and Engineering Risk Management Research Group for the city of Sharjah, United Arab Emirates, to help engineers and others in assessing and managing seismic risk—as it defines soil conditions—and its effects on ground motion traveling to buildings through soil. The authors carried out a local site-specific ground-response analysis using SHAKE2000, a one-dimensional ground-response modeling software covering the city of Sharjah. Soil data were collected from over 387 boreholes in order to develop local site amplification-potential maps in the area. Site effects were then integrated in the Geographic Information System (GIS) platform for combined hazard-assessment presentations. The Emirates of Sharjah is zoned indicating regions of different amplification potential and regions of high vulnerability to seismic hazard. In addition, spectral acceleration maps at various frequencies were developed for future planning purposes as well as for risk analysis of structural damage due to earthquakes.

Introduction

The most important seismological aspect of earthquake hazard mitigation is the prediction of the strong ground motion likely at a particular site. Nevertheless, the aspects of earthquake prediction that still receive the most publicity are the prediction of the place, size and time of the earthquake. Of course, prediction of the region where earthquakes are likely to occur has long been achieved by seismicity studies using earthquake observatories, useful probability estimates of long-term hazards which can be inferred from geological measurements of the slip rate of faults, regional strain changes, etc.

The path of the seismic waves in the upper geological formation strongly influences their characteristics, thus producing varying effects on the ground surface motion [1], [2]. The ground motion parameters at a particular site are influenced by the source, travel path and site characteristics. The influence of local soil conditions on the ground response has been recognized for many years and its significance was felt during the 1985 Mexican, 1989 San Francisco, U.S.A., and 1995 Los Angeles, U.S.A., earthquakes. In addition, Istanbul, Turkey, has also experienced many strong earthquakes throughout its history and suffered extensive damage. According to Ince [3], the data pertaining to the damage sustained by historical artifacts and structures from past earthquakes were examined along with the soil amplification of the region. It was found that soil amplification and partial liquefaction contributed to the damage of historical artifacts and structures.

Seismic events were once thought to pose little danger to United Arab Emirates (UAE) communities. However, recent earthquakes and scientific evidence suggest that the risk is much higher than previously thought. The al-Masafi earthquake of 2002 had a magnitude of 5.2, and the successive earth tremors that followed are strong evidence of the active seismicity of the area. Currently, no reliable scientific means exist to predict earthquakes. Therefore, identifying seismic potential locations, adopting strong policies and implementing measures and utilizing other mitigation techniques are essential to reducing risk from seismic hazards in any community. Sharjah is becoming one of the main Emirates of UAE, having the third largest population and active business centers. For this, creating multiple maps that identify seismic risk areas can help Sharjah's planners, policy makers, building code officials and engineers understand which areas should have minimal development to reduce the impact of earthquakes.

Over a period of two years, the authors collected and analyzed data from over 387 boreholes in the Sharjah Munici-

pality as well as others from different locations in the city. Many of the samples were collected from project sites where soil was used as backfill materials. The selections were based on the soil used for projects such as sub-base, sub-grade, below sub-grade, below foundation, below slab on grade and general filling.

In this study, a numerical analysis for the one-dimensional response of soil columns was carried out using SHAKE2000, a software package which has been previously used and found to be valuable [4]. It uses an equivalent linear, total stress analysis procedure to compute the response of a 1-D, horizontally layered viscoelastic system subjected to vertically propagating shear waves. Further, it uses the exact continuum solution to the wave equation adapted for use with transient motions through the Fast Fourier Transform algorithm.

This study aimed to perform analyses on the influence of local soil conditions on ground response during earthquakes at various locations in the Emirate of Sharjah, UAE. The specific objectives of this study were: (1) to contribute to a comprehensive seismic risk assessment study of the city of Sharjah; (2) to estimate the amplification potential and prepare maps indicating zones of high vulnerability to seismic hazard; (3) to obtain spectral acceleration maps used for seismic hazard risk assessment of the area; and, (4) to integrate the site effects in GIS for combined hazard assessment.

Geology and Seismicity of the Area

UAE has a mountain belt along the eastern coast on the Gulf of Oman, about one fifth of which is desert. The western part of the UAE is facing the subduction boundary across the Arabian Gulf opposite the Strait of Hormuz, one of the most seismically active zones in the world. The city of Sharjah faces the Zagros folded belt, one of the most active faults in the world. The main city lies on the Arabian Gulf and other parts of the Emirate lie on the Gulf of Oman. It is located in the geological window between altitudes 25º 25' N and 25º 14' N and 55º 45' E and 55º 20' E.

It has been generally accepted that the UAE has little or no earthquake activity. However, the country is not as safe from earthquake disasters as often assumed. In March, 2002, and according to Jamal and A-Homoud [5], an earthquake magnitude of 5 shocked the al-Masafi area, northeast of UAE, with its epicenter at a depth of 16 km. The strong motions recorded on December 10th, 2002, and April 25th, 2003, represent sufficient evidence of the existence of considerable seismic activity in the UAE.

According to UNESCO [6] and Malkawi et al. [7], the seismic activity in the area is attributed to the following:

1. Major faults of unknown activity levels have been mapped as transecting the UAE.
2. The horn formed by the territory of the UAE penetrates into the plate boundary of collision between the Arabian Peninsula and Asia, thus accumulating stresses.
3. The Zagros Mountain is a folded belt that extends for about 1,500 km in the northwest-southeast direction along the western part of Iran and the northeastern part of Iraq from Oman in the southeast to the Turkish borders in the northwest. The occurrences of earthquake events in the Zagros province define a zone, about 200 km wide, which runs parallel to the folded belt. The majority of the earthquakes occur in the crustal part of the Arabian plate that underlies the Zagros folded belt because it is one of the most active faults in the world. For example, a recent study of the historical seismicity of Iraq shows that most of the moderate to large historical events occurred in eastern Iraq along the Zagros folded belt.
4. The Makran subduction zone, the area where Oman Gulf subducts under the Eurasian plate, is an oceanic crust, which extends eastward to the Owen Fracture zone along the Indian plate boundary. This oceanic crust descends below the continental crust along the Makran subduction trench. This zone is capable of producing very strong earthquakes. For instance, the maximum regionally observed earthquake on November 27th, 1945, had a magnitude of 8.2 at about 750 km from the UAE.

Ground Response Analysis

Data Collection and General Classification

Soil borehole logs from over 387 sites covering most parts of the Emirates of Sharjah were utilized in this study. Boreholes selected were those with overburden thickness varying from 1 to 30 meters, representing typical geological features in Sharjah. The exact GPS locations for all boreholes were obtained from the Sharjah Directorate of Town Planning and Surveying, as shown in Figure 1.

Shear Wave Velocity

Due to a lack of availability of actual published shear wave velocities for the area under study, the following empirical model was used by Lyisan [8]:

$$V_s = 51.5\ N^{0.516} \quad (1)$$

where: N = uncorrected SPT
V_s = shear wave velocity, m/s

Figure 1. Borehole Locations in the City of Sharjah

Attenuation Relationship

The attenuation relationship is an equation that describes how the ground motion changes with magnitude and source-site distance. Joyner and Boore [9] developed a highly generalized attenuation equation based on worldwide data, which were generated in two forms for earthquake magnitudes between 5.0 and 7.0:

$$\log PGA = 0.49 + 0.23(M - 6) + \log r - 0.0027 \quad (2)$$

$$\log PGV(cm/s) = 2.17 + 0.49(M - 6) - \log r + 0.0026r \quad (3)$$

where

PGA	=	peak ground acceleration at bedrock
PGV	=	peak ground velocity at bedrock
M	=	magnitude of earthquake
d	=	shortest plan distance between fault and site (km)
r	=	hypo-central distance

$$r = \left(8^2 + d^2\right)^{0.5} \quad (2)$$

$$r = \left(4^2 + d^2\right)^{0.5} \quad (3)$$

Atkinson and Boore [10] developed the following model for PGA using all available worldwide data and for all ranges of ground motion levels:

$$\ln a = c_1 + c_2 m + c_3 r + c_4 \ln r + c_5 p \quad (4)$$

where c_1 = - 2.682, c_2 = 0.980; c_3 = 0.000580; c_4 = -1.522; and, c_5 = 0.518.

Equation (4) was used to obtain PGA at rock level after attenuation in the city of Sharjah [7], [11]. Figure 2 shows the grids of the PGA map for 50 years with a 10% probability of earthquake occurrence. The values obtained at bedrock for the city of Sharjah range from 0.06g to 0.09g.

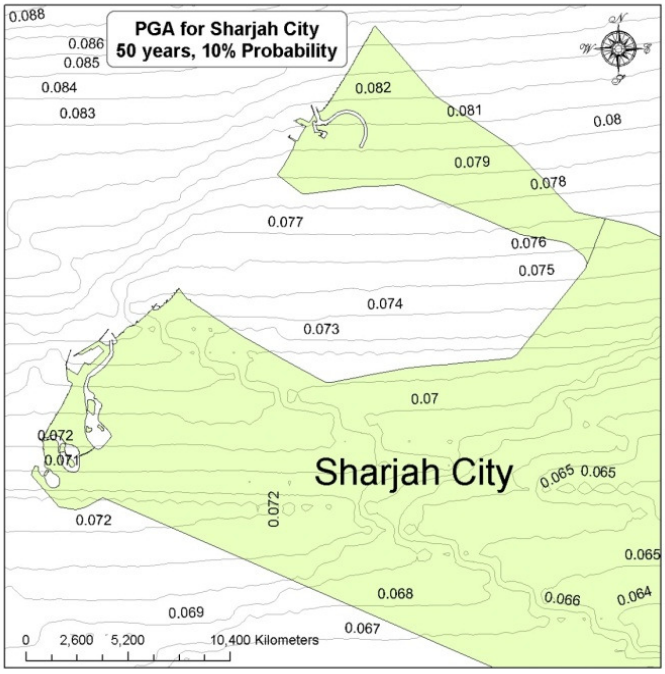

Figure 2. Seismic Hazard Map for the City of Sharjah for 50 Years and a Probability of 10% [7], [11]

Estimation of Ground Motion Signal at Bedrock

The input ground motion considered for this study was the Chalfant Valley (July 21st, 1986, at 14:42) with an earthquake magnitude of 6.2 as recorded by Long Valley Dam (L Abut) station. The reason for selecting this ground motion was based on two factors: the magnitude of the most effective earthquakes that originated from southern Iran and affected our study area was between 6.0 and 6.5, and the peak ground acceleration for the city of Sharjah over the last 50 years and with a 10% probability was between 0.06g and 0.09g. Chalfant Valley's PGA falls within the same range.

Results and Discussions

Microzonation of Ground Shaking

An equivalent linear one-dimensional ground response analysis using SHAKE2000 was followed for all borehole sites in the city of Sharjah in order to find the following parameters: peak ground acceleration, site amplification factor, peak spectral acceleration, frequency of peak acceleration, and the spectral acceleration at particular frequency zones. These factors are important for building a risk analysis. Maps showing the variation of these parameters in Sharjah were developed using GIS.

Peak Ground Acceleration at Rock and Surface

The values of the PGA at rock level for all locations were plotted following UNESCO [6] and Joyner and Boore [9] in order to obtain the PGA map shown in Figure 2. The values obtained at bedrock for the city of Sharjah ranged from 0.06g to 0.09g and were amplified based on the soil profile at different locations. From the SHAKE2000 analysis, the acceleration-time histories at various depths for all locations were found to obtain the peak acceleration value at the surface. These values, ranging from 0.04g to 0.3g, were plotted in order to obtain the Peak Ground Acceleration (PGA) map at ground surface, as shown in Figure 3. The map shows irregularly distributed peak acceleration values due to variation in the soil profile at various locations.

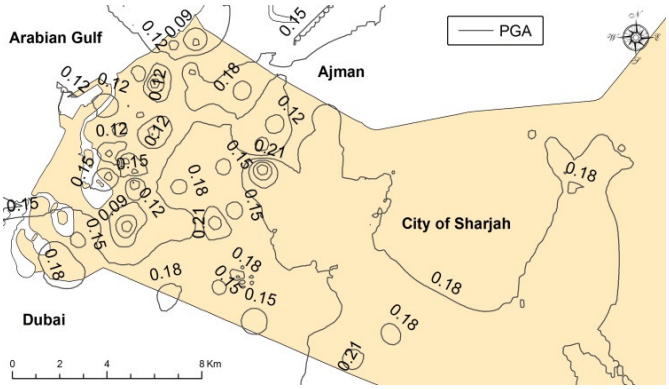

Figure 3. Peak Ground Acceleration Map at Surface Level

Site Amplification Factor

Amplification of ground motion is the increase in the intensity of ground shaking that can occur due to geological conditions. To estimate the amplification of the ground surface, it was necessary to estimate how many times the PGA at bedrock amplified on its way to the ground surface. The Site Amplification Factor refers to the ratio between the PGA at bedrock obtained from the ground acceleration-time history for each borehole and the PGA at the surface as an output from the ground response analysis. Results indicated that the amplification factors ranged from 1.2 to 3.0 for the city of Sharjah. Based on these factors, the city of Sharjah was divided into four main zones, as shown in Figure 4. Lower amplification values indicate smaller amplification potential and, hence, a lower seismic hazard.

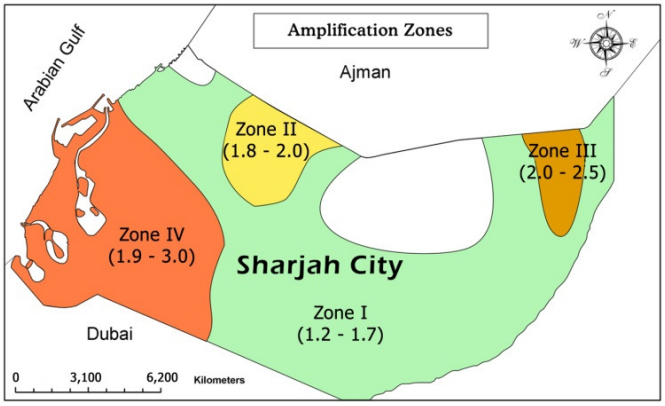

Figure 4. Site Amplification Factor Zonation Map for the City of Sharjah

As shown in Figure 4, most of the study area falls under zone I, which exhibits a relatively low amplification potential ranging from 1.2 to 1.7. The soil profile indicates that 70% of the soil column is dense to very dense, while 15% at a shallow 4-meter depth is loose. Table 1 shows typical soil profiles for zones I through IV. In zone II, a relatively small part of the city falls under this zone, with an amplification potential of 1.8 to 2.5. The soil profile indicates that 60% of the soil column is dense to very dense, while 15% of a shallow 4-meter depth is loose. In zone III, the amplification factor increased from 2.0 to 2.5. This is due to the soil column consisting of more loose to medium-dense soil, thus giving it more of a chance to trap the signal between soil particles with low shear wave velocity. Zone IV has an amplification factor of 1.9 to 3.0, which is slightly higher than previous zones. This zone contains less than 35% of dense to very dense sand, and more than 30% of loose sand, as shown in Table 1. It is worth mentioning that this region of the city contains high-rise buildings with a very dense population, indicating more risk potential.

Response Spectra at Surface

Distribution of Spectral Acceleration for Specific Frequency

At surface level, the estimate of the frequency at peak spectral acceleration is important for calculating the resonance effect from coinciding with the structure's natural frequency causing a negative impact on the safety of build-

ings. Therefore, the spectral acceleration of different frequencies—0.5 Hz, 2 Hz, 5 Hz, and 10 Hz—was calculated at each borehole and represents tall and high-rise, 3-4 story, 2-story, and 1-story buildings, respectively. A peak spectral acceleration (PSA) map for the city of Sharjah is shown in Figure 5. The PSA values vary from 0.14 to 1.4 and are divided into three main zones, as shown in Table 2.

Table l. Representative Soil Profiles for Zones I - IV

Depth, m	**Zone I**	Depth, m	**Zone II**		
	Soil Type	Avg. SV		Soil Type	Avg. SV
0 - 4.5	Loose Sand	160	0 - 4.5	Loose Sand	158
4.5 – 8.5	Medium Dense Sand	202	4.5 – 10.5	Medium Dense Sand	217
8.5 - 30	Dense to very Dense Sand	284	10.5 - 30	Dense to very Dense Sand	304
Depth, m	**Zone III**	Depth, m	**Zone IV**		
	Soil Type	Avg. SV		Soil Type	Avg. SV
0 - 7.5	Loose Sand	146	0 - 10.5	Loose Sand	128
7.5 – 20.5	Medium Dense Sand	261	10.5 – 18.5	Medium Dense Sand	234
20.5 - 30	Dense to very Dense Sand	302	18.5 - 30	Dense to very Dense Sand	308

Table 2. Zonation Based on PSA

Zone	PSA
I	0.14 -0.60
II	0.60 – 0.80
III	0.80 – 1.40

Figure 6 illustrates the spectral acceleration at 0.5 Hz, which relates to tall and high-rise buildings commonly found in the western part of the city of Sharjah. The acceleration values vary from 0.04g to 0.07g with an average value of 0.05g. This average value is on the lower end of the amplification range and considered relatively low from a seismic hazard point of view.

Figure 7 illustrates the spectral acceleration at 2 Hz frequency. The acceleration values vary from 0.06g to 0.5g with an average of 0.28g. The higher range is found in two areas, one around the coastal region, while the other is in the middle part of the city. A small part was also found near the northern border of the city of Sharjah.

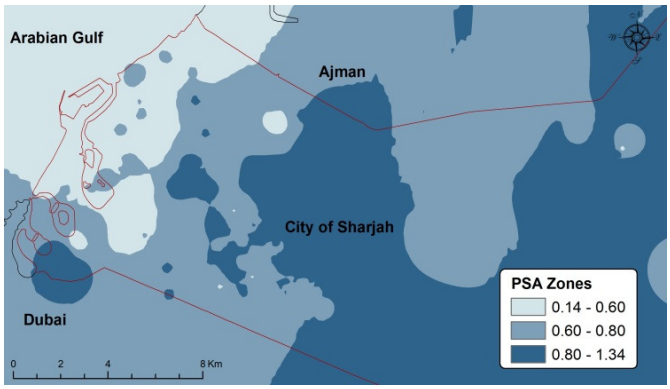

Figure 5. Peak Spectral Acceleration Zonation Map for the City of Sharjah

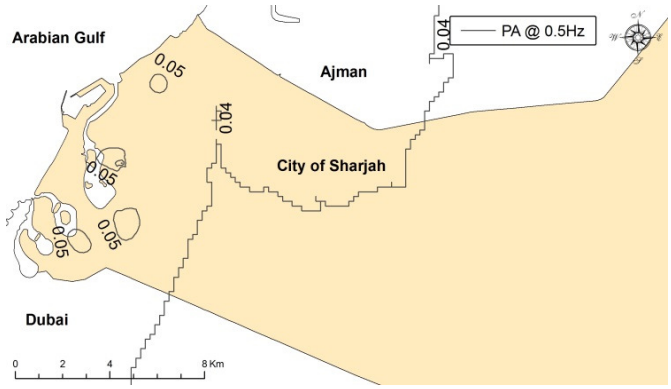

Figure 6. Spectral Acceleration Map of the City of Sharjah at 0.5 Hz

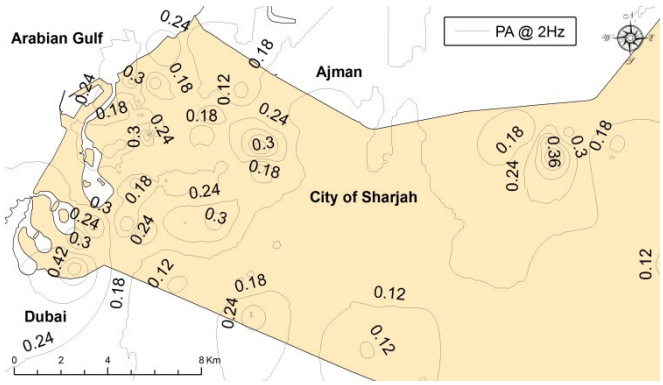

Figure 7. Spectral Acceleration Map of the City of Sharjah at 2 Hz

Figure 8 shows the spectral acceleration at 5 Hz, which relates to 2-story buildings. The acceleration values vary from 0.05g to 0.9g with an average value of 0.48g. Most of the areas that have high spectral acceleration in this frequen-

cy range are residential areas with 1- or 2-story buildings, which might be cause for concern during an earthquake.

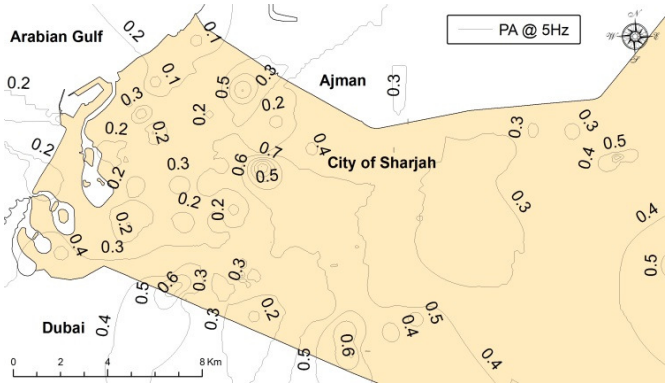

Figure 8. Spectral Acceleration Map of the City of Sharjah at 5 Hz

Figure 9 shows the spectral acceleration at 10 Hz. The acceleration values vary from 0.06g to 0.55g, with an average value of 0.3g. The distribution pattern of accelerations in this frequency range was similar to the one at a frequency of 5 Hz, in terms of building heights. In areas with high spectral acceleration under this frequency, 1-story buildings can be at high risk to life and property.

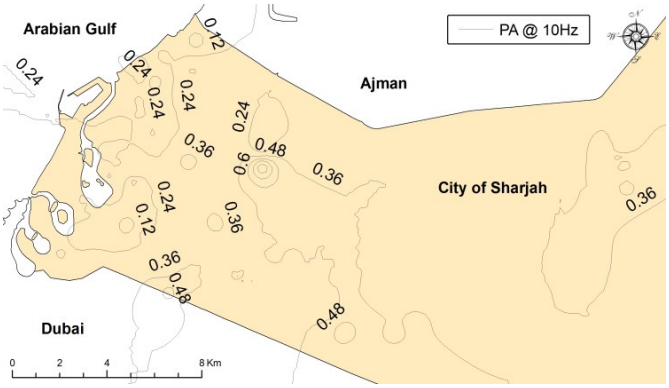

Figure 9. Spectral Acceleration Map of the City of Sharjah at 10 Hz

Distribution of Frequency at PSA

Figure 10 shows the frequency distribution at which maximum amplification is likely to take place. The map indicates three different zones of frequencies. First, the frequency range of 2.0 Hz to 5.0 Hz, where most of the city is under and site amplification might take place. This frequency range corresponds to 2- to 4-story buildings. In the city of Sharjah, these types of buildings are dominant and most likely affected by the presumed earthquake scenario presented in this study. Second, the frequency zone that is at a relatively lower risk ranges between 1.75 Hz to 2.5 Hz, which corresponds to 4- to 5-story buildings. Third, tall and high-rise buildings at a frequency of 1 Hz or less are considered outside the range for the peak spectral acceleration.

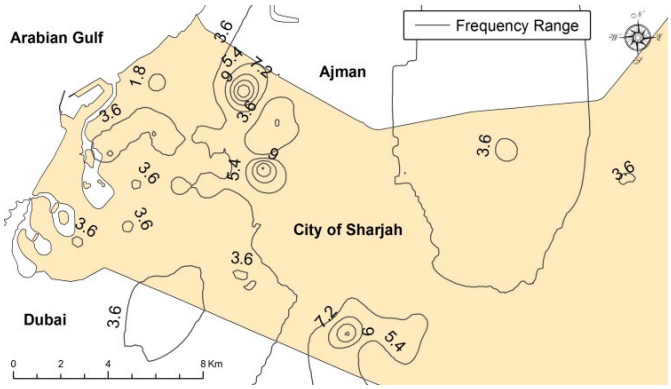

Figure 10. Frequency Range of Peak Ground Acceleration for the City of Sharjah (in Hz)

Conclusion

This study looked at a local site-specific ground response analysis, which is an important step in estimating the effects of earthquakes. The analysis used a one-dimensional ground response, modeled using SHAKE2000. Soil data from 387 boreholes were collected in order to develop local site amplification potential maps for the city of Sharjah. Furthermore, the researchers utilized a Geographical Information System (GIS) to create amplification potential and surface response spectra maps at various locations in Sharjah. These maps show zones of high vulnerability earthquake risk that can be used for earthquake-resistant design of structures.

The city of Sharjah was divided into four zones, according to the amplification factor, which ranged from 1.2 to 3.0. In Zone IV, a high amplification factor was found near the west region of the city, while the rest of the city lies in Zone I with amplification factors of 1.2 to 1.7. Response spectra at the ground surface obtained for all borehole sites showed a wide range of spectral acceleration at different frequencies. The range for spectral acceleration at 0.5 Hz was between 0.04g to 0.07g; at 2 Hz, it was in the range of 0.06g to 0.5g; at 5 Hz, it was in the range of 0.05g to 0.9g; at 10 Hz, it was in the range of 0.06g to 0.55g.

Most of the city lies in the frequency range of 2.0 Hz to 5.0 Hz, where site amplification will take place. This frequency range corresponds to 2- to 4-story buildings. In the city of Sharjah, these types of buildings are dominant and most likely affected by the presumed earthquake scenario presented in this study.

The reader is cautioned that the results presented in this paper were based on a limited soil sample. Prior to implementation in the field, further analysis using more soil data covering the entire city would need to be conducted. Finally, this work can be further improved by utilizing the dynamic properties of soil in this type of analysis.

References

[1] Boominathan, A., & Kumar, S. K. (2010). A Site Specific Study on evaluation of design Ground Motion Parameters. *International Journal of Geotechnical Earthquake Engineering*, *1*(1),1-25.

[2] Hunter, J. A., Benjumea, B., Harris, J. B., Miller, R. D., Pullan, S. E., Burns, R. A. et al. (2002). Surface and down hole shear wave seismic methods for thick soil site investigations. *Soil Dynamics and Earthquake Engineering*, *22*, 931-941.

[3] Ince, G. C. (2011). The relationship between the performance of soil conditions and damage following an earthquake: a case study in Istanbul, Turkey. *Natural Hazard and Earth system Sciences*, *11*, 1745-1758.

[4] Schnabel, P. B., Lysmer, J., & Seed, H. B. (1972). *SHAKE: A computer program for earthquake response analysis of horizontally layered sites*. Report No. EERC 72/12, Earthquake Engineering Research Center, University of California, Berkeley.

[5] Jamal, A., & A-Homoud, A. S. (2004). Seismic hazard assessment of United Arab Emirates and its surroundings, *Journal of Earthquake Engineering, Imperial College Press*, *8*(6), 817-837.

[6] UNESCO (1983). *AFESD and IDB assessment and mitigation of earthquake risk in the Arab region*. UNESCO Report.

[7] Malkawi, A. I. H., Barakat, S., Shanableh, A., Al Bdour, W., Omar, M., & Altoubat, S. (2007). *Seismic Hazard Assessment and Mitigation of Earthquake Risk in the United Arab Emirates*. Published Jointly by Jordan University of Science and Technology and the Deanship of Research and Higher Studies, University of Sharjah, United Arab Emirates.

[8] Lyisan, R. (1996). Correlations between Shear Wave Velocity and In-Situ Penetration Test Results. *Teknik Dergi Journal*, *2*(2), 1187-1199.

[9] Joyner, W. B., & Boore, D. M. (1988). Characterization and Prediction of Strong Ground Motion. *Proceedings of Earthquake Engineering and Soil Dynamics II GT Div/ASCE*, Utah, June.

[10] Atkinson, G. M., & Boore, D. M. (1997). Some comparisons between recent ground-motion relations. *Seism. Res. Lett*., *68*, 24-40.

[11] Al Bodour, (2005). *Seismic Hazard Assessment and Mitigation of Earthquake Risk in United Arab Emirates*. Unpublished Master's thesis, University of Science and Technology, Jordan.

Biographies

MAHER OMAR is an Associate Professor of Geotechnical Engineering and currently the Chairman of Civil and Environmental Engineering Department at the University of Sharjah. He earned his Ph.D. (1995) degree from Southern Illinois University, USA. His research interests include Soil Stabilization using Synthetic Fibers, Landfill Analysis & Design, Soil Remediation, Soil Liquefaction, Machine Foundation, Sustainable Development, and Engineering Education. Dr. Omar may be reached at momar@sharjah.ac.ae

ABDALLAH SHANABLEH is a Professor of Environmental Engineering and Management at the at University of Sharjah. He earned his Ph.D. (1990) from University of Texas at Austin, USA. His research interests are in Waste Management, Water and Wastewater Treatment, Risk Analysis, transportation, waste disposal, and water supply, and Sustainable Development. Dr. Shanableh may be reached at shanableh@sharjah.ac.ae

MUHSIN BALWAN received the B.Sc. and M.Sc. degrees in civil engineering both from the University of Sharjah, United Arab Emirates. He currently the Director of Traffic Engineering Department at Sharjah Directorate of Public Works. He is also a member of Sharjah National Disaster and Crises Management Team. Eng. Balwan may be reached at binbalwan@hotmail.com

MOHAMMED FATTAH is a Professor of Building and Construction Engineering Department at University of Technology, Iraq. He earned his Ph.D. (1999) degree from University of Baghdad, Iraq. His research interests are Soil Dynamics, Pile Foundations, Soil Improvement, and Finite Elements. Dr. Fattah may be reached at myf_1968@yahoo.com

KHALED HAMAD is an Assistant Professor in the Department of Civil & Environmental Engineering, University of Sharjah, United Arab Emirates, where he heads the Traffic and Road Safety Institute. He received his Ph.D. degree from University of Delaware, USA. His research interests are in Intelligent Transportation Systems with emphasis on the applications of Geographic Information Systems, artificial intelligence, and soft computing techniques in transportation. Dr. Hamad may be reached at khamad@sharjah.ac.ae

VARIABLE TIMING CONTROL FOR ARCP VOLTAGE SOURCE INVERTERS OPERATING AT LOW DC VOLTAGE

Todd D. Batzel, Penn State Altoona; Kipp Adams, Penn State Altoona

Abstract

The Auxiliary Resonant Commutated Pole (ARCP) inverter has been of interest in motor drive applications that can benefit from any combination of increased conversion efficiency, reduced EMI radiation or higher PWM switching frequency. The ARCP inverter achieves high efficiency by turning the main switches on or off only under zero-voltage conditions. This reduces switching losses in the main circuit and potentially increases overall conversion efficiency. Furthermore, the reduced loss in the main switch allows for higher switching frequencies, which is of benefit for ironless low-inductance motors that are widely being used in small- to medium-power vehicle propulsion applications. The soft-switching ARCP generates an output with significantly reduced *dv/dt* and *di/dt* as compared to hard-switched inverters, which tends to reduce EMI emissions. All of these attributes of the soft-switching ARCP are beneficial in electric propulsion or electric vehicle auxiliary applications. In the ARCP inverter, the control signal timing for main and auxiliary switches is critical for maintaining the most favorable operating conditions. Many ARCP implementations utilize variable-timing control, where load current polarity and magnitude are used to determine the control signal timing–usually without additional sensors. In this study, the timing of main and auxiliary switching was examined for low dc bus voltage operation. A variable-timing methodology for ARCP switching was developed specifically in order to address issues associated with low-voltage ARCP operation. The operation principles are described here along with simulation and experimental results to demonstrate the approach.

Introduction

Auxiliary Resonant Commutated Pole (ARCP) technology was developed with the initial intent of reducing switching losses in the main switching devices of power conversion systems by switching them on or off only under zero-voltage conditions [1]. This soft-switching strategy also was intended to yield benefits such as reduced EMI emission [2-4] and permit operation of the switches at increased switching frequencies.

Although the adoption of the ARCP inverter tends to increase the overall cost and complexity of a drive system, its potential benefits make the ARCP of interest in a variety of electric vehicle (EV) applications. The ARCP inverter was proposed for electric vehicle propulsion by Dong et al. [5] and Morii et al. [6]. Dong et al. [5] demonstrated a significant efficiency benefit for an EV application with the use of an ARCP inverter operating with a DC bus voltage of 324 V. Similar results were obtained by Morii et al. [6] when they used an ARCP inverter suitable for high-power EVs.

There are two basic approaches used to generate the ARCP auxiliary and main switch control signals—fixed and variable timing. For the fixed-timing implementation, all switching times signals are generated using preset, constant values. Thus, fixed timing is easy to implement and has been shown to perform well over a limited range of load currents. However, fixed timing cannot produce zero-voltage switching (ZVS) for a wide load-current range. Variable-timing control was introduced by Chan et al. [7] to address this shortcoming of fixed timing, and uses the instantaneous load current to generate the switching signals that yield ZVS across the load-current range. Several studies have demonstrated improved ARCP efficiency for variable-timing control compared with the fixed-timing approach, with the increased performance coming at the expense of higher complexity [8-10]. Although voltage sensors placed across the switching devices are sometimes used to assist in ZVS implementation [11], their use significantly increases cost and complexity. Therefore, voltage sensors are generally avoided so that switching times must be determined in real-time using the circuit model and measured load current.

Although switching methodologies for ARCP inverters have been examined in the literature, published works in this area are aimed at high-voltage applications. In one such case, an ARCP inverter operating at 700 vdc showed improvement in efficiency when variable-timing control methods were employed [12]. In this current paper, the authors identify some of the issues that are specifically associated with low-voltage operation of the ARCP, and present a technique for implementation of variable-timing control under low-voltage conditions. In this study, simulations were performed and a prototype ARCP was operated at rela-

tively low voltages in order to demonstrate operation of the low-voltage system. The low-voltage range (24-42 V) is appropriate for small-vehicle propulsion applications and electric-vehicle auxiliaries such as power-steering assist.

ARCP Principle of Operation

The principle concept of the ARCP inverter is to force the voltage across main switches to be nearly zero volts before toggling their state. This has the effect of reducing the switching loss as compared to standard hard-switched configurations. An ARCP inverter configuration used to achieve this zero-voltage switching (ZVS) is shown in Figure 1 and it consists of two snubber capacitors (C_{r1} and C_{r2}) and a resonant branch added to a standard hard-switched pole. The resonant branch contains two auxiliary switches, *SP* and *SS*, for pumping current into or sinking current from the pole, respectively. Both the pump (*SP*) and sink (*SS*) auxiliary switches include anti-parallel diodes and a resonant inductor, L_r. The main pole was constructed with the main switches *S1* and *S2*, their associated flyback diodes and the aforementioned snubber capacitors.

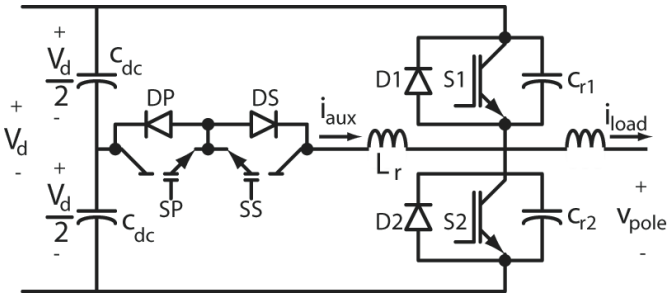

Figure 1. ARCP Pole Configuration

In order to operate the ARCP with the same conventional controllers as hard-switched inverters, the ARCP interface should be compatible with the standard PWM signals that are widely used in electric-machine control systems. The signals required to control the ARCP are shown in Figure 2, where the PWM input signal triggers the start of an ARCP state transition. Here, it is assumed that a logical 1 at the PWM input should deliver full DC bus voltage (V_d) to the pole output (V_{pole}), while a logical 0 should produce 0 V at the pole output.

In a hard-switched inverter, a rising PWM input signal turns off the lower switch (*S2*) and, following a short dead time, turns on the upper switch (*S1*). Similarly, a falling PWM input signal first turns off *S1*, then turns on *S2*. For ARCP soft-switching, where load current is to be commutated from a power switch to a diode (e.g., from *S1* to *D2* or *S2* to *D1*; see Figure 1), the hard-switched sequence can be used to obtain ZVS if the load-current magnitude is sufficient to charge or discharge the pole voltage from its current state to the opposite rail within switching time constraints. Otherwise, the auxiliary circuit must be used to introduce enough current to assist with the charge/discharge of the resonant capacitor. When switching load current from a diode to a switch or when load-current magnitude is small, the auxiliary circuit will always be used to assist the capacitor charge/discharge.

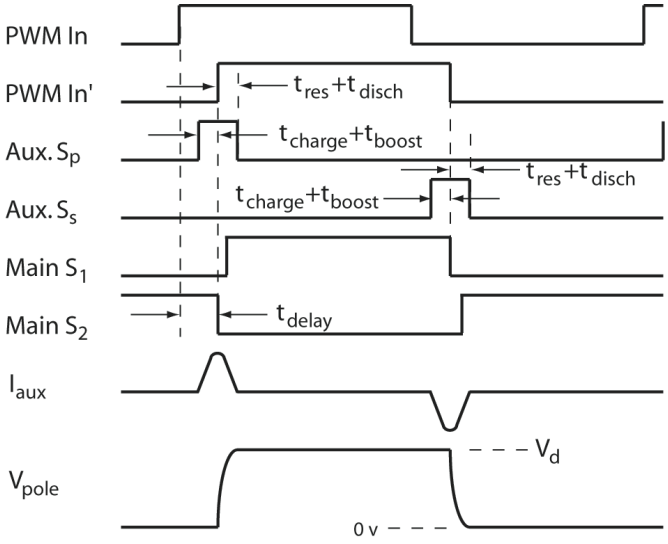

Figure 2. ARCP Signal Timing

Referring to Figure 2, ARCP operation when auxiliary current assist is necessary to commutate the load current from the lower diode (*D2*) to the upper switch (*S1*) is described as follows, where a positive load current i_{load} is assumed. A rising edge of the PWM input signal triggers the auxiliary pump switch (*SP*) so that the resonant inductor begins to charge. The time to charge the resonant inductor to the required current level (t_{charge} + t_{boost}) is variable and depends on the load-current level as well as the necessary boost current. When the auxiliary current (i_{aux}) magnitude exceeds the load current by a sufficient margin, called the boost current, i_{boost}, the bottom switch *S2* is turned off. With *S2* off, the boost current charges and discharges snubber capacitors C_{r2} and C_{r1}. In this case, the pole output voltage, v_{pole}, rises, while the slope of the auxiliary current decreases, eventually becoming negative. When C_{r1} is fully discharged, the upper switch, *S1*, is turned on at zero voltage. The resonant inductor continues to discharge toward zero current, at which point it will be turned off under zero-current conditions. The transitions for commutating load current from the upper switch (*S1*) back to the lower diode (*D2*) are similar.

Referring once again to Figure 2, it can be seen that for ARCP operation, the state change for the main switches occurs after some delay due to the resonant inductor charge time ($t_{charge} + t_{boost}$). To accommodate the maximum possible resonant inductor charge time delay, and to maintain compatibility with PWM controllers, a delayed PWM signal (PWM In') is generated. Therefore, the PWM input and delayed PWM input are offset by a delay (t_{delay}) corresponding to the maximum possible resonant inductor charge time, which has been expressed by Jiang [13] as:

In Equation (1), ${}'I_{aux}$ is the maximum auxiliary current level required for the inverter operation, which is the rated load current plus the required boost current. Similarly, the required ramp time for charging the resonant inductor based on the variable load current is often determined using Equation (2):

$$t_{delay} = \frac{2{}'I_{aux}L_r}{V_d} \tag{1}$$

$$t_{charge} + t_{boost} = \frac{2L_r}{V_d}\left(i_{load} + i_{boost}\right) \tag{2}$$

For variable-timing ARCP implementations, accurate prediction of the auxiliary current and pole output voltage state is essential for achieving zero-voltage (for main switches) or zero-current (for auxiliary devices) switching and, therefore, exploiting the ARCP benefits. For example, if the predicted auxiliary circuit charge time, ($t_{charge} + t_{boost}$), is longer than necessary, the resonant inductor will charge to an unnecessarily high current level resulting in increased auxiliary circuit conduction losses. Similarly, if the predicted auxiliary circuit charge time is shorter than necessary, the resonant inductor current may be insufficient to commutate the snubber capacitors to the opposite rail, and ZVS cannot be achieved.

The direct measurement of the auxiliary current is not easily or inexpensively incorporated into the ARCP controller. Therefore, for purposes of generating necessary timing signals, the auxiliary current dynamics are often computed [14] using Equation (3):

$$\frac{di_{aux}}{dt} = \frac{V_d - 2V_{pole}}{2L_r} \tag{3}$$

Likewise, in the absence of a voltage sensor, the voltage dynamics are characterized using the solution of Equation (3) along with the load-current measurement shown in Equation (4).

$$\frac{dv_{pole}}{dt} = \frac{1}{2c_r}\left(i_{aux} - i_{load}\right) \tag{4}$$

Low-Voltage ARCP Operation

In this section, the operation of the ARCP at low voltages is illustrated. Important aspects of operating the ARCP at low voltages are described along with the consequences of low-voltage operation relative to timing signal generation. Simulations are then used to substantiate the analysis.

Low-Voltage ARCP Operating States

For ARCP analysis and modeling, ideal-power switching device models have typically been used since, in high-voltage ARCP operation, those power device non-idealities are insignificant relative to the high operating DC bus voltage. For low-voltage operation, however, those power switch characteristics must be included in order to obtain ZVS through prediction of switching times. ARCP operation is now described using Figures 3 and 4, which show the ARCP signals and states, and the corresponding circuit for each state, respectively. In the interest of brevity, only a positive transition of the PWM input is considered. The load current is assumed to be positive so that the auxiliary circuit assist is necessary.

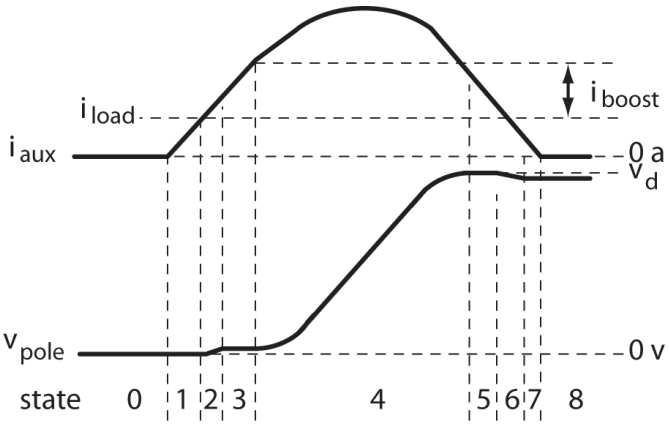

Figure 3. ARCP Signal Timing States, Including Switch Drops

The initial operating point in Figure 3 is state 0, which is a steady-state condition where *S2* is gated on, and *S1* off. Due to the load-current direction, diode *D2* is conducting the full load current, and the pole voltage output is the diode voltage drop, $-V_{d2}$. In this state, the auxiliary current is non-conducting and the resonant capacitors, C_{r1} and C_{r2}, are charged to V_d+V_{d2} and -V_{d2}, respectively.

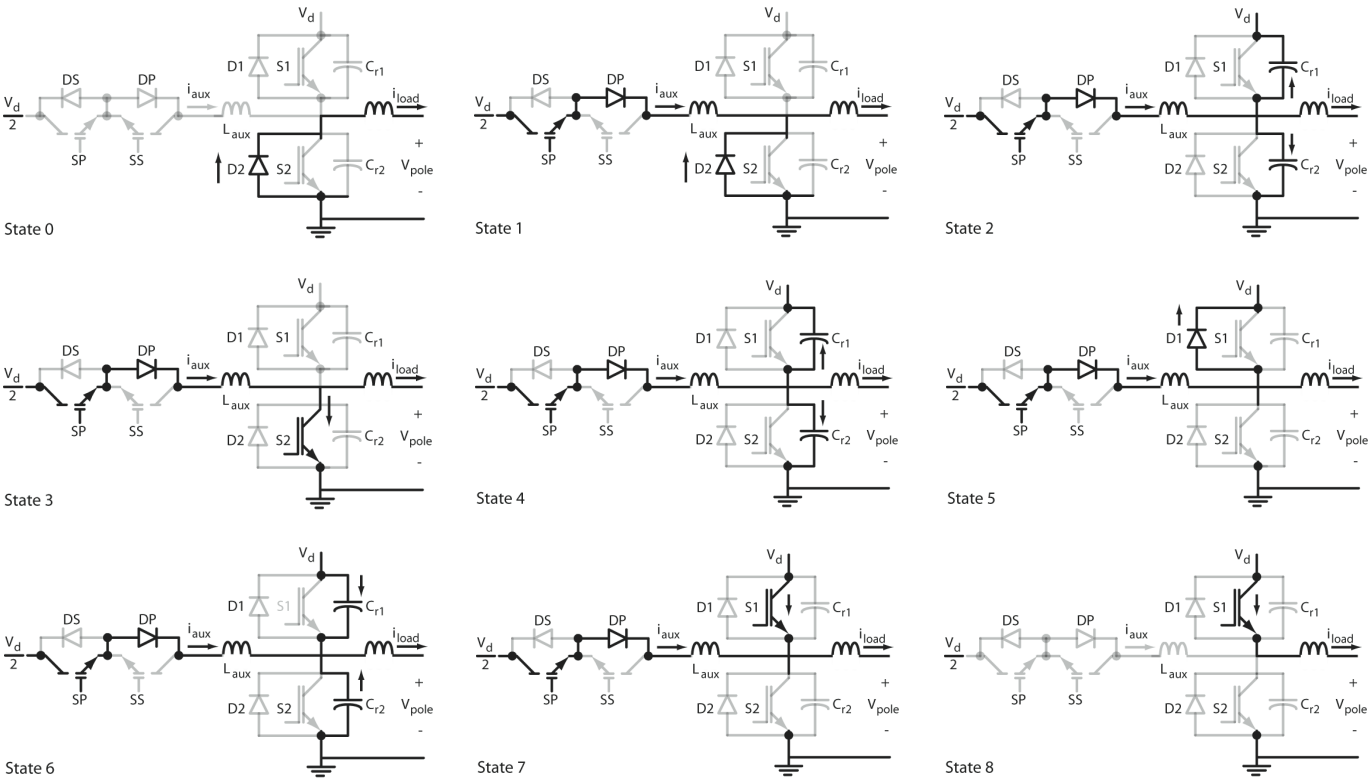

Figure 4. ARCP Turn-On States for Positive Load Current

The auxiliary pump switch (*SP*) turn-on marks the transition to state 1, as shown in Figure 3. Note in Figure 2 that there is an interval of between the PWM input edge and the auxiliary pump switch turn on. This interval depends on the amount of auxiliary current needed at the present operating point. In state 1, the resonant inductor will charge according to Equation (5), where v_{sa} and v_{da} represent the on-voltage drops of auxiliary circuit switches and diodes, respectively. As shown in Figure 4, the pole voltage in state 1 is clamped by load-current flow in *D2* to yield Equation 6.

$$\frac{di_{aux}}{dt} = \frac{1}{L_r}\left(\frac{v_d}{2} - \text{sgn}(i_{aux})(v_{sa} + v_{da}) - v_{pole}\right) \qquad (5)$$

$$\frac{dv_{c2}}{dt} = \frac{dv_{pole}}{dt} = 0 \qquad (6)$$

It is important to note the difference between Equation (5) and its approximation in Equation (3) that is often used for ARCP analysis. For high dc bus voltages, Equations (3) and (5) yield very similar results. However, for low dc bus voltages, their outcomes may differ significantly. State 1 persists until i_{aux} exceeds i_{load} and the ARCP transitions to state 2. At this point, diode *D2* turns off, and the difference between i_{aux} and i_{load} begins to charge c_{r2} until the capacitor voltage reaches the minimum turn-on voltage of the main switch, *S2*, which is $v_{ce,sat}$. In state 2, the auxiliary current is governed by Equation (5), while the pole voltage is described by Equation (4).

The changeover from state 2 to 3 occurs when c_{r2} is charged so that the main switch *S2* begins to conduct. In state 3, the main switch, *S2*, conducts the difference between the auxiliary and load current until this difference reaches a level (i_{boost}) sufficient to charge the resonant capacitor, c_{r2}, to the positive rail. In this state, the auxiliary current and pole-voltage equations obey Equations (5) and (6). When the resonant inductor is charged to the specified boost current level, *S2* is turned off and the ARCP transitions to state 4, as shown in Figures 3 and 4. With *S2* turned off, the boost current charges the resonant capacitors according to Equation (4), while the auxiliary current follows Equation (5). The timing for the turn-off of *S2* (or start of state 4) is of great importance: if it is turned off too late, unnecessary boost current and losses are introduced, while if it is turned off prematurely, it may not be possible for the resonant capacitor to be charged to the positive rail.

In state 4, as resonant capacitor c_{r2} charges, the auxiliary current will be reduced in slope according to Equation (5). It is also important to note that for auxiliary circuit pumping, the magnitude of di_{aux}/dt for rising versus falling auxiliary current will be different due to the voltage drops in the auxiliary and main switches. Thus, the auxiliary current charge and discharge will not be symmetric as originally predicted by Equation (3). The effect will be similar for auxiliary current sinking, during transitions from the upper diode (*D1*) to the lower switch (*S2*). For transitions from the upper switch (*S1*) to the lower diode (*D2*) at light positive load currents, or from the lower switch (*S2*) to the upper diode (*D1*) for light negative load currents, the asymmetry is even more pronounced. The asymmetry has implications in the calculation of optimum switching times for the auxiliary pump cycle that has not been addressed in previous works.

A transition to state 5 occurs when the pole voltage is fully charged and the boost current turns on *D1*. At (or near) this point, upper switch S1 can be turned on at zero voltage. Note, however, that *S1* will not conduct current until its turn -on voltage, $v_{ce,sat}$, is reached. In state 5, the auxiliary current continues to ramp toward zero according to Equation (5), and the pole voltage is determined from Equation (6). When i_{aux} falls below i_{load}, *D1* turns off and the difference in these currents will charge upper resonant capacitor c_{r1} until the turn-on voltage of *S1* is met. This corresponds to state 6 in Figures 3 and 4. In state 6, the pole voltage and auxiliary current are represented by Equations (4) and (5), respectively.

State 7 begins when c_{r1} is charged to a level sufficient to allow *S1* to begin conducting. In state 7, the load current is increasingly provided through *S1* as i_{aux} continues to decay toward zero. For this state, the pole voltage and auxiliary current are modeled by Equations (6) and (5), respectively. When i_{aux} fully discharges, marking the end of state 7, its control signal may be turned off at zero current. Since the auxiliary circuit will not conduct in the opposite direction (with *SS* off), this timing is not critical as long as the gate turn-off signal is applied *after* full discharge. When the resonant inductor is fully discharged, there is a transition to state 8, as shown in Figures 3 and 4. State 8 represents a steady state where switch *S*1 is on, *S*2 is off, the auxiliary current is again disabled and the output pole voltage is v_d-v_{s1} (for positive load current). The system will remain in state 8 until the input PWM signals the need to commutate the load current from the upper switch (*S1*) to the lower diode (*D2*).

A similar sequence was used to go from state 8 back to state 0 (upper switch to lower diode) for negative load current or small positive load current–the difference is that the auxiliary circuit branch sinks current in this case by turning on switch *SS*. However, similar procedures can be easily applied to identify state transitions for this case. In the interest of brevity, the details of these state transitions are not included in this discussion. For sufficiently negative load current, it is not necessary to use the auxiliary branch to commutate current from the lower diode to the upper switch since the load current itself can be used to charge the resonant capacitors to the opposite rail. Similarly, for sufficient positive load current, it is not necessary to use the auxiliary branch to sink current when transitioning from the upper switch to the lower diode.

Low-Voltage ARCP Experimental Results

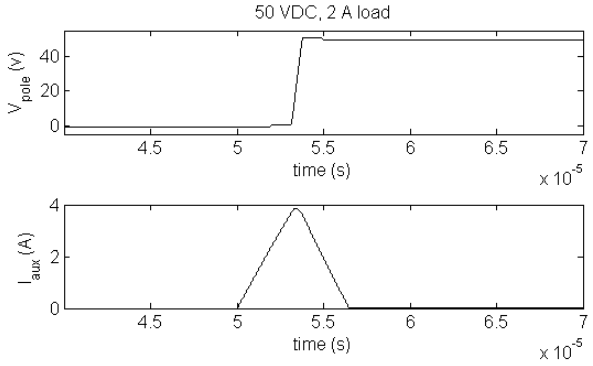

Figure 5. ARCP Simulation at 50 vdc and Pos. Load Current

In order to analyze low-voltage ARCP operation, a circuit simulation was performed. Example simulation results are shown in Figure 5, which shows operation at 50 vdc bus, and a positive load current of 1A. The simulation demonstrates some of the aspects of low-voltage ARCP operation as described previously. For example, the auxiliary current is asymmetric (auxiliary current rising slope is less than falling slope), as predicted by Equation (5).

Finally, to confirm simulations, an ARCP inverter pole pair (in H-bridge configuration) was constructed using IGBTs as the main switch and MCTs as the auxiliary switch. The system was programmed using variable-timing control. An example waveform showing auxiliary current and pole voltage from the experimental system is shown in Figure 6 for a positive load current of 1A and a dc bus voltage of 50 V. The experimental results show the same characteristics as the simulation.

Variable-Timing Control

In this section, the ARCP pole output voltage and auxiliary current signals are characterized for each ARCP state, and general solutions for the timing associated with each

state are developed. This analysis forms the basis for the variable-timing control of the ARCP.

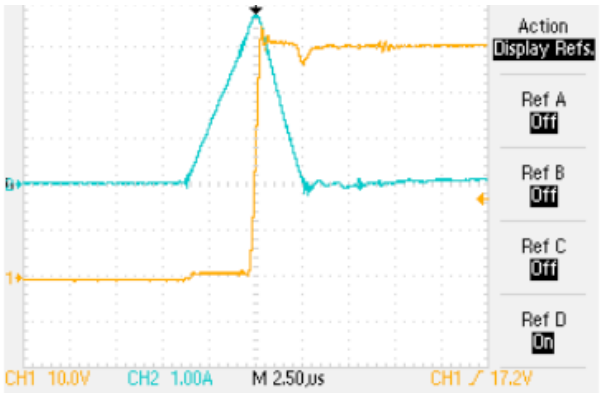

Figure 6. Experimental ARCP Aux. Current and Pole Voltage

ARCP Circuit Timing Analysis

The ARCP states shown in Figures 3 and 4 included two distinct operating modes. For states 2, 4 and 6, the circuit was in resonance mode. In states 1, 3, 5 and 7, the output voltage was clamped at some known value. Each of these operating modes of the ARCP was then analyzed to characterize the circuit timing.

1) *Resonant Circuit Timing Analysis*: The circuit was then analyzed for the resonant mode. The solution yielded timing characteristics for states 2, 4 and 6. Applying KCL to the circuit model for resonant mode shown in Figure 7 yielded Equations (7) and (8):

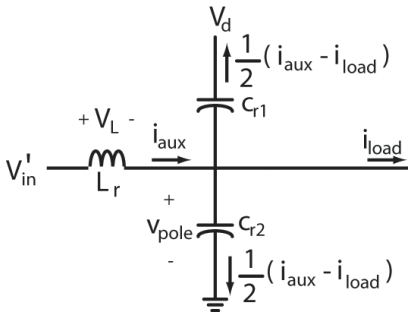

Figure 7. ARCP Equivalent Circuit for Resonance

$$V'_{in} - L_r \frac{di_{aux}(t)}{dt} - \frac{1}{2C_r}\int \left(i_{aux}(t) - i_{load}\right)dt = 0 \qquad (7)$$

$$V'_{in} = \frac{V_d}{2} - \text{sgn}\left(i_{aux}\right)\left(V_{da} + V_{sa}\right) - V_{pole,init} \qquad (8)$$

where $V_{pole,init}$ is the pole voltage at the start of each ARCP state, and V_{da} and V_{sa} represent the voltage drops across the auxiliary circuit diode and switch, respectively. The solution to Equation (7) is shown by Equation (9)

$$i_{aux}(t) = A\sin\left(\omega_0 t + \phi\right) + i_{load,init} \qquad (9)$$

where Equations (10) and (11) are

$$\omega_0 = \sqrt{\frac{1}{2L_rC_r}} \qquad (10)$$

$$A = \sqrt{\frac{2C_r}{L_r}V'^2_{in} + \left(i_{aux,init} - i_{load}\right)^2} \qquad (11)$$

and $i_{aux,init}$ represents the auxiliary current at the start of the ARCP state of interest. Also,

$$\phi = \sin^{-1}\left(\frac{i_{aux,init} - i_{load}}{A}\right) \quad \text{for } V'_{in} \geq 0 \qquad (12)$$

or

$$\phi = \pi - \sin^{-1}\left(\frac{i_{aux,init} - i_{load}}{A}\right) \quad \text{for } V'_{in} < 0 \qquad (13)$$

With the auxiliary current known from Equation (9), the pole voltage output can be determined from Equation (14):

$$V_{pole}(t) = V'_{in} - L_r\frac{di_{aux}}{dt} \qquad (14)$$

Differentiating Equation (9) and plugging it into Equation (14) gives us

$$V_{pole}(t) = V'_{in} - B\cos\left(\omega_0 t + \phi\right) + v_{pole,init} \qquad (15)$$

where

$$B = \sqrt{V'^2_{in} + \frac{L_r}{2C_r}\left(i_{aux,init} - i_{load}\right)^2} \qquad (16)$$

Finally, Equation (15) was solved for each possible time for which the pole voltage, $V_{pole}(t)$ would take on the value $\overline{V}_{pole}$, given the initial conditions; see Equation (17):

$$t_{rv} = \frac{1}{\omega_0}\left[\pm\cos^{-1}\left(\frac{V'_{in} + v_{pole,init} - \overline{V}_{pole}}{B}\right) - \phi + 2\pi n\right] \qquad (17)$$

This yielded (for n=0, 1, 2, …) all possible times for which the pole voltage would have the specified magnitude. For

the ARCP application where resonance is not sustained, the authors were interested in the solution with the smallest positive time from Equation (17).

2) *Clamped Circuit Timing Analysis*: For ARCP states 1, 3, 5 and 7, the output voltage of the ARCP was clamped so that the circuit was not in resonance. With the voltage clamped, one can easily solve for the time required for the auxiliary current to reach a target value, $\bar{I}_{aux}$, given the initial condition of Equation (18):

$$t_{ci} = \frac{L_r\left(\bar{I}_{aux} - i_{aux,init}\right)}{V'_{in}} \tag{18}$$

Variable Timing

Using the solutions from the previous section, each of the ARCP states described in Figures 3 and 4 were then analyzed to quantify their respective state times. By knowing the timing characteristics of each state, the required switching times for the main and auxiliary switches can be predicted and applied to variable-timing control. It should be noted, once again, that the following analysis was performed for a positive load current and for the commutation of current from the lower diode (*D2*) to the upper switch (*S1*). Other transitions can be analyzed using the same procedure.

ARCP state 1 has the output voltage clamped to $-v_{d2}$, an initial auxiliary current of zero, and a target auxiliary current equal to the load current. Therefore, Equation (18) was used to find the total time required for ARCP state 1:

$$t_1 = \frac{L_r i_{load}}{v'_{in}} \tag{19}$$

ARCP state 2 was a resonant state where the initial pole voltage was $-v_{d2}$, and the pole voltage at the end of this state would be v_{s2}. Therefore, Equation (17) was used to determine the total time required for ARCP state 2:

$$t_2 = \frac{1}{\omega_0}\left[\pm\cos^{-1}\left(\frac{V'_{in} - v_{D2} - v_{ce,sat}}{B}\right) - \phi + 2\pi n\right] \tag{20}$$

Once the total time for state 2 was determined, it could be used with Equation (9) to find the auxiliary current at the end of state 2:

$$i_{aux}(t'_2) = \sqrt{\frac{2C_r}{L_r}V'^2_{in}}\,\sin\left(\omega_0 t_2\right) + i_{load} \tag{21}$$

For ARCP state 3, the resonant capacitor was clamped by a conducting *S2*. The initial auxiliary current was given by Equation (21), and the final auxiliary current was the load current plus the required boost current. Thus, using Equation (19) gives:

$$t_3 = \frac{L_r\left(i_{load} + i_{boost} - i_{aux}(t'_2)\right)}{V'_{in}} \tag{22}$$

Next, ARCP state 4 was examined, for which the pole voltage resonates from an initial value of v_{s2} to a final value of $v_d + v_{d1}$. From Equation (17), it was found that

$$t_4 = \frac{1}{\omega_0}\left[\pm\cos^{-1}\left(\frac{V'_{in} + v_{s2} - (v_d + v_{d1})}{B}\right) - \phi + 2\pi n\right] \tag{23}$$

The corresponding auxiliary current at the end of t_4 was

$$i_{aux}(t'_4) = \sqrt{\frac{2C}{L_r}V'^2_{in} + i^2_{boost}}\,\sin\left(\omega_0 t_4 + \phi\right) + i_{load} \tag{24}$$

For ARCP state 5, the auxiliary current decayed from its initial value given by Equation (24) to a final value that was equal to the load current. During this time, the pole voltage was clamped to the DC bus voltage plus the diode voltage drop. The time for auxiliary current to decay is

$$t_5 = \frac{L_r\left(i_{load} - i_{aux}(t'_4)\right)}{V'_{in}} \tag{25}$$

The total time for ARCP state 6 was computed using Equation (17) from the initial pole voltage of $v_d + v_{d1}$ to its value when upper switch *S1* begins to conduct, which was $v_d - v_{ce,sat}$.

$$t_6 = \frac{1}{\omega_0}\left[\pm\cos^{-1}\left(\frac{V'_{in} + v_{D1} + v_{ce,sat}}{B}\right) - \phi + 2\pi n\right] \tag{26}$$

The auxiliary current at the end of t_6 was obtained from the auxiliary current at the start of the state, which was i_{load}:

$$i_{aux}(t'_6) = \sqrt{\frac{2C_r}{L_r}V'^2_{in}}\,\sin\left(\omega_0 t_6 + \phi\right) + i_{load} \tag{27}$$

Finally, ARCP state 7 time, where the auxiliary current ramps to zero with the pole voltage clamped at $v_d - v_{ce,sat}$ was computed using Equation (18):

$$t_7 = \frac{L_r\left(-i_{aux}(t'_6)\right)}{v'_{in}} \tag{28}$$

At the end of state 7, the auxiliary switch was turned off at zero current and the ARCP was in a steady state with the upper switch (*S1*) conducting the full load current.

Variable-Timing Control for Low-Voltage ARCP

Lai et al. [11] showed that variable-timing control of the ARCP was critical for optimizing the inverter performance–specifically in minimizing losses in the power switching components and avoiding damaging transient currents. The ARCP timing results from the previous section were then used to determine optimum switching times for auxiliary and main switches.

Referring to Figure 2, the fixed delay time, t_{delay}, between the input PWM signal transition and the turn off of main switch *S2* first had to be computed. This delay is necessary to allow sufficient time for the auxiliary current to reach its required level before switching the state of any main switches. Although Equation (1) has been used in the literature, it may not allow sufficient time when considering voltage drops in the auxiliary circuit. Therefore, a more accurate computation applicable to low-voltage ARCP operation would be given as Equation (29):

$$t_{delay} = \frac{L_r \hat{I}_{aux}}{0.5v_d - v_{sa} - v_{da}} \tag{29}$$

Next, referring to Figure 2, auxiliary switch *SP* is turned on, $t_{charge} + t_{boost}$, before main switch *S2* is turned off. Noting that t_{charge} and t_{boost} correspond to ARCP states 1-3, the time from the PWM-In signal until the auxiliary switch *SP* is turned on was determined by Equation (30):

$$t_{SP,ON} = t_{delay} - \sum_{n=1}^{3} t_n \tag{30}$$

From Figure 2, it can be seen that the lower switch (*S2*) is turned off exactly t_{delay} after the PWM In signal:

$$t_{S2,OFF} = t_{delay} \tag{31}$$

The upper switch (*S1*) can be turned on at zero voltage at

$$t_{S1,ON} = t_{delay} + t_4 \tag{32}$$

Finally, the auxiliary pump switch, *SP*, can be turned off at zero current no sooner than

$$t_{SP,OFF} = t_{delay} + \sum_{n=4}^{7} t_{state\ n} \tag{33}$$

ARCP Simulation Results

In this section, the ARCP timing analysis presented previously is compared with more traditional variable-timing approaches. In addition, simulations of a low-voltage variable-timing ARCP inverter using these results are performed.

Variable-Timing Comparison

The ARCP variable-time computation methodology presented in the previous section was then compared to other techniques that have been reported in the literature. The results are summarized in Figure 8. For purposes of comparison, the resonant inductor and capacitor values were adjusted in proportion, and in inverse proportion to the dc voltage, respectively, so that the calculated times would be constant using the conventional calculation method.

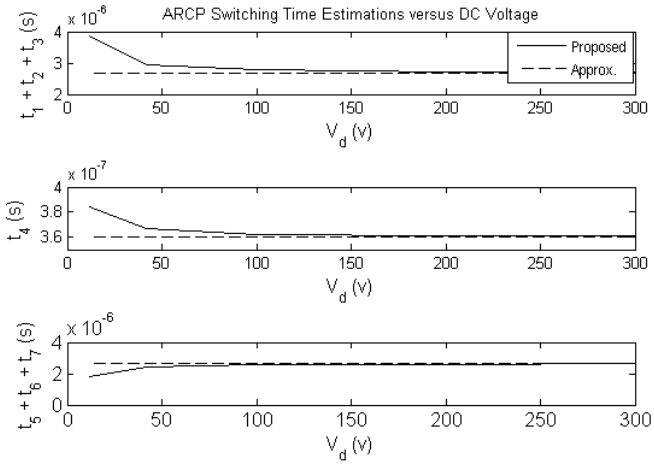

Figure 8. Switching Time Calculations for 1A Load

The first variable-timing parameter to be compared was the time required for the auxiliary current to be charged to the load current plus the required boost current level. In this study, that time corresponded to $t_1 + t_2 + t_3$, from Equations (19), (20) and (22), whereas other published works [15], [16] used Equation (2). Figure 8 shows that these two computations produce results that correspond closely at high dc bus voltages, yet diverge significantly at low voltages due to the significance of device non-idealities that are not considered in Equation (2). The significance of this computation is that it is used to determine the time at which the lower switch is to be turned off in order to end the charging of the auxiliary inductor. Too short a charge time could result in insufficient boost current to resonate the pole output voltage to the opposite rail, whereas too long a charging time would yield excessive boost current that could unnecessarily in-

crease the total ARCP commutation time and increase the conduction losses.

Next, the resonant time (t_4), as described in Equation (23), was compared with the computation suggested by Kuhn and Sudhoff [15]:

$$t_{res} = \frac{2}{\omega_0} \tan^{-1}\left(\frac{C_r \omega_0 V_d}{i_{boost}}\right) \tag{34}$$

Once again, Figure 8 shows that the results were similar only at high dc voltages. The time required for the auxiliary current to decay to zero after the completion of the resonant phase ($t_5 + t_6 + t_7$) as specified in Equations (25), (26) and (28) was compared to the method used by Kuhn and Sudhoff [15]. Figure 8 also shows good agreement except at low dc voltages, as expected. The comparison shown in Figure 8 corresponds to ARCP transitions from the lower diode to the upper switch with positive load current. However, examination of other ARCP transitions yielded similar results to those of Figure 8.

ARCP Simulation

An ARCP circuit simulation was then used to compare computed timing characteristics to those obtained from the simulation. The simulation utilized a low bus voltage of 28V dc, C_r = 10,000 pf, L_r = 18 μH and a positive load current of 1A. The boost current was set to 1.5A. The result of a transition from the lower diode to the upper switch is shown in Figure 9.

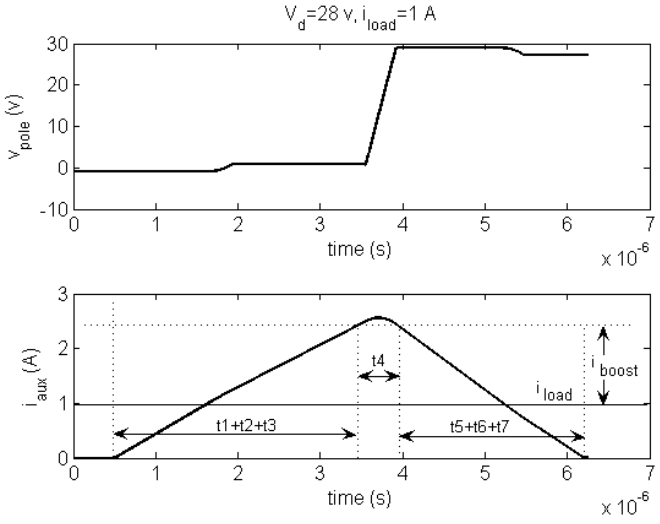

Figure 9. ARCP Simulation for Low DC Bus Voltage, 1A Load

A close examination of the circuit simulation shows that the time for the auxiliary current to reach the load-current level plus the boost current (as measured from the auxiliary pump switch turn-on) was 3.053 μsec. This compares quite favorably with the computed value from Equations (19), (20) and (22) of 3.076 μsec. However, the traditional calculation methodology yielded 2.678 μsec. Thus, if the traditional methodology were to be applied to this low-voltage ARCP with variable-timing control, the lower switch would be turned off before the required boost current is reached. This could result in loss of zero-voltage switching.

The circuit simulation showed a resonant time (t_4) of 0.379 μsec, compared to the computed time from Equation (23) of 0.3698 μsec. The traditional calculation method yielded a resonant time of 3.598 μsec. Finally, the total time for the ARCP commutation as measured from the turn-on of the auxiliary pump switch to the instant the auxiliary current decayed to zero was observed to be 5.699 μsec in the simulation. The computed value using Equations (19), (20), (22), (23), (25), (26) and (28) was 5.71 μsec, while the traditional computation yielded 5.64 μsec.

Conclusion

In this paper, the authors presented a variable-timing method for accurate soft-switching in an ARCP converter over a wide dc bus voltage range. It was shown through simulation that special attention is needed for accurate timing control of the ARCP when the dc bus voltage is low (where low is defined generally as the voltage level at which the switching device voltage drops play a significant role in the circuit). This proposed approach was verified through simulation to be accurate in determining appropriate gate switching times required to optimize performance of the ARCP. The switching times determined using the proposed approach were also compared to approaches where the device voltage drops were not considered to demonstrate the potential implications of low-voltage ARCP operations on variable timing.

References

[1] De Doncker, R. W., & Lyons, J.P. (1990). The Auxiliary Resonant Commutated Pole Converter. *IEEE Industry Applications Society Annual Meeting*, *2*, 1228-1235.

[2] Zhu, H., Lai, J., Hefner, A.R., Tang, Y., & Chen, C. (2001). Modeling-Based Examination of Conducted EMI Emissions from Hard and Soft-Switching PWM Inverters. *IEEE Transactions on Industry Applications, 37*(5), 1383-1393.

[3] Emami, Z., Farzanefard, H., & Motahari, S. R. (2010). EMI Evaluation in Hard Switching and Soft Switching PWM Flyback Converters. *Power Electronic & Drive Systems & Technologies Conference (PEDSTC)*, (pp. 46-51).

[4] Kim, H. J., Chung, Y. H., Lee, K. S., Jon, Y. S., & Kim, K. S. (2007). Performance Analysis of Soft-Switching Inverter for the Photovoltaic Power System. *7th International Conference on Power Electronics*. (pp. 436-439).

[5] Dong, W., Choi, J., Li, Y., Yu, H., Lai, J., Boroyevich, D. et al. (2000). Efficiency Considerations of Load Side Soft-Switching Inverters for Electric Vehicle Applications. *Applied Power Electronics Conference and Exposition, 2*, 1049-1055.

[6] Morii, H., Yamamoto, M., & Funabiki, S. (2009). Capacitor-Less Auxiliary Resonant Commutated Pole (ARCP) Voltage Source Soft Switching Inverter Suitable for EV. 13th *European Conference on Power Electronics and Applications,* (pp. 1-8).

[7] Chan, C. C., Chau, K. T., Chan, D. T. W., Yao, J., Lai, J., & Li, Y. (1998). Switching Characteristics and Efficiency Improvement with Auxiliary Resonant Snubber Based Soft-Switching Inverters. *Power Electronics Specialists Conference* '98, *1*, 429-435.

[8] Yu, Q., & Nelms, R. M. (2002). State Plane Analysis of an Auxiliary Resonant Commutated Pole Inverter and Implementation with Load Current Adaptive Fixed Timing Control. *IECON*, *1*, 437-443.

[10] Lai, J., Zhang, J., Yu, H., & Kouns, H. (2006). Source and Load Adaptive Design for a High-Power Soft-Switching Inverter. *IEEE Transactions on Power Electronics*, *21*(6), 1667-1675.

[11] Lai, J., Yu, W., & Park, S. (2009). Variable Timing Control for Wide Current Range Zero-Voltage Soft-Switching Inverters. *24th Annual IEEE Applied Power Electronics Conference and Expo*, (pp. 407-412).

[12] Ma, K., Xu, D., Zhang, T., & Igarashi, L. (2009). The Evaluation of Control Strategies for Auxiliary Resonant Commutated Pole Inverter. *IEEE Energy Conversion Congress and Exposition*, (pp. 810-816).

[13] Jiang, J., Zhou, X., & Zhang, W. (2000). An Improved Auxiliary Resonant Commutated Pole Inverter Using Assistant Power Source. *3rd International Power Electronics and Motion Control Conference*, *1*, 158-162.

[14] Walters, E. A., Pekarek, S. D., & Wasynczuk, O. (1997). Simulation of an ARCP-Based Field Oriented Induction Motor System. *Proceedings of the Naval Symposium on Electric Machines*, (pp. 85-90).

[15] Kuhn, B. T., & Sudhoff, S. D. (1997) Modeling Considerations in ARCP Versus Hard Switched Drives. *Proceedings of the 1997 Naval Symposium on Electric Machines*, (pp. 161-168).

[16] Teichmann, R., & Bernet, S., (1998). Investigation and Comparison of Auxiliary Resonant Commutated Pole Converter Topologies. *29th Annual IEEE Power Electronics Specialists Conference Record*, *1*, 15-23.

Biographies

TODD D. BATZEL received a BS in electrical engineering from Pennsylvania State University in 1984, an MS in electrical engineering from the University of Pittsburgh in 1989, and a PhD in electrical engineering in 2000 from Pennsylvania State University. He is currently an associate professor of electrical engineering at Penn State Altoona. His research interests include machine controls, electric drives, and artificial intelligence. Dr. Batzel may be reached at tdb120@psu.edu

KIPP ADAMS is currently a fourth-year student in the electro-mechanical engineering technology program at Penn State Altoona.

WAVE PROPAGATION IN METAMATERIAL USING MULTISCALE RESONATORS BY CREATING LOCAL ANISOTROPY

Riaz Ahmed, University of South Carolina; Sourav Banerjee, University of South Carolina

Abstract

Directional guiding, passing or stopping of elastic waves through engineered materials have many applications to the engineering fields. Recently, such engineered composite materials received great attention by the broader research community. In elastic waves, the longitudinal and transverse motion of material particles are coupled, which exhibits richer physics and demands greater attention than electromagnetic waves and acoustic waves in fluids. Waves in periodic media exhibit the property of Bragg scattering and create frequency band gaps in which the energy propagation is prohibited. However, in addition to the Bragg scattering, it has been found that local resonance of artificially designed resonators can also play a critical role in the generation of low-frequency band gaps. It has been found that negative effective mass density and negative effective elastic modulus are created by virtue of the local resonators and are correlated with the creation of the frequency band gaps that can be artificially perturbed.

In this paper, the authors present a novel anisotropic design of metamaterial using local split-ring resonators of multiple-length scales. Unlike traditional metamaterials, multiple split rings of different dimensions are embedded in a polymer matrix. Considering the complexity of the proposed material, it is extremely difficult to find the dynamic response of the material using analytical methods. Thus, a numerical simulation was performed in order to find frequency band gaps. Simultaneously, correlation between the band gaps and negative effective mass density and negative effective elastic modulus was verified. Both unidirectional split rings and bidirectional chiral split rings were studied. The effects of discontinuity in the rings at larger scales were compared with the dynamic characteristics of full rings in the proposed metamaterial. Application of such metamaterials will be primarily for vibration isolation and impact mitigation of structures. The proposed configuration is based on unit dimension and is, thus, dimensionless. The concept can be easily commutable between macro-scale structures for low-frequency applications and micro-scale MEMS devices for high-frequency applications.

Introduction

Sonic and ultrasonic wave propagation through periodic structures has been the subject of interest for many years. Recently, this topic received greater attention in solid-state physics and acoustics. Periodic media has a unique capability of being able to manipulate wave propagation by exhibiting innumerous possibilities, e.g., creating directional guiding, frequency filtration, negative dispersion and many other novel phenomena yet to be discovered. Such properties of the periodic media have triggered many new ideas of possible applications to different engineering fields. Periodic elastic structures are capable of producing frequency band gaps, where apparently no wave energy can be transmitted through the structures; however, energy is not actually lost but is in fact absorbed by the local resonators. A significant amount of research has been conducted in recent years on the manipulation of frequency band gaps in different frequency ranges through an innovative design of the acoustoelastic metamaterials.

Acoustoelastic metamaterials and a novel arrangement of phononic crystals are used for vibration control, impact mitigation and acoustic wave manipulation. Structures (e.g., civil, mechanical and aerospace) or individual structural components are vulnerable to external vibration, especially when the external vibration frequencies are at the proximity of the natural frequencies of the structures. The natural frequencies of a system are known during the design of the structural systems. Thus, if possible, the proposed metamaterials can be placed on the structures and the design of the metamaterials can be tuned in such a way that the external vibration frequencies close to the natural frequencies of the structure will be completely damped, keeping the structure safe. Other possible applications of metamaterials are evident in naval research. Metamaterials are capable of guiding and bending acoustic waves; for example, sonar radiated waves can be twisted and guided so that they will never be reflected back to the enemies. And while a perfect acoustic clock could be built, it is admittedly a rather farfetched futuristic application. These acoustoelastic metamaterials are classified into two broader categories. One set of metamaterials is made by changing the structural geometry by processes such as grooving, cutting, etc.; in other

words, perturbing the surface texture of the structures. On the other hand, metamaterials can also be made by designing novel inclusion patterns in the host matrix of the materials and considering them composite or engineered materials.

El-Bahrawy [1] and Banerjee et al. [2-4] studied wave propagation in periodic wave guides, where the surfaces of the elastic media (wave guides) were proposed to be perturbed sinusoidally without creating any inclusions inside the material (metamaterial of type 1). Thus, surface perturbations (surface etching) and volume perturbations (inclusions) are completely different genre of metamaterials. Here, the metamaterials with volume perturbation is discussed. Photonic researchers are also engaged in designing electromagnetic metamaterials [5-7] in the exploration of photonic band gaps, a range of frequencies where electromagnetic waves cannot propagate [8]. The same is true for the physical understanding of stress (elastic) wave propagation in phononic crystals and electromagnetic wave propagation in photonic crystals [9-11]. Thus, the concepts of designing newly engineered materials are commutable between electrodynamics and elastodynamics. As a rule of thumb, mass-in-mass systems are frequently proposed for elastodynamic problems to predicatively manipulate the frequency band gaps with engineered volume inclusion (metamaterials of type II). Applications of such acoustic metamaterials have been envisioned for acoustic cloaking, vibration control, sound isolation, etc. [12], [13].

Band-gap manipulation is very important in periodic structures in order to diversify their applicability. The formation of a negative bulk modulus and negative effective mass densities can result in band gaps in periodic structures [14-16]. Negative effective mass density arises from the negative momentum of the unit cell with a positive velocity field [17]. In mass-in-mass unit cells, the effective mass of the cell becomes negative at frequencies near the local resonance frequency, due to the special decay in wave amplitudes [18]. Hsu [19] showed that frequency band gaps can be formed by multiple scattering of the periodic inclusions, also known as Bragg scattering. Low-frequency sounds can be controlled by introducing locally resonant components into phononic crystals [20-22]. Generally speaking, a locally resonant medium consists of a heavy material core coated with softer material and then embedded into a host of other media. There are always multiple possibilities for opening new low-frequency forbidden gaps by setting an engineered local resonator in phononic crystals. Band gaps can be obtained or manipulated by altering the geometry of the local resonators [19].

Table 1. Material Properties

Material	Young's Modulus (GPa)	Density (kg/m^3)	Poisson's Ratio
Steel	205	7850	0.28
Epoxy	2.35	1110	0.38

Recently, researchers have attempted to open new portals of band gaps by artificially designing the metamaterial system. Huang et al. [14] proposed a multi-resonator system by introducing an additional mass in a previously proposed one -resonator mass-in-mass model [18]. Similarly a layer-in-layer system was proposed by Zhu et al. [23] to calculate the effective dynamic properties of the finite acoustic metamaterial. Low-frequency or high-frequency (high or low wavelengths, respectively) bands were already engineered by the proposed models. A model that can devise a wider band of frequency gaps (at both low- and high-frequency regions) is desired. If by any means higher numbers of closely spaced band gaps are obtained, they can eventually be merged by manipulation. Such multiple band gaps could potentially form a wider band gap. Such possibilities were not demonstrated by any previous models. In this study, then, a novel split-ring metamaterial was proposed. The proposed model not only obtains wider frequency bands but also multiple band gaps in both low- and high-frequency regions. The proposed unit cell is composed of a multiscale mass-in-mass system that forms a multiscale mass-in-mass model (MMM), which was proposed by any researchers. A two-dimensional study was performed and the full structure was considered infinite with periodic unit cells.

The concept of split rings was inspired by its counterpart from electromagnetic waves in photonics. Guenneau et al. [24] proposed a double 'C' resonator for wave focusing and confinement. Movchan et al. [25] used split-ring resonators to control electromagnetic bands in two-dimensional photonic structures. Many other photonic researchers found split rings useful in manipulating electromagnetic waves for specific purposes. To the best of authors' knowledge, split-ring resonators were introduced into the acoustic wave arena for the very first time in this study.

A few possible futuristic applications of the proposed metamaterials were mentioned in previous paragraphs. However, in the near term, this research will likely have a significant impact on the design of innovative microphones for directional sensitivity of sounds [26]. Speech recognition by reducing noise will improve the quality of synthesized sound for clean speech recognition in transformed domains [27]. Similar to the concept of Filtered-XRLS, an

algorithm with sequential updates [28] can be used to optimize the design of appropriate acoustic metamaterial filters, which will eventually help active acoustic noise control. In this paper, a step towards the engineering design of such a metamaterial is presented.

Numerical Implementation

A two-dimensional structure with a multiple-resonator system was proposed in this study. Figure 1a illustrates the schematic of the unit cells. One unit cell is composed of a steel core with a diameter of 0.1414" embedded in a circular ring with an outside diameter of 0.2828". A softer material (epoxy) was used to seal the space between the steel ball and the circular ring. A similar mass-in-mass system was proposed by Huang et al. [18].

In this paper, an additional set of semicircular rings was placed symmetrically in order to increase the number of band gaps. To generate access to the new portal in order to manipulate further frequency bands, another pair of elliptical split rings was positioned symmetrically but orthogonally to the previously positioned semicircular rings. All of the rings were made of steel with a thickness of 0.037" and included in a softer material. For simplicity, the steel cores, elastic coating and the split rings were considered embedded in an epoxy matrix. Material properties of the unit cell are listed in Table 1. Additional studies were performed in order to analyze the geometrical dependency of elliptical split rings compared to elliptical full rings (see Figure 1b).

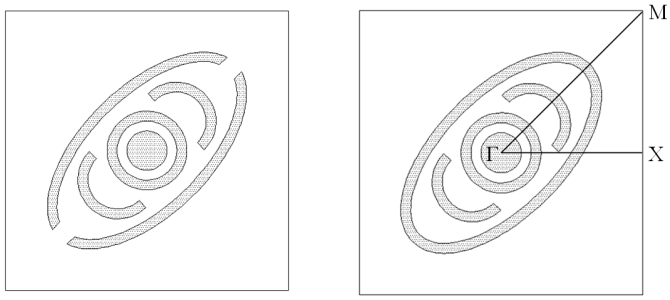

(a) Split Ellipse **(b) Full Ellipse**

Figure 1. Proposed Multiple Resonator Unit Cell

The proposed model was fairly complicated for performing analytical solutions for obtaining the dispersion curves. The eigenvalue analysis (dispersion) was performed using Finite Element simulation. The Floquet periodic boundary condition was enforced at all four boundaries of the unit cell. Floquet boundary conditions can be written as $(x + dx, y + dy) = F(x,y)$, where dx and dy are the period length of the periodic media along x and y directions, respectively. Floquet boundary conditions are based on the Floquet theory, which can be applied to the problem of small-amplitude vibrations of spatially periodic structures. A Bloch solution [29] for the frequency response to a small-amplitude time-periodic excitation that also possesses spatial periodicity can be sought in the form of the product of two functions. One follows the periodicity of the structure, while the other follows the periodicity of the excitation. The problem can be solved on a unit cell of periodicity by applying the corresponding periodicity conditions to each of the two components in the product. The Floquet periodicity conditions at the corresponding boundaries of the periodicity cell are expressed as

$$u_T = u_S e^{(ik.(x_t - x_s) - i\omega t)} \tag{1}$$

where $\boldsymbol{u}$ is the displacement vector and vector $\mathbf{k}$ represents the spatial periodicity of the excitation or the wave number. $\boldsymbol{T}$ stands for target and $\boldsymbol{S}$ stands for source element. $\mathbf{x_t - x_s}$ $\mathbf{k.\ x_t - x_s}$ calculates the distance between source and target and, thus, $\mathbf{k}$ provides the phase difference between them. The general linear relation between the stress and strain tensors in solid materials at x_m is expressed by Hook's law:

$$\sigma_{ij} = C_{ijkl}(x_m)\varepsilon_{kl} \tag{2}$$

Here, σ is the Cauchy's stress tensor, ε is the strain tensor and C_{ijkl} is a fourth-order elasticity tensor. For small deformations, the strain tensor is defined as

$$\varepsilon_{kl} = \frac{1}{2}\left(u_{k,l} + u_{l,k}\right) \tag{3}$$

where i, j, k and l take on the values of 1, 2 and 3; typical index notation applies. u_i represents particle displacement along i. The elastic wave equation is then expressed as

$$\frac{\rho(x_m)(\partial^2 u_i)}{\partial t^2} - \nabla \cdot (C_{ijkl}(x_m)\varepsilon_{kl} - s_i) = F_i \tag{4}$$

Here, $\rho(x_m)$ is the medium density, which is a function of space; $\boldsymbol{s}$ and $\boldsymbol{F}$ represent the source terms. If a time-harmonic wave is assumed, the displacement function can be written as

$$u(x, k, t) = u(x, k)e^{i\omega t} \tag{5}$$

where f represents the frequency and $\omega = 2\pi f$ is the angular frequency. Assuming the same time-harmonic dependency for the source terms $\boldsymbol{s_0}$ and $\boldsymbol{F}$, the wave equation for linear elastic waves reduces to an inhomogeneous equation:

$$-\omega^2 \rho(x_m)u_i - \nabla \cdot \left(C_{ijkl}(x_m)\varepsilon_{kl} - s_i\right) = F_i \tag{6}$$

Alternatively, eigenmodes and eigenfrequencies can be solved by treating this Helmholtz equation as an eigenvalue

partial differential equation. Eigenfrequency equations are derived by assuming a harmonic displacement field, similar to the frequency response formulation. The only difference is that the eigenfrequency study uses a new variable, $j\omega$, explicitly expressed in the eigenvalue $j\omega = -\lambda$. The eigenfrequency f is then derived from $j\omega$ as

$$f = \left|\frac{\mathrm{Im}(j\omega)}{2\pi}\right| \tag{7}$$

A dispersion relation was obtained by discretizing the wave number domain from zero to ka/π, where 'a' is the periodicity of the unit cell and '**k**' is the fundamental or incident wave number. Please note that, according to the Bloch-Floquet theorem, any solution of wave number $(\tilde{k})$ in periodic media can be written as

$$\tilde{k} = k + G \tag{8}$$

$$G = \frac{2\pi n}{a}\hat{x} + \frac{2\pi m}{b}\hat{y} \tag{9}$$

where n and m take on the values 1,2,3,…∞. a and b are the periodicity of the unit cell along the x and y directions, respectively. In this study, $a = b$. **G** is the reciprocal basis of the proposed periodic media.

Dispersion Relation and Geometric Dependency

The primary objective of this study was to obtain multiple band gaps at both low- and high-frequency regions. Frequencies up to 180 kHz were analyzed in this study. Frequencies less than 50 kHz were considered to be in the low-frequency region and 50–180 kHz frequencies were considered to be in the high-frequency region. Figure 2 shows the dispersion relation for the multi-resonant system proposed in Figure 1a. The total band structure was computed for the ΓXMΓ boundary (see Figure 1b). Three band gaps were observed in the low-frequency region from 20.83 to 22.07 kHz, 27.22 to 29.94 kHz and 36.72 to 37.47 kHz, with bandwidths of 1245 Hz, 2723 Hz and 743 Hz, respectively.

To understand the explanation of band-gap formation in gap frequencies, a frequency-domain analysis was performed. A uniformly distributed compressive load of magnitude 1 N (P in Figure 3a) was applied on both sides of the unit cell along the x direction. According to load-deformation laws, one can expect to observe compressive deformation in unit cells along the x direction. At an arbitrary frequency of 28.5 kHz (a frequency within the band gap 27.22 to 29.94 kHz) it was observed that the unit cell tends to elongate along the x direction. Such an unusual phenomenon signifies the formation of negative bulk modulus at frequencies where band gaps exist and verifies the established hypothesis on creation of resonant band gaps.

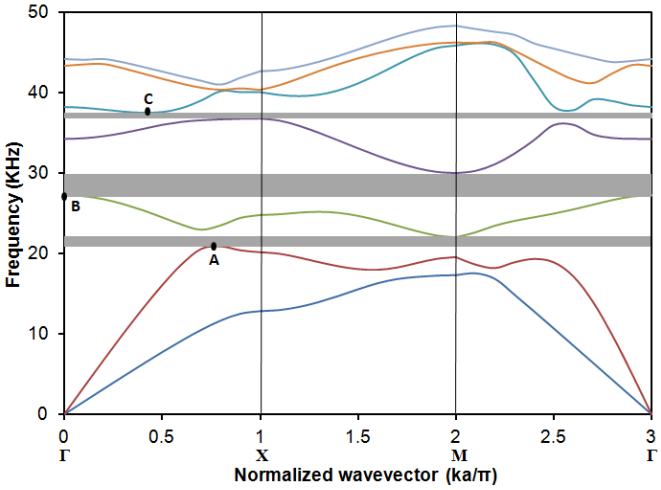

Figure 2. Dispersion Relation with Split Ellipse Resonator

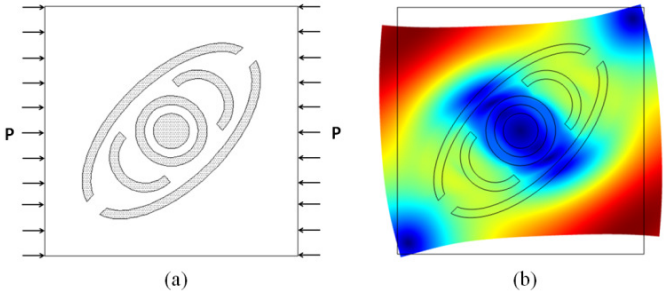

Figure 3. (a) Loading Setup in Unit Cell and (b) Displacement Mode at f = 28.5 kHz

Another objective of this study was to understand the geometric effect of elliptical resonators. Both the models with split rings (model 1) and full-ring resonators (model 2) were introduced in Figure 1. The full-ellipse resonator model also produced three band gaps from 20.59 to 22.7 kHz, 26.64 to 30.37 kHz and 37.17 to 37.9 kHz, with bandwidths of 2118 Hz, 3726 Hz and 729 Hz, respectively (see Figure 4). Both proposed models generated three low-frequency band gaps for the ΓXMΓ boundary. No high-frequency band gaps were observed. In model 2, each band gap was formed in more or less the same frequency ranges, compared to model 1. However, higher bandwidths were noticed for full-ellipse configurations for the first two band gaps, while the third band gap thickness was relatively unchanged in both models.

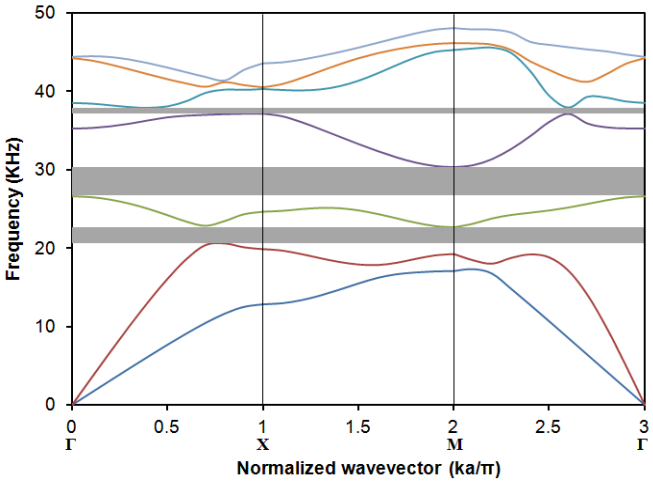

Figure 4. Dispersion Relation with Full Ellipse Resonator

Vibration in steel-core and steel resonators created the band modes in the first band gap. Steel-ball and closed steel rings were the dominating resonators in these bands and elliptical rings were vibrating with smaller amplitudes. Plate vibration was also coupled with these modes. In the second band gap, resonances at elliptical rings were more prominent than the first mode. Since elliptical rings are responsible for both first and second band mode resonances, a change in resonator geometry affected the bandwidth. Vibration modes at location A & B (see Figure 2) is shown in Figures 5a and 5b. A full ellipse can absorb more energy than a split resonator, which results in higher bandwidth at the second band gap in the full-ellipse model. In the third gap, very little vibration was observed in the elliptical rings (see Figure 5c), which signifies almost the same bandwidth for both models.

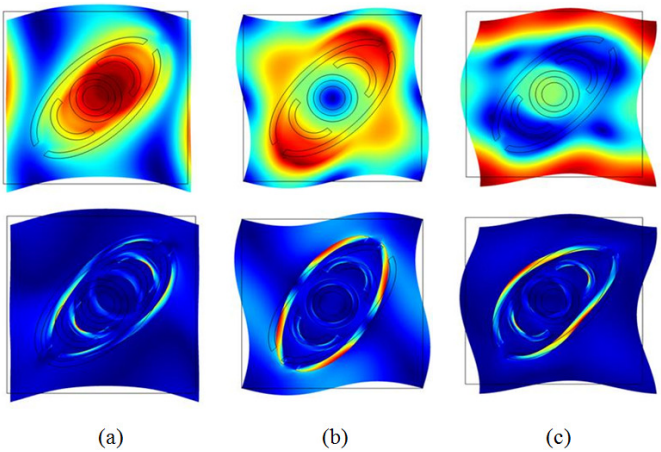

Figure 5. Displacement (top) and Von Mises Stress (bottom) Mode at (a) A, (b) B and (c) C Positions (see also Figure 2)

Band gaps over the full frequency range (0-180 kHz) for the ΓXMΓ boundary and their dependency on elliptical resonators are reported in Figures 2, 4 and 5. The geometric influence of elliptical resonators in the Γ-X, X-M and M-Γ directions were also explored individually.

A comparative study was conducted and the band structures obtained from the models are presented in Figures 6, 7 and 8. A remarkable number of band gaps, more than 20, were achieved in both the Γ-X and X-M directions for each model. In this paper, bandwidths higher than 700 Hz are reported. In the figures shown in this paper, the y axis represents the location of the band gaps along the frequency axis and the x axis represents the frequency bandwidth of the band gaps. Larger band gaps were observed at low frequencies in all directions. In the low-frequency region, frequency bands were generated very close to each other. Larger band modes were mostly dependent on elliptical ring resonators. Thus, geometric alteration will help to manipulate the band structure. It was also observed that the local resonances were a function of the incident wave direction.

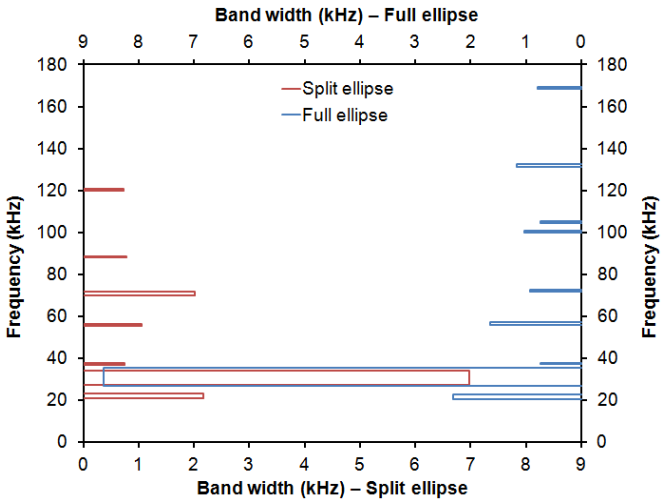

Figure 6. Band-Gap Comparison for Split and Full Ellipse Resonator in Γ-X Direction

At higher frequencies, significant numbers of smaller band gaps were observed (in both the Γ-X and X-M directions). These band gaps were strongly influenced by the cell geometry. Different frequency ranges were more pronounced for different geometries. Epoxy modes were mainly dominant in the high-frequency regions. Low-amplitude vibrations of elliptical and half-circular resonators were also coupled with those modes. Since epoxy modes were dominant at higher frequencies, little scattering can be achieved, which is another reason to get smaller band gaps. Using this understanding, a new orientation was proposed to expand

the first band gap at the lower frequencies. The proposed configuration is shown in Figure 9.

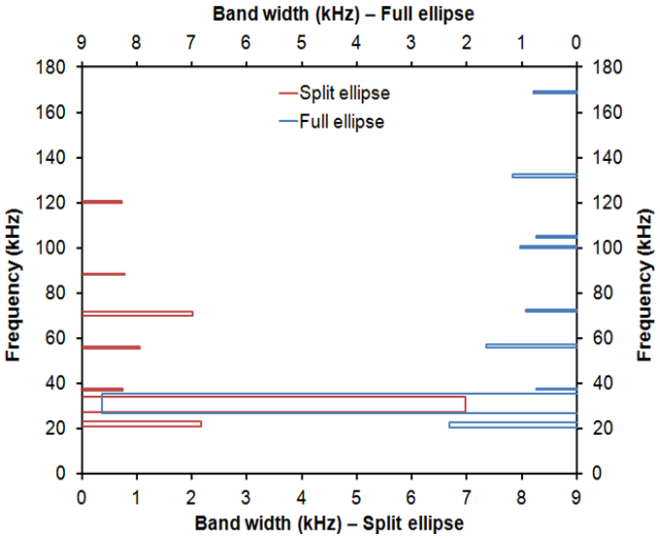

Figure 7. Band-Gap Comparison for Split and Full Ellipse Resonator in X-M Direction

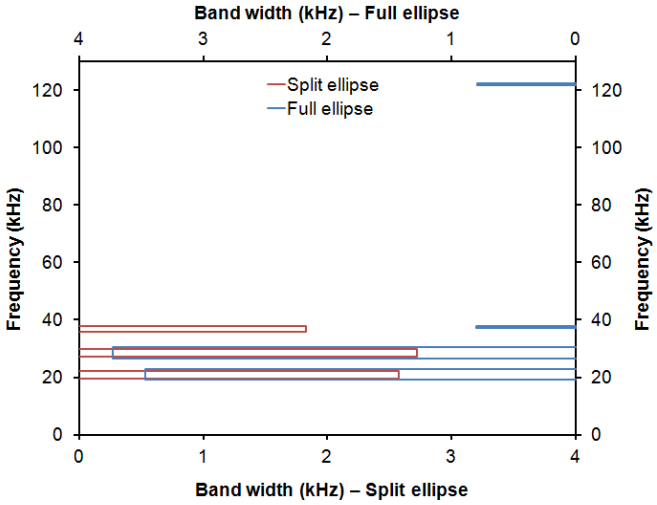

Figure 8. Band-Gap Comparison for Split and Full Ellipse Resonator in M-Γ Direction

A similar eigenvalue analysis of the system was performed and the dispersion relation between frequency and wave number for the proposed 2D mirror image pattern is shown in Figures 10 and 11. Figures 10 and 11 show the dispersion curves in the Γ-X, X-M and M-Γ directions for both the split-ellipse and the full-ellipse configurations, respectively.

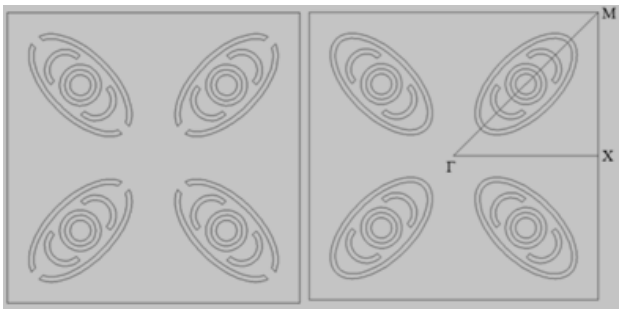

Figure 9. Proposed Multiple Diagonally Symmetric Resonator Unit Cell with Split-Ring Ellipse (left) and Full-Ring Ellipse (right)

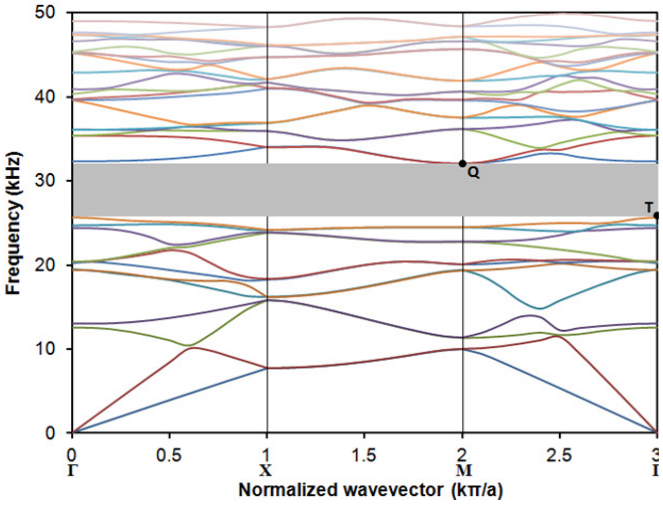

Figure 10. Dispersion Relation for the Split Ellipse Resonators

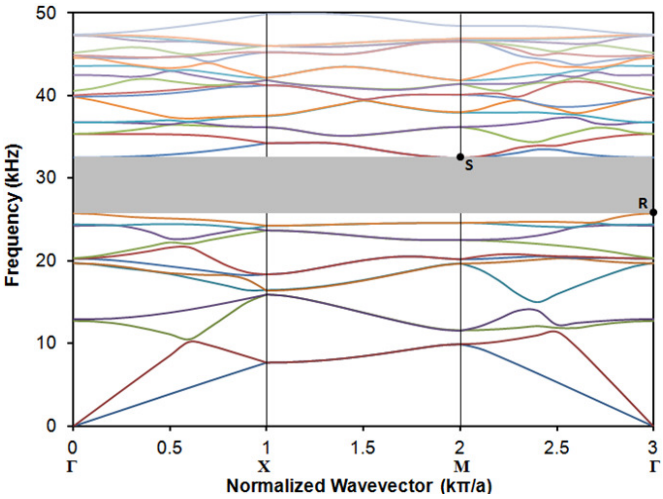

Figure 11. Dispersion Relation for the Full Ellipse Resonators

The dispersion relations show the existence of absolute band gaps below 50 kHz. These band gaps are essentially wider (between 24 kHz and 33 kHz) than the band gaps obtained in Figures 2 and 3. Figure 12 shows the displacement and Von Mises stress pattern for the modes T and Q (see Figure 10). Figure 13 shows the complete band structure of the diagonally symmetric pattern between 0–180 kHz along the X-M direction. It clearly shows that the number of band gaps is improved by the split-ring configuration if organized in a diagonally symmetric (mirror image) pattern of the unit cells, which was originally proposed in Figure 1 over a full-ring configuration.

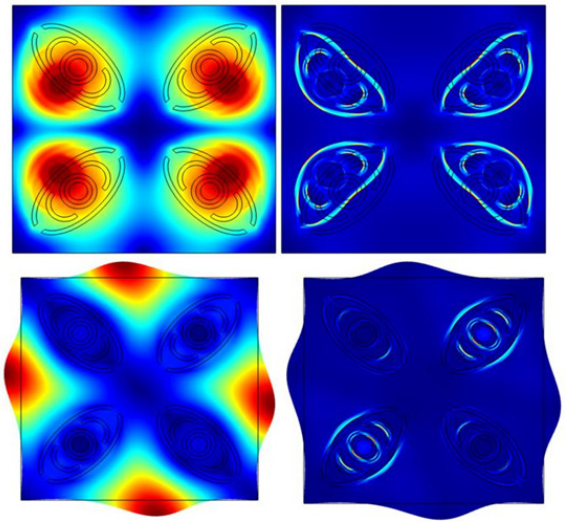

Figure 12. Displacement (left column) and Von Mises Stress (right column) for Mode T (top rows) and Mode Q (bottom rows)

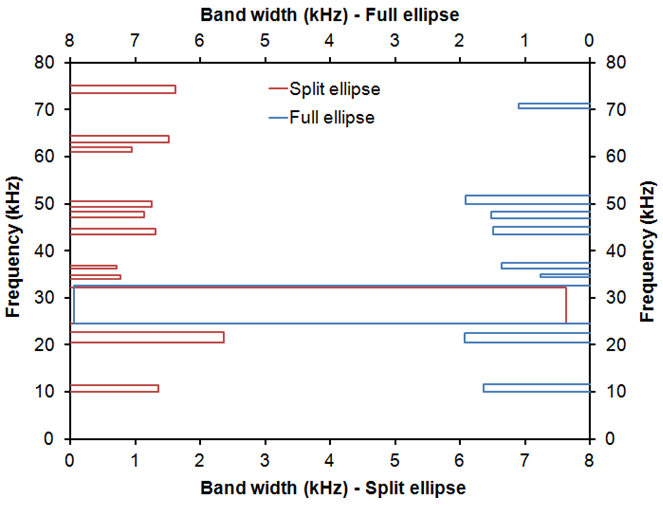

Figure 13. Band-Gap Comparison for Split and Full Ellipse Resonators in Diagonally Symmetric Configuration in X-M Direction

Acknowledgement

This research study was partially funded by the Office of the Vice President of Research and Department of Mechanical Engineering at the University of South Carolina.

Conclusion

Obtaining multiple band gaps by designing a novel configuration of metamaterials is one of the key areas of interest in recent days. Mass-in-mass and layer-in-layer models were proposed by previous researchers for finding multiple band gaps. But the number of band gaps was not significantly increased by these models. In this current study, a novel multi-scale mass-in-mass (MMM) system containing split-ring resonators for achieving several band gaps in both low- and high-frequency regions was proposed. Split-ring resonators are frequently used for guiding electromagnetic waves; however, it was initiated in order to implement this idea for guiding the acoustic waves for the first time. Three distinct band gaps were obtained (ΓXYΓ boundary) from the proposed model. However, multiple and wider band gaps were achieved for wave propagation along the direction other than the orthogonal directions. Wider band gaps were visible in the low-frequency region, while other smaller band gaps were noticed in the high-frequency region. It was also found that the frequency bands were influenced by the geometry of the elliptical resonators. Band position and width can be manipulated with the change of resonator geometry. A diagonally symmetric orientation of the unit cell was able to drastically improve the extent of the band gaps. This study can be useful to isolate or guide different directional wave and control the vibration over a wide range of frequencies, which can be a useful note for structural health monitoring.

References

[1] El-Bahrawy, A. (1994a). Stopbands and Passbands for symmetric Rayleigh-Lamb modes in a plate with corrugated surfaces. *Journal of Sound and Vibration 170*(2), 145-160.

[2] Banerjee, S., & Kundu, T. (2006). Elastic Wave Propagation in Sinusoidally Corrugated Wave Guides. *Journal of Acoustical Society of America*, *119*(4), 2006-2017.

[3] Banerjee, S., & Kundu, T. (2006). Symmetric and Anti-symmetric Rayleigh-Lamb modes in Sinusoidally corrugated waveguides: An Analytical approach. *International Journal of Solids and Structures*, *43*, 6551-6567.

[4] Banerjee, S., & Kundu, T. (2008). Elastic Wave Field Computation in Multilayered Non-Planar Solid Structures: A Mesh-free Semi-Analytical Approach, *Journal of Acoustical Society of America*, *123*(3), 1371-1382.

[5] Veselago, V. G. (1968). The Electrodynamics of Substances With Simultaneously Negative Values of ε and μ. *Soviet Physics Uspekhi, 10*, 509–514.

[6] Smith, D. R., Pendry, J. B., & Wiltshire, M. C. K. (2004). Metamaterials and Negative Refractive Index. *Science*, *305*, 788–792.

[7] Pendry, J. B., Holden, A. J., Robbins, D. J., & Stewart, W. J. (1999). Magnetism From Conductors and Enhanced Nonlinear Phenomena. *IEEE Transactions on Microwave Theory Tech., 47*, 2075–2084.

[8] Smirnova, E. I., Mastovsky, I., Shapiro, M. A., Temkin, R. J., Earley, L. M., & Edwards, R. L. (2005). Fabrication and Cold Test of Photonic Band Gap Resonators and Accelerator Structures. *Physical Review Special Topic Accelerator & Beams*, *8*, 091302.

[9] Liu, Z., Chan, C. T., & Sheng, P. (2005). Analytic Model of Phononic Crystals With Local Resonances. *Physical Review B*, *71*, 014103.

[10] Mei, J., Liu, Z., Wen, W., & Sheng, P. (2006). Effective Mass Density of Fluid-Solid Composites. *Physical Review Letters*, *96*, 024301.

[11] Wu, Y., Lai, Y., & Zhang, Z. (2007). Effective Medium Theory for Elastic Metamaterials in Two Dimensions. *Physical Review B*, *76*, 205313.

[12] Sigalas, M. M., & Economou, E. N. (1992). Elastic and Acoustic Wave Band Structure. *Journal of Sound and Vibration*, *158*, 377–382.

[13] Poulton, C. G., Movchan, A. B., McPhedran, R. C., Nicorovici, N. A., & Antipov, Y. A. (2000). Eigenvalue Problems for Doubly Periodic Elastic Structures and Phononic Band Gaps. *Proceedings of Royal Society London, A*, 456, 2543–2559.

[14] Huang, G. L., & Su C. T. (2010). Band Gaps in a Multiresonator Acoustic Metamaterial. *Journal of Vibration and Acoustics*, *132*(3), 031003.

[15] Li, J., & Chan, C. T. (2004). Double-Negative Acoustic Metamaterial. *Physical Review E, 70*, 055602.

[16] Milton, G. W., & Willis, J. R. (2007). On Modifications of Newton's Second Law and Linear Continuum Elastodynamics. *Proceedings of Royal Society London A*, 463, 855–880.

[17] Yao, S. S., Zhou, X. M., & Hu, G. K. (2008). Experimental Study on Negative Effective Mass in a 1D Mass-Spring System. *New Journal of Physics*, *10*, 043020.

[18] Huang, H. H., Sun, C. T., & Huang, G. L. (2009). On the Negative Effective Mass Density in Acoustic Metamaterials. *International Journal of Engineering Sciences*, *47*, 610–617.

[19] Hsu, J. C. (2011). Local resonances-induced low-frequency band gaps in two-dimensional phononic crystal slabs with periodic stepped resonators. *Journal of Physics D: Applied Physics*, *44*, 055401.

[20] Liu, Z., Zhang, X., Mao, Y., Zhu, Y. Y., Yang, Z., Chan, C. T., et al. (2000). Locally resonant sonic materials. *Science, 289*, 1734.

[21] Goffaux, C., S´anchez-Dehesa, J., Levy Yeyati A., Lambin, Ph., Khelif, A., Vasseur, J. O., et al. (2002). Evidence of Fano-like interference phenomena in locally resonant materials. *Physical Review Letters*, *88*, 225502.

[22] Hsu, J. C., & Wu, T. T. (2007). Lamb waves in binary locally resonant phononic plates with two dimensional lattices. *Applied Physics Letters*, *90*, 201904.

[23] Zhu, R., Huang, G. L., Hu, & G. K. (2012). Effective dynamics properties and multi-resonant design of acoustic metamaterials. *Journal of Vibration and Acoustics*, *134*, 031006-1.

[24] Guenneau, S., Movchan, A., Pétursson, G., & Ramakrishna, S. A. (2007). Acoustic metamaterials for sound focusing and confinement. *New Journal of Physics*, *9*, 399.

[25] Movchan, A. B., & Guenneau, S. (2004). Split-ring resonators and localized modes. *Physical Review B*, *70*, 125116

[26] Varada, V., Wang, H., & Devabhaktuni, V. (2010). Sound source localization employing polar directivity patterns of bidirectional microphones. *International Journal of Modern Engineering*, *11*(1), 35-44.

[27] Ngo, H., & Mehrubeoglu, M. (2010). Effect of the number of LPC coefficients on the quality of synthesized sounds. *International Journal of Engineering Research and Innovation*, *2*(2), 11-16.

[28] Tan, Li., & Jiang, J. (2009). Active noise control using the filtered-XRLS algorithm with sequential updates. *International Journal of Modern Engineering*, *9*(2), 29-34.

[29] Brillouin, L. (1953). *Wave Propagation in periodic structures*. Dover Publications, Inc.

Biographies

RIAZ AHMED is a Graduate Student in the Mechanical Engineering Department of the University of South Carolina. He received his MS degree from University of South Carolina, USA and BS degree in Mechanical Engineering from Khulna University of Engineering and Technology, Bangladesh. His area of research is related to theoretical and computational modeling of acoustics/ultrasonic waves in

periodic media and novel design of acoustoelastic metamaterials.

SOURAV BANERJEE is an Assistant professor of Mechanical Engineering at The University of South Carolina. He earned his B.S. degree (2000) from Bengal Engineering College, West Bengal, India in Civil Engineering. He received his M.Tech with specialization in Structural Engineering from Indian Institute of Technology, Bombay, India in 2002 and he received his Ph.D. (Engineering Mechanics, 2005) from the University of Arizona, Tucson, AZ. Dr. Banerjee is currently teaching at the University of South Carolina. His research area is related to theoretical and computational modeling of ultrasonic waves and phonons in homogeneous and heterogeneous media (e.g. metal, composites, functionally graded materials etc.). He has published 22 peer reviewed research papers and about 40 papers in conference proceedings. He has earner numerous awards and recognitions in the field of Structural Health Monitoring, e.g. prestigious 'Achenbach Medal' in the year 2010 is one of them. Dr. Banerjee may be reached at banerjes@cec.sc.edu.

DYNAMIC INTELLIGENT MEAN FILTER FOR IMPULSE NOISE SUPPRESSION IN 2D IMAGES

Benjamin Asubam Weyori, Nkrumah University of Science and Technology (GHANA);
Kwame Osei Boateng, Kwame Nkrumah University of Science and Technology (GHANA)

Abstract

Noise, as random, unwanted data, appears in images from various sources. So its reduction or removal is an important task in image processing. This study employed an intelligent mean filter, which is an extension of the median filter, adaptive median filter, and the mean filter, to achieve the purpose of noise reduction. The proposed mean filter belongs to the broad class of nonlinear filters. The method is more effective in image processing because it utilizes an intelligent technique to find the mean of a set of pixels in the active window, which is used to perform the filtering process. Impulsive noise is a form of image corruption where each pixel value is replaced with an extremely large or small value that is not related to the surrounding pixel values by a significant probability.

Any pixel that is noisy is replaced with the computed mean. The adaptiveness of the method lies in the size of the filtering window, which is determined by the amount of noise in the window. The filtering process starts with a 3x3 window and extends it to a 5x5 window until it gets to the maximum window size chosen by this technique, which is 9x9. The window size extends from the initial size to the subsequent sizes if the amount of noise pollution in each chosen size is greater than 40% using some approximation schemes. The moving-window architecture is employed to the movement of the window through the entire image in order to aid the filtering process. The performance of the proposed intelligent Mean filter has been evaluated in MATLAB simulations on an image that was subjected to various degrees of corruption with impulse noise. The results demonstrated the effectiveness of the algorithm.

Introduction

The transfer medium, the working conditions and the recording devices of an imaging system are subjected to noise corruption during transmission. Thus, the image quality is reduced and the effectiveness and accuracy of the subsequent processing course, such as edge detection, image segmentation, and pattern segmentation, can be negatively affected. Therefore, it is helpful to remove the noise from the image using an image filter. But the effective removal of the noise is often accomplished at the expense of blurred or even lost features [1].

Noise filtering is an important component in signal processing systems, which is comprised of estimating the amount of the signal that has been degraded by noise. The percentage of noise corruption is calculated by taking the percentage of the degraded pixels in the entire image. Intuitively, when the percentage of the polluted pixel is greater than the percentage of the clean uncorrupted pixel, most of the proposed filtering techniques generate a fairly poor result. The design of a filter will depend on the detection of the type of noise, estimation of the intensity of the noise corruption and the distribution of the noise [2], [3]. Digital image filtering techniques can be categorized into two broad areas: spatial domain filtering and frequency domain filtering. The spatial domain filtering technique is based on the direct manipulation of the image pixels, while the frequency domain filtering technique has to do with modifying the Fourier transform of the image [3].

Various spatial filtering techniques have been proposed for removing impulse noise in the past, and it is well known that linear filters can produce serious image blurring. As a result, nonlinear filters have been widely exploited due to their much improved filtering performance, particularly in relation to impulse noise attenuation and detail preservation. One of the most popular and robust nonlinear filters is the standard median (SM) filter [4], which exploits the rank-order information of pixel intensities within a filtering window and replaces the center pixel with the median value. The SM filter's effectiveness in noise suppression and simplicity of implementation has led to various modifications, such as the weighted median (WM) filter [5] and the center weighted median (CWM) filter [6].

The median filter is implemented by replacing all of the pixels in the activate window with the selected center pixel known as the median. The process replaces the corrupted and also the uncorrupted pixels in the image; the replaced uncorrupted pixels cause a lot of defeat in the image quality. Hence, a tentative solution for circumventing this problem is to implement a noise (impulse noise) detection technique to aid in the filtering process; this identifies only the corrupted pixels that will be replaced, while the uncorrupted pixels remain intact. The switching median filter [1], [7-9]

has achieved a lot of significant performance due to the noise detection mechanism that solves the problem of identifying the corrupted pixels in a filtering process.

The most popular approaches for dealing with such impulse noise have centered on median filtering and the rich class of order statistic filters that have emerged from the study of median filters [10], [11]. Recently, variations on the median filtering scheme have been shown, under specific signal/noise models, to deliver improved performance relative to the corresponding traditional methods. To solve the problem of filtering out edge details and image details causing blurring of the image, an intelligent mean filtering scheme is presented in this paper. It exhibits improved performance in removing impulse noise, while preserving the fine details of the 2D image structure.

Impulse (salt-and-pepper) Noise

Impulse noise is a sort of unidirectional impulse-like noise. This category of noise is usually occurs as a result of electromagnetic interference, analog-to-digital converter error, bit error in transmission, malfunctioning pixels in camera sensors or faulty memory locations [8], [11], [12]. Intuitively, when an image is polluted with this kind of noise, it sets some of the pixel values of the region with lower values to the maximum value and also converts some of the pixel values to the minimum value or zero.

Hence, an image that has been corrupted with impulse noise (salt and pepper) appears as bright spots in the dark region and dark spots in the bright region of the image. The uncorrupted pixels remain intact in the image. The percentage of the noise present in the image is calculated by the difference of the total percentage and the percentage of uncorrupted pixels. This can be quantified by finding the percentage of the corrupted pixels. The probability density function of impulse noise is given by:

$$p(z) = \begin{cases} P_a & for \quad z = a \\ P_b & for \quad z = b \\ 0 & otherwise \end{cases} \qquad (1)$$

The probability density function describes the distribution of the impulse noise particles in the image, where a and b are the pixel values in the image. When a happens to be far less than b and most of the image pixels lie in the range around the value of a, then b becomes a distortion with a high intensity appearing as a bright dot or bright spot in that region. Otherwise, when the pixel values lie in the range of b, then a instead becomes the distortion with a lower intensity and appears as a dark dot or dark spot.

If P_a or P_b is zero, then only one kind of situation can occur; that is, whether the spots that appear are either bright or dark in the entire image, which is termed unipolar noise. If neither of the probabilities are zero and both of the dark spots and the white spots are randomly distributed in the entire image, and if the frequency of appearance is approximately equal, then the noise is described as salt-and-pepper impulse noise.

Bipolar impulse noise occurs when an image contains extremely low values in a region where the pixel values are of high intensity and extremely high values in the region where the values are of low intensity. The salt-and-pepper impulse noise and the spots and spikes impulse noise belong to this category of noise, where the values of a and b are referred to as saturated values in the sense that they produce extremely pure white or extremely pure black, corresponding to the minimum and maximum values allowed. Positive (high pixel values) impulses appear white (salt) noise, while the zero impulses appear as black (pepper). For an 8-bit image this means that a = 0 (black) and b = 255 (white) [2], [3].

Mean Filter

Mean filtering is a linear filtering method for image smoothing. Its implementation is, as its name implies, intuitive and easy, i.e., it can reduce the amount of intensity variation between one pixel and the neighboring ones. The mean filter is the simplest type of low-pass filter because all of the coefficients of the mean filter have identical values. An example of a mean filter is shown in Figures 1 and 2. The idea is simply to replace each pixel value in an image with the mean value of its neighbors, including itself. The main purpose of doing this is to eliminate pixels which are unrepresentative of their surroundings [13], [14].

1/9	1/9	1/9
1/9	1/9	1/9
1/9	1/9	1/9

Figure 1. 3x3 Mean Filter/Kernel

Three factors can affect the characteristics of the filter (mask/kernel): width, height and shape of the filter. For example, the larger the size of the kernel, the more severe

would be the smoothing result. Therefore, there is always a compromise between the reduction of noise and the blurring effects associated with the selection of filter size and type. A better filtering technique is needed for areas in an image that have fine details and edges so that these details are not lost in the filtering process [2]. Figure 2 shows an example of the standard mean filter and how the mean is computed to form the window pixels that replace the center pixel.

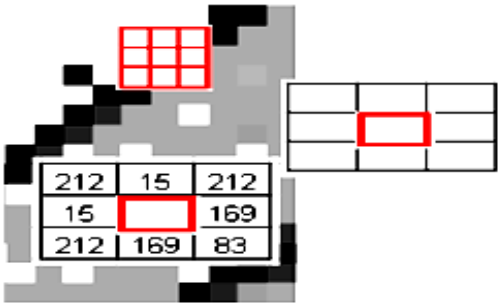

$$Mean = (212 + 15 + 212 + 15 + 15 + 169 + 83) / 9 = 122$$

Figure 2. Example of Mean Filtering

Proposed Intelligent Mean Filter

The intelligent mean filter algorithm is an ordered statistical non-linear filter which combines the techniques of the traditional median filter and mean filter in order to achieve a better result. The median filter ranks the pixel values using the ascending order or descending order and picks the middle value or the median, which is applied by replacing the median or middle values with the center values in the activate region. However, no detection mechanism is used to test and verify whether or not the center value in the region is polluted.

In this proposed filter algorithm, an initial window is chosen as 2n+1, and then the pixel values in the window are arranged using some specified criteria. The pixel value before the median value, the median value and the pixel value after the median value are chosen, including the minimum and maximum values. The pixel value before the median value and the value after the median value are tested to find out if they are polluted or not. The test is conducted by comparing them to the minimum and maximum values. If the condition of the value before the median is equal to the minimum value, then the window size is increased. On the other hand, if the value after the median is equal to the maximum value, then the window size is increased, meaning that there is a very high likelihood of impulse noise being present in the window. Hence, the size of the window is increased in order to bring in more pixels that may not be polluted to aid in the filtering process. After the window size is increased, the entire process is carried out again. If the same situation occurs, or the same conditions are met, the window size is increased again until it reaches the maximum window size. If the two conditions are not met, then the two values appear to be noiseless pixel values, hence the intelligent mean is computed. This is done by adding the median value and the two values before the median and after the median and dividing it by the number of values.

The computation of the intelligent mean is quite complex and takes time. After this process, the difference between the individual pixel values and the intelligent mean is computed. These differences are compared to a threshold value. If the difference is less than the threshold value, then the pixel value associated with this is replaced by the intelligent mean. This process continues until all of the affected values are successfully replaced. Finally, the maximum value is also replaced by K if it is equal to 255 for an 8-bit image; it is, however, different for an image with a higher bit count.

The neighborhood pixel properties are carefully employed in choosing the window size, and the relationship involved is used to arrive at a useful algorithm. The moving-window architecture technique shown in Figure 3 is adapted from the adaptive median filtering technique to help in the implementation of this algorithm. This is a systematic technique that moves throughout the entire image from point to point and helps the filtering process to work in every window.

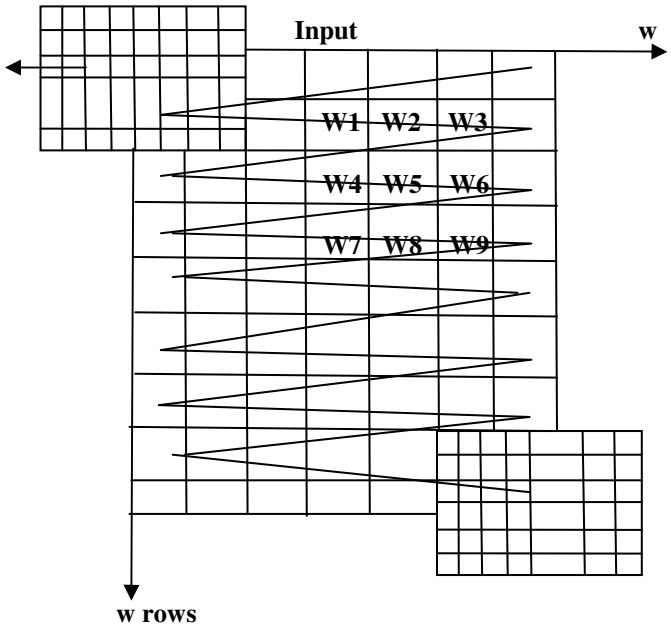

Figure 3. Moving-Window Architecture

For finding the arithmetic mean of a discrete set of numbers, a formula is applied, which is the same for finding the intelligent mean. If n numbers are picked, each distinct number is denoted by a_i, where $i = 1,\ldots,n$.

$$Mean = \frac{1}{n}\sum_{i=1}^{n} a_i \qquad (2)$$

Implementation and Testing of the Algorithm

K = median position in the sorted list
X_{med} = median of gray level value in $S_{x,y}$
X_{min} = minimum gray level value in $S_{x,y}$
X_{max} = maximum gray level value in $S_{x,y}$
X_{k-1} = value directly adjacent to the left of the median value
X_{k+1} = value directly adjacent to the right of the median value
$S_{x,y}$ = size of the window
D = largest interval between the sorted values starting for n=2 to n=n-1
K1 = pixel corrupted by impulse noise (salt noise) i.e., K1 = 0.
K2 = pixel corrupted by impulse noise (pepper noise) i.e., K2 = 255 for an 8-bit image

The modified median filtering algorithm works at three different levels, denoted as level A, B and C, as follows:

Level A:
$A1 = X_{k-1} - X_{min}$
$A2 = X_{k+1} - X_{max}$
If A1 > 0 and A2 < 0 Goto level B Else increase the window size.

Level B:

$$X_{maen} = \frac{X_{k-1} + X_{med} + X_{k=1}}{n}$$

$$B1 = \left| X_{i,j} - X_{mean} \right| < threshold$$

$$B2 = X_{\max} - 255$$

If B1 is true then replace $X_{i,j}$ with X_{mean} and proceed
If B2=0 the replace X_{max} with X_{max} — threshold

Figure 4 illustrates how the value to the immediate left of the median and the value to the immediate right of the median (when the values are arranged in ascending order horizontally) are tested for the presence of impulse noise. Figure 5 illustrates how the intelligent mean is computed and how the detected pixels that are corrupted with impulse noise are replaced with the intelligent mean.

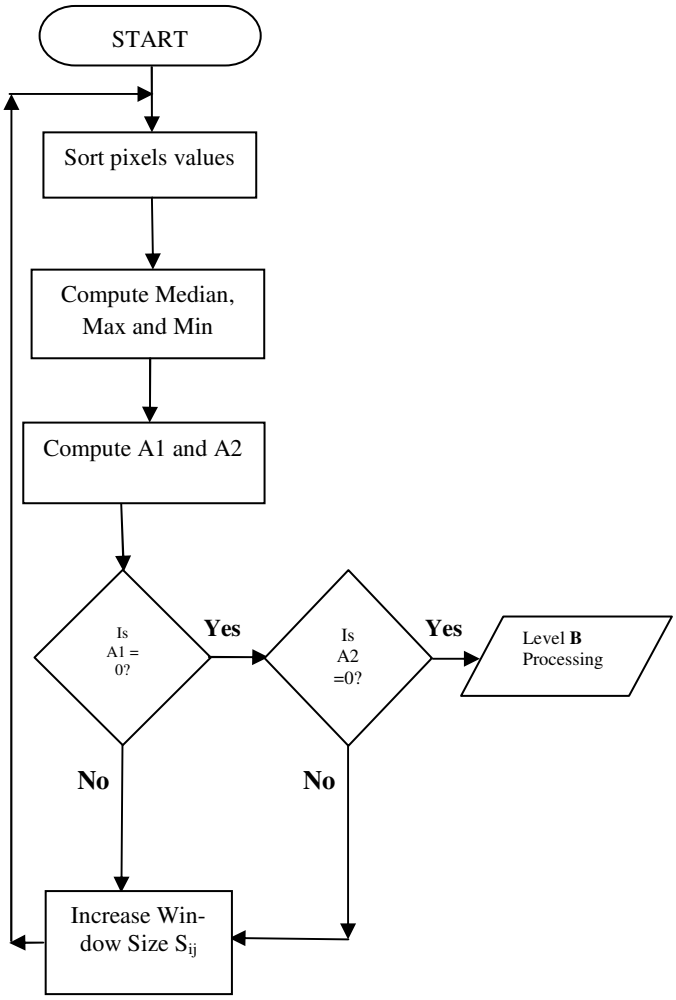

Figure 4. Flowchart Showing the Steps for the Detection of the Presence of Impulse Noise in the Active Window

Experimental Results

In order to test the performance rate of the proposed algorithm, experiments were performed at different noise levels. Intensive simulations were carried out on several images corrupted with impulse noise and Gaussian noise. The results showed that the modified efficient median filter achieved better results when applied to images corrupted by impulse noise (salt and pepper) than the results obtained from the image corrupted by Gaussian noise. The performance evaluation of the filtering operation was demonstrated by the output of the following images. The modified median filtering algorithm was implemented using MATLAB 7.40(R2007a), applied to a 3x3 window.

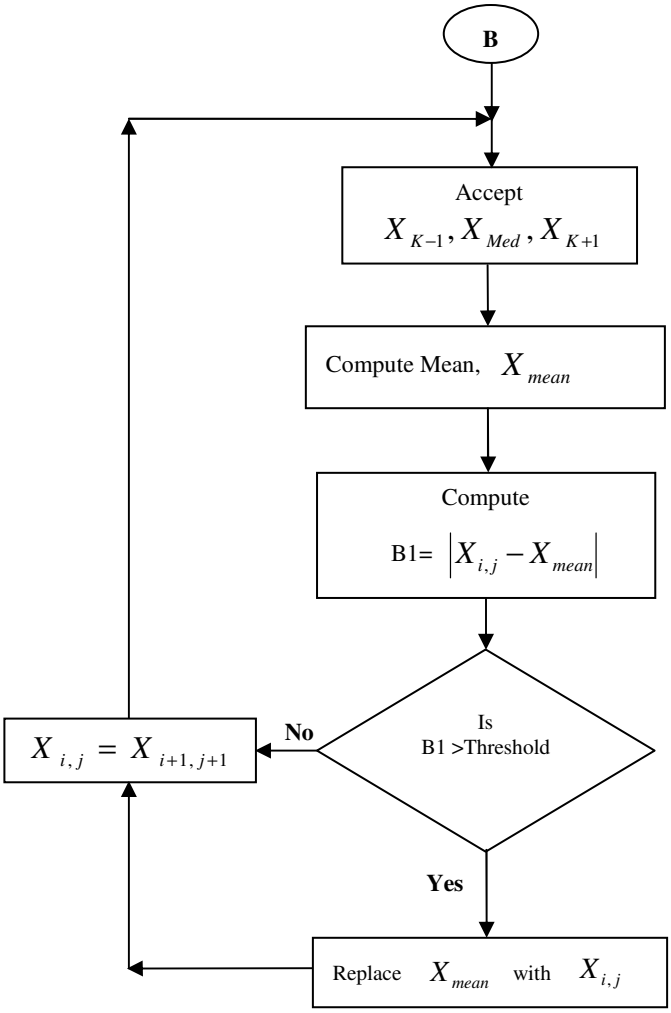

Figure 5. Flowchart Showing the Computational Steps of the Intelligent Mean Filter

Figure 6. Original Image of the Moon

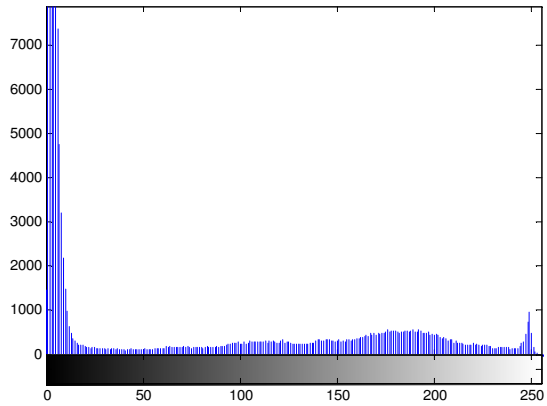

Figure 7. Histogram of the Original Image

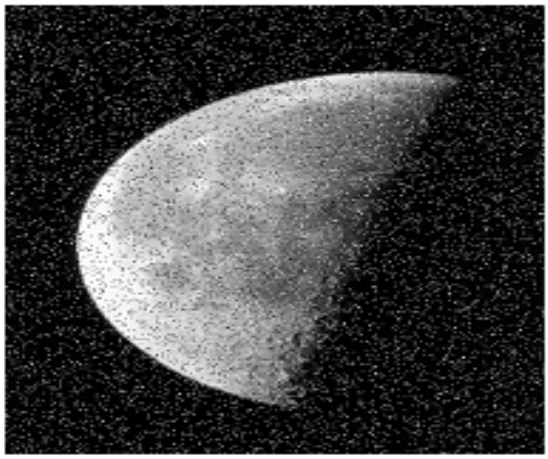

Figure 8. Image Polluted with 10% Impulse Noise

Figure 9. Filtered Image Using Intelligent Mean Filter

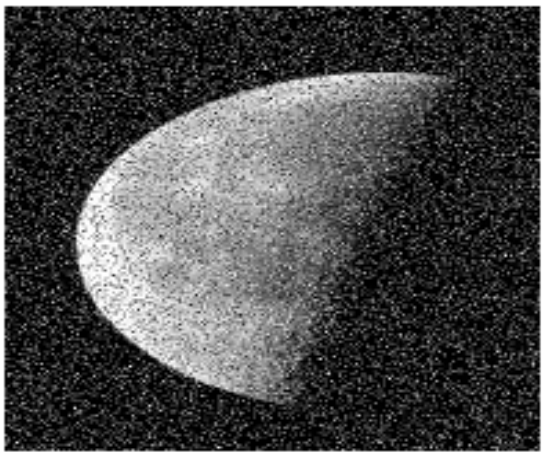

Figure 10. Image Polluted with 20% Impulse Noise

Figure 11. Filtered Image Using Intelligent Mean Filter

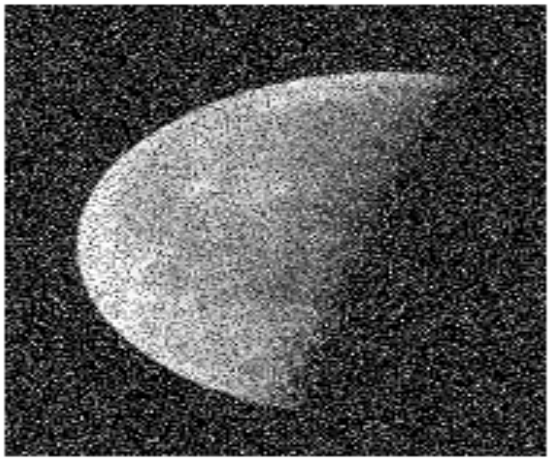

Figure 12. Image Polluted with 30% Impulse Noise

Figure 13. Filtered Image Using Intelligent Mean Filter

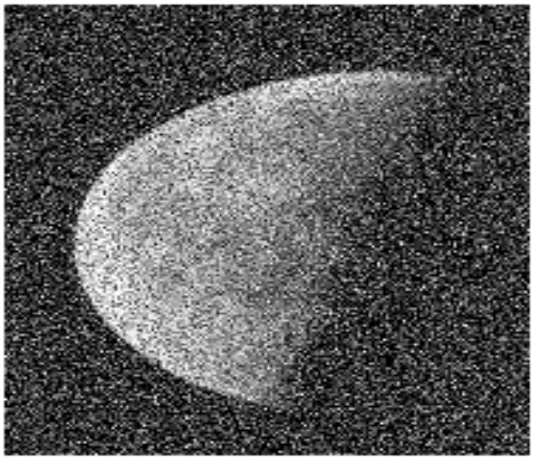

Figure 14. Image Polluted with 40% Impulse Noise

Figure 15.Filtered Image Using Intelligent Mean Filter

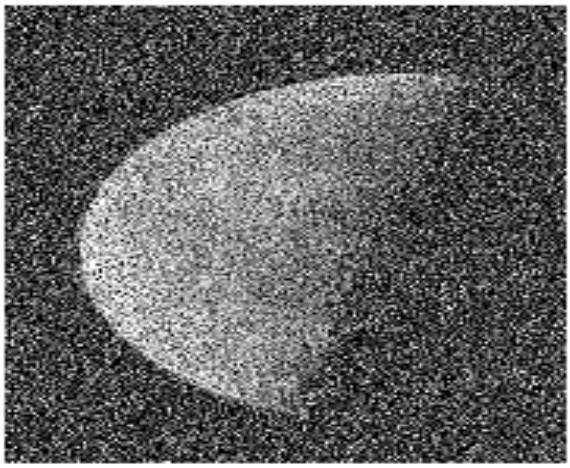

Figure 16. Image Polluted with 50% Impulse Noise

Figure 17. Filtered Image Using Intelligent Mean Filter

The original 2D grayscale 8-bit image of the moon is shown in Figure 6. The image is loaded and display using Matlab without noise added to it. Figures 8, 10, 12, 14 and 16 are the moon image corrupted with 10%, 20%, 30%, 40% and 50% salt-and-pepper noise, respectively. To show the efficiency and measure the effectiveness of the intelligent mean, the technique was applied to these corrupted images in order to produce the filtered images shown in Figures 9, 11, 13, 15 and 17. The images produced by the application of the intelligent mean clearly show that, pictorially, the noise added to the image was eliminated or significantly reduced. Figure 7 shows the distribution of the pixels in the image.

Simulation Results

Intensive simulations were carried out using several images of the moon, corrupted with various levels of impulse noise. The performance of the filtering operation was quantified using the Peak Signal-to-Noise Ratio (PSNR). The PSNR was chosen because it is one of the best known techniques for assessing the amount of noise pollution in an image and also the amount of noise that is left in a filtered image. The peak signal-to-noise criterion was adopted in order to measure quantitatively the performance of various digital filtering techniques [12]. This PSNR is defined as:

$$PSNR = 10 \log_{10} \left(\frac{255^2}{MSE} \right) \tag{3}$$

where

$$MSE = \frac{1}{MN} \sum_{j=1}^{M} \sum_{i=1}^{N} \left(G(i, j) - F(i, j) \right)^2 \tag{4}$$

and where M and N are the total number of pixels in the column and row of the image, respectively, and G denotes the noise image and F denotes the filtered image.

Table 1. Peak Signal-to-Noise Ratio of the Filtering Techniques

Filter Methods	10% Impulse Noise	20% Impulse Noise	30% Impulse Noise	40% Impulse Noise	50% Impulse Noise
Mean Filter	33.70dB	31.97dB	29.95dB	29.28dB	28.70dB
Standard Median Filter	34.35dB	32.63dB	31.39dB	30.45dB	29.67dB
Gaussian Filter	33.83dB	32.00dB	30.84dB	29.96dB	29.29dB
Adaptive Weiner Filter	33.79dB	31.98dB	30.83dB	29.95dB	29.28dB
Proposed Intelligent Mean	38.67dB	36.93dB	35.45dB	34.02dB	32.95dB

Conclusion

In this study, the authors proposed an intelligent mean filter, designed and implemented using MATLAB. The method is a very simple non-linear filter, compared to other filters, and is easier to implement in terms of noise detection and noise signal suppression. It employs a moving-window architecture that moves through the image pixels in an overlapping manner and filters the signal based on the computation of the intelligent mean per window.

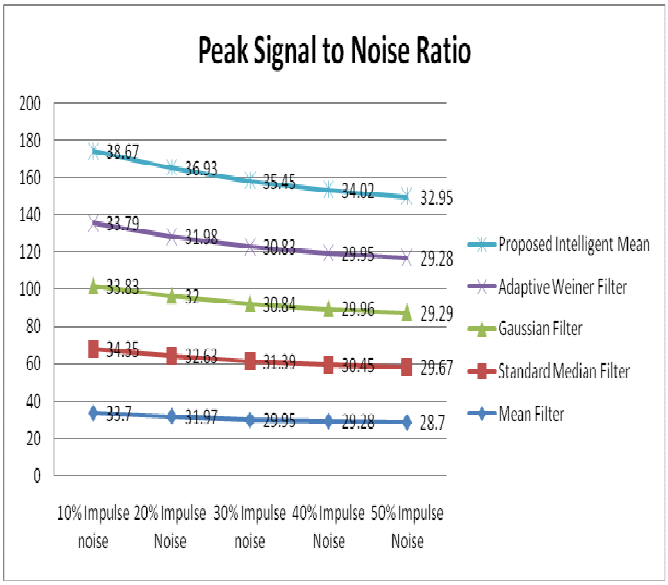

Figure 18. Graphical Representation of the Result of the Peak Signal-to-Noise Ratio in the Filtering Techniques

Extensive simulation experiments were conducted on the moon image with different levels of noise in order to compare the proposed intelligent mean technique with several other filtering techniques. The simulation results quantitatively showed that the proposed algorithm performed better than many existing state-of-the-art techniques in terms of preserving fine details of the image and drastically reducing the image noise factor.

References

[1] Yueli, H., & Huijie, J. (2009). *Research on Image Median Filtering Algorithm and its FPGA Implementation*, Global Congress on Intelligent Systems, XX, 226-230.

[2] Gonzalez, R. C., & Wood, R. E. (2007). *Digital Image Processing*, (2nd Edition), Prentice-Hall, India.

[3] Boateng, K. O., Weyori, B. A., & Laar, D. S. (2012). Improving the Effectiveness of the Median Filter. *International Journal of Electronics and Communication Engineering, 5*(1), 85-97.

[4] Mamta, J., & Parvinder, S. S. (2009). Design and Development of an Improved Adaptive Median Filtering Method for Impulse Noise Detection. *International Journal of Computer and Electrical Engineering, 1*(5), 627-630.

[5] Brownrigg, D. R. K. (1984). The weighted median filter. *Commun. ACM, 27*(8), 807–818.

[6] Ko, S.-J., & Lee, Y. H. (1991). Center weighted median filters and their applications to image enhancement. *IEEE Trans. Circuits Syst., 38*(9), 984–993.

[7] Eng, H.-L., & Ma, K-K. (2001). Noise adaptive soft-switching median filter. *IEEE Trans. Image Process., 10*(2), 242–251.

[8] Pok, G., Liu, J.-C., & Nair, A. S. (2003). Selective removal of impulse noise based on homogeneity level information. *IEEE Trans. Image Processing, 12*(1), 85–92.

[9] Hwang, H., & Haddad, R. A. (1995). Adaptive median filters: New algorithms and results. *IEEE Trans. Image Process., 4*(4), 499–502.

[10] Bovik, A. (2000). *Handbook of Image & Video Processing*, (1st Edition), New York: Academic.

[11] Gupta, G. (2011). Algorithm for Image Processing Using Improved Median Filter and Comparison of Mean, Median and Improved Median Filter. *International Journal of Soft Computing and Engineering (IJSCE), 1*(5), 304-311.

[12] Vaseghi, S. V., & Milner, B. P. (1995). *Speech Recognition in Impulsive Noise*, Instruments of Acoustics, Speech and Signal Processing, IEEE Process international conference Acoustics, Speech and Signal Processing, ICASSP-95, 437– 440.

[13] Fisher, R., Perkins, S., Walker, A., & Wolfart, E. (2003). *Noise Generation*. Department of Artificial Intelligence, University of Edinburgh, UK.

[14] Fisher, R., Perkins, S., Walker, A., & Wolfart, E. (2003). *Median Filter*. Department of Artificial Intelligence, University of Edinburgh, UK.

Biographies

BENJAMIN ASUBAM WEYORI is currently a Ph.D. Student in the Department of Computer Engineering, Kwame Nkrumah University of Science and Technology (KNUST), Kumasi, Ghana and a Lecturer at the Department of Computer Science and Information Systems, University of Energy and Natural Resources (UENR), Sunyani, Ghana. His research is in Digital image processing, Mobile Ad Hoc Networks and Artificial intelligence. He can be reached on weyoribenjamin@yahoo.co.uk

KWAME OSEI BOATENG is a Senior Lecturer and currently the Head of Computer Engineering Department, Kwame Nkrumah University of Science and Technology (KNUST), Kumasi, Ghana. Dr. Boateng has worked as a researcher at Fujitsu Laboratories Ltd., Japan and was an ICT consultant for KNUST. His research interests include; design and test of logic circuits, reconfigurable instrumentation, residue number system applications and digital signal processing. He can be reached on koboat_2000@yahoo.com

MULTI-PRODUCT CAPACITATED LOCATION ROUTING INVENTORY PROBLEM

S. Reza Sajjadi, Transsolutions; Mohsen Hamidi, Utah Valley University; S. Hossein Cheraghi, Western New England University

Abstract

The efficient design/redesign of the logistics network is essential for companies to maintain their competitive advantage. This paper presents a novel non-linear mixed-integer programming model for the multi-product capacitated location routing inventory problem (MPCLRIP), where a two-layer distribution system consisting of depots and customers was studied. The supply decisions such as location of depots, allocation of customers to the depots, finding routes to serve customers, inventory levels at depots, and product order intervals can be simultaneously and optimally made. A heuristic solution tackles the proposed combinatorial optimization problem, where a set of generated problems were solved in a reasonable computational time.

Introduction

A supply network deals with the distribution of product(s) from a source to the final customers. Smart design/redesign of the supply network is a key to cutting enterprise costs in today's competitive market. As Melo et al. [1] indicated, some typical supply chain decisions include capacity, inventory, procurement, production, routing and the choice of transportation modes. Knowing that such decisions can be classified into strategic, tactical and operational levels, a common decision process is to follow a sequential decision approach from strategic level to operational level when designing/redesigning the logistics network [2]. Due to supply chain decision interactions, such a sequential approach, however, may result in sub-optimal networks [3], [4]. Therefore, there has been a tendency by researchers and practitioners to combine two or more supply decisions. Presented by Laporte et al. [5], capacitated location routing problem (CLRP) is a classical logistics problem which takes location and routing problems into account simultaneously. When using a CLRP model, the decision maker considers three simultaneous decisions: location of facility, allocation of customers to facilities and determining routes to serve the customers. Nagy and Salhi [6] considered some real-world applications of LRP and its variant which include postal delivery, newspaper delivery, blood distribution, food distribution, school bus pick-up and delivery, waste disposal transportation and mobile healthcare. While the LRP models have been well studied, the integration of other supply decisions such as inventory and packaging problems have been dropped from the literature [6]. Moreover, the multi-commodity problem, which represents a real-life aspect of facility location and supply chain networks [1], was dropped from most LRP studies as well. Integrating inventory into the LRP model results in more complexity as more decisions are incorporated into the model. In fact, most of the integrated location, routing and inventory studies concentrate on dual combinations of location, routing and inventory including location-routing, location-inventory and routing-inventory, ignoring all of the three decisions simultaneously. As such, a body of research is also available on integrated routing-inventory and location-inventory models.

A review of the inventory-routing (IR) literature was done by Kleywegt et al. [7], [8], who reviewed the inventory-routing (IR) literature in terms of demand, vehicle, horizon, delivery and inventory characteristics. They then formulated IR as the Markov decision process and provided approximation methods for it. Their study indicates that when the inventory and routing problems are integrated, the total cost of the system is reduced. Moin and Salhi [9] classified the IR models based on their planning horizon: single period, multiple period and infinite. They also categorized the IR solution approaches into two classes: the theoretical method, where a derivation of the lower bound is determined; and, the heuristic method, where a near-optimal solution is sought. Shen et al. [10] proposed a joint inventory-location model for a network consisting of one supplier and a set of retailers to minimize the location-inventory-shipment costs in a blood-products distribution system. The study, in fact, improves the current network configuration from a decentralized system, where each retailer has a blood warehouse, to a centralized inventory system, where some retailers are identified as distribution center (DC)/depot and products (with variable demand) are shipped from there to their assigned retailers. It was assumed that the inventory policy at DCs/depots follows an approximation of the (Q,r) system, where Q is the order quantity and r is the reorder level.

In this paper, the authors present a mixed-integer programming model for a two-layer multi-product capacitated location routing inventory problem (MPCLRIP), where the classical capacitated LRP (CLRP) model is integrated with the inventory system that runs under fixed-order interval policy for multiple products at the depot level. Since CLRP

is a combinatorial optimization problem [11], an efficient heuristic solution methodology is presented to tackle the proposed model.

Literature Review

Shen [12] presented a survey on integrated supply chain models. The study proposed various integrated model formulations for location, allocation, transportation and inventory decisions. It also considered routing cost approximation when a subset of customers is assigned to the same route. The combination of location, routing and inventory literature can be classified into two categories: direct delivery and multiple delivery. Direct delivery studies assume that products are directly transported from depots to customers. In other words, each individual customer's requirement is equal to or greater than one truck load. Erlebacher and Meller [13] developed an analytical model for a stylized version of a three-layer supply chain system with capacitated plants. They considered non-linear inventory costs for the proposed continuous review policy. Moreover, the rectilinear distance is assumed from plants to DCs/depots and from there to customers.

Daskin et al. [14] formulated a non-linear integer program for a three-layer supply chain system (facility, DC/depot and retailer). They converted the model to the Lagrangian relaxation sub-problem and proposed a number of heuristics to solve it. The study applied the (Q,r) model with type I service as the inventory policy and approximated Q* using the EOQ model. The type I service assumes that the service level in the (Q,r) model is approximately equal to the probability of demand during lead time being less than the reorder point (r). Ghezavati et al. [15] studied a three-tiered distribution network that considers service level constraints and coverage radius assumptions, where demand at each depot follows the Poisson distribution. In this model, products are shipped from a single supplier to multiple potential DCs/depots and then from there to the customers. The service level constraint assumption takes the safety stock and demand costs into consideration simultaneously. The coverage radius assumption considers that each DC/depot can serve a subset of customers based on their distances from that DC/depot. Representing the solution in a matrix structure, the authors considered a genetic algorithm (GA) as the solution methodology.

In contrast to direct delivery, the multi-delivery system assumes that customer demand is less than truck load (LTL), allowing multiple customer visits on a route. An initial version of one such model that considered variable warehousing costs in the objective function of the LRP model was the work of Perl and Daskin [11], where the variable warehousing costs were involved in the objective function. Sajjadi and Cheraghi [16] proposed a multi-product LRIP model that considered a periodical inventory policy (T, I_{max}), assuming that the demand follows a stochastic distribution. The proposed model was then solved by a two-phase simulated annealing (SA) approach. Liu and Lee [17] integrated the inventory problem running under the (Q,r) policy with LRP. Liu and Lin [18] proposed a heuristic solution based on the SA and tabu search (TS) approaches to deal with the model that had been previously proposed by Liu and Lee [17]. Ambrosino and Scuttela [19] proposed four-layer static and dynamic LRP models in which there were two types of customers, while warehousing costs were considered in the objective function.

Forouzanfar and Tavakkoli-Moghaddam [20] presented a non-linear mixed-integer model for integrating location, routing and inventory decisions in a supply network where demand is uncertain. A genetic algorithm was proposed to solve various problem sizes. Klibi et al. [21] proposed the stochastic multi-period location-transportation problem (SMLTP). This study modifies three LRP assumptions in order to adopt more realistic situations by considering other transportation modes in the model such as single-customer partial truckloads, full truckloads and multi-drop truckloads. The model assumed that orders are received at depots on a daily basis, which must be fulfilled the next day. The order intervals and quantity of demand follow a probabilistic distribution.

In contrast to many transportation models that minimize the logistics costs, the proposed objective function maximizes profit as it subtracts the depot opening cost as well as inventory holding, customer shipment and production/procurement costs from sales revenue. A heuristic nested method that hierarchically combines location-allocation and transportation problems was proposed as the solution methodology. Javid and Azad [22] proposed a mixed-integer model for location-routing-inventory decisions in a supply network design. Their model considers single-product distribution, while the DCs/depots run under a continuous review system. Furthermore, the study assumed that customer demand would follow a normal distribution, the safety stock would be available to prevent depot stock out, and the DC/depot opening cost would depend on the capacity level of the DC/depot. The proposed two-phase heuristic approach considers a randomly generated constructive algorithm in the first phase, which is improved by TS and SA procedures. The improvement phase is broken down into location and routing sub-problems, where multiple procedures are proposed to improve location and routing phases sequentially. Yang et al. [23] modeled the just-in-time (JIT) delivery strategy using a two-stage integrated location-routing-

inventory problem assuming exponential distribution for customer demand. The study determined the best order interval inventory policy at depots, while it took a penalty cost into account in the objective function for late deliveries. A numerical example was solved by the proposed particle swarm optimization (PSO) approach as the solution. Results indicated that the JIT strategy reduced network costs. Other related works were conducted by Xuefeng [24], Zhang et al. [25] and Liu et al. [26].

Model Description

The following notations are used in this paper.

I = {*i*; *i*=1, 2,…, *n*}: Set of customers (second layer)
J = {*j*; *j*= *n*+1, *n*+2,…, *n*+*m*}: Set of depots (first layer)
V = {*v*; *v*=1,…, V}: Set of vehicles
P = {*p*; *p*=1,…, P}: Set of products
H = $I \bigcup J$ {*h*; *h*=1, 2…, *n*+*m* }: Set of nodes on the network including depots and customers
L_{gh} : Distance traveled from point (node) *g* to point (node) *h*, assumed symmetric
A : Ordering cost for the family of products (major setup cost)
a_p : Ordering cost for product *p* (minor setup cost)
v_p : Unit variable cost of product *p*
r : Annual inventory cost rate
H_p : Holding cost of product *p* per unit per year (H_p=r* v_p)
D_i : Annual demand of customer *i*
D_p : Annual demand for product *p*
D_{ip} : Annual demand of customer *i* for product *p*
D_{pj} : Annual demand of product *p* at depot *j*
F_j : Fixed depot opening cost of depot *j*
K_j : Capacity space of depot *j*. Products can share the space based on a standard unit volume.
K_v : Capacity of vehicle *v*. Products can share the space based on a standard unit volume.
T : Basic order interval time
t : Service order interval of the network per year
m_p : Order interval multiplier of product *p*
α_p : Volume/Size unit coefficient

Inventory Model

The inventory model proposed in this study was adopted from the model presented by Silver et al. [27]. The model represented the order interval inventory system where one orders multiple items for the warehouse in a specific time interval, T. Referring to Silver et al. [27], the annual inventory cost (IC) and optimal order interval (T*) can be obtained from Equations (1) and (2), respectively.

$$IC(T, m_p) = \frac{A + \sum_{p \in P}(a_p / m_p)}{T} + \sum_{p \in P} \frac{D_p m_p T H_p}{2} \quad (1)$$

$$T^* = \sqrt{\frac{2(A + \sum_{p \in P}(a_p / m_p))}{\sum_{p \in P} m_p H_p D_p}} \quad (2)$$

The total annual inventory cost of the system can be defined as the sum of the ordering cost and holding cost, respectively. Equation (1) indicates that there are two types of ordering costs, the ordering cost for all products together (family), known as major ordering cost (A), and the ordering costs considered for each individual product, known as minor ordering cost (a_p). The demand is known and fixed; no shortage and safety stock are allowed. Such a model is applicable when inventory cannot be continuously monitored and/or items from same supplier may yield savings in ordering, packing and shipping costs.

Moreover, when demand levels for multiple items are highly variable (e.g., low-demand product versus high-demand product), it may not be economical to replenish all items at all order times. Instead, at every time interval T, only those items that are in high demand are ordered. In fact, the time interval, T, is defined as the basic (family) order interval, and a product *p* can be ordered at a positive integer coefficient of interval T, namely product order interval, based on its annual demand size. As such, while a high-demand product is ordered every T units of time, a low-demand product may be ordered every *m*T (2T, 3T or more). The coefficient *m* was considered as a variable in the model. In a network such as the LRP, where a subset of customers is assigned to a depot *j*, Equation (2) can be re-written as follows:

$$T_j^* = \sqrt{\frac{2(A + \sum_{p \in P}(a_p / m_p))}{\sum_{i \in I} \sum_{p \in P} m_p H_p D_{ip}}} \quad (3)$$

Equation (3) calculates the optimal basic order interval time for a multiple-product multiple-customer inventory system.

Mathematical Model

The problem under consideration was a two-layer distribution system consisting of depots at the first layer and customers at the second layer. The basic assumptions of CLRP

are held by the proposed model: at each interval, a set of homogenous vehicle(s) holding limited capacity begin their tour from selected depot(s), serves a subset of customers in full and returns to the same depot(s). Each customer is served through only one vehicle, where the vehicle itself is assigned to only one depot. While the capacities of the depots and vehicles are limited, there is no individual limit on each product capacity, meaning that the products can share depot and vehicle spaces.

Depots hold inventory, and the demand for products is deterministic and the inventory policy follows the time-interval strategy explained in the previous section. It was assumed that there is no inventory cost at the customer level. The annual cost of the network includes the fixed-depot opening cost, routing cost and inventory cost. The network has a fixed and known service interval that means the network is served *t* times per year. However, this is different from the scheduling problem in which the time of the service is identified. Therefore, each route may have a different dispatching schedule during a year; however, the total annual number of dispatches is the same for all routes (1/t).

The following decision variables were used in the model:

Z_{ghv} : Routing decision: 1 if there is an immediate connection from point *g* to point *h* on route *v*, otherwise 0
X_j : Location decision: 1 if depot *j* is open, otherwise 0
Y_{ij} : Allocation decision: 1 if customer *i* is assigned to depot *j*, otherwise 0
T_j : Basic order interval at depot *j*
m_{pj} : Order interval multiplier of product *p* at depot *j*

The mathematical MPCLRIP model formulated as a non-linear mixed-integer programming model is presented as follows:

$$\text{Min} \sum_{j\in J} F_j X_j + \frac{1}{t}\sum_{\substack{h\in H\\ g\neq h}}\sum_{g\in H}\sum_{v\in V} L_{gh} Z_{ghv} + \sum_{j\in J}\frac{(A+\sum_{p\in P} a_p/m_{pj})}{T_j} X_j + \frac{1}{2}\sum_{j\in J}\sum_{i\in I}\sum_{p\in P} D_{ip} m_{pj} T_j H_p Y_{ij} \quad (4)$$

subject to:

$$\sum_{v\in V}\sum_{h\in H} Z_{ihv} = 1 \;\; i \in I \quad (5)$$

$$\sum_{g\in H, g\neq h} Z_{hgv} - \sum_{g\in H, g\neq h} Z_{ghv} = 0 \; v \in V, h \in H \quad (6)$$

$$\sum_{i\in I}\sum_{j\in J} Z_{jiv} \leq 1 \;\; v \in V \quad (7)$$

$$\sum_{g\in R}\sum_{h\in \overline{R}}\sum_{v\in V} Z_{ghv} \geq 1 \; \forall (R, \overline{R}), R \subset H, J \subseteq R \quad (8)$$

$$-Y_{ij} + \sum_{h\in H}\left(Z_{ihv} + Z_{jhv}\right) \; v \in V, i \in I, j \in J \quad (9)$$

$$\sum_{i\in I}\sum_{p\in P}\frac{\alpha_p D_{ip}}{t}\sum_{h\in H} Z_{ihv} \leq K_v \; v \in V \quad (10)$$

$$\sum_{j\in J}\sum_{i\in I}\sum_{p\in P} \alpha_p D_{ip} m_p T_j Y_{ij} - K_j X_j \leq 0 \; j \in J \quad (11)$$

$$Z_{ghv} = 0,1 \; g = 1,\ldots, n+m; \; h = 1,\ldots, n+m; \; v = 1,\ldots, v \quad (12)$$

$$X_j = 0,1 \; j = n+1,\ldots, n+m \quad (13)$$

$$Y_{ij} = 0,1 \; i = 1,\ldots, n, \; j = n+1,\ldots, n+m \quad (14)$$

$$T_j \geq 0 \; j = n+1,\ldots, n+m \quad (15)$$

$$m_p \in \text{natural number} \quad (16)$$

The objective function, Equation (4), can be explained as follows: The first term indicates the fixed opening cost of depots. The second term is the annual routing cost where the coefficient 1/t indicates the number of services per year for the network. The rest of the terms show the inventory cost: the order cost and holding cost, respectively. As explained, it was assumed that there is a base-order interval time (T_j) for a depot and then each product can be ordered every other $m_{pj} * T_j$ time, meaning that for a product with a lower demand, it is not required to order every T_j time. The constraints can be detailed as follows. Equation (5) indicates that each customer is on only one route. Equation (6) shows that every vehicle that enters a node should exit from that node. Equation (7) indicates that any vehicle on the network can depart a depot only once. Equation (8) notes the sub-tour elimination. Equation (9) shows that if a customer is assigned to a depot, there should be a route from that depot passing through the customer. Equations (10) and (11) are capacity constraints on the vehicle and depot, respectively.

Equations (12)–(15) illustrate the integrity constraints; Equations (12)–(14) are binary assumptions, while Equation (15) ensures non-negative values for the order interval decisions and Equation (16) restricts the value of m_ps to natural numbers.

Solution Methodology

The heuristic solution algorithm consists of two procedures which are performed sequentially: location-allocation-routing procedure and inventory procedure. The location-allocation-routing procedure is a modified version of the procedure developed by Sajjadi et al. [28]. The structure of this procedure is shown in Figure 1. The algorithm is composed of two components: initial solution generation and solution improvement. The improvement itself is divided into three subsections: location-allocation, allocation-routing and routing improvements.

Step one generates the initial solution; it determines which depot(s) should be open and allocates customers to the opened depots. The second step deals with the location-allocation structure; it improves the initial solution by changing the open depots and allocating the customers to the selected depots. The third step constructs tours from open depots to customers. The fourth step attempts to reduce the routing costs by changing the customer allocation; if this step changes the allocation of customers, it also constructs another set of tours from open depots to customers. The fifth step selects the best solution generated in the third and fourth steps. Finally, the sixth step improves the position of customers among the routes which are assigned to a depot.

While the model by Sajjadi et al. [28] deals with a single-product LRP, the model presented in this paper considers a multi-product LRP and so the customer may demand several types of products with different sizes and volumes. The α_p coefficient converts each product volume to a standard volume. To update the remaining capacity of depots and remaining capacity of vehicles in the above procedure, a standard unit volume (e.g., one cubic foot) must first be selected and then the total volume of each customer's demand is calculated using α_p. The depot capacity and vehicle capacity are also expressed based on the standard unit.

Using the solution from the location-allocation-routing procedure (Steps 1-6), the inventory decisions are obtained by the inventory procedure. The procedure consists of four additional steps adopted from Silver et al. [27] to find the order intervals for each product. The four steps are as follows.

Step 7. For each open depot, based on the customers allocated to the depot, calculate the total demand for each product, D_{pj}.

Step 8. Set m_{pj} =1 for the product that has the minimum:

$$\frac{\alpha_p}{D_{pj} v_p}$$

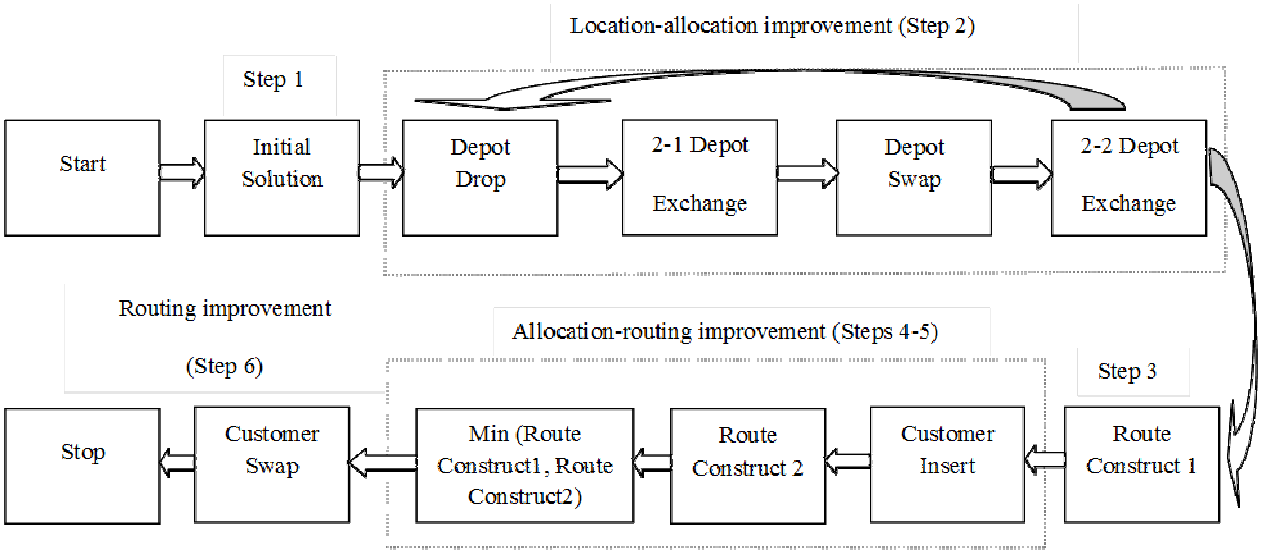

Figure 1. The structure of location-allocation-routing procedure [14]

For other products calculate m_{pj} based on Equation (17) and round it to the nearest integer greater than zero.

$$m_{pj} = \sqrt{\frac{a_p}{D_{pj} v_p} * \frac{D_{1j} v_1}{A + \alpha_1}} \quad (17)$$

Step 9. Calculate the basic order interval by Equation (18):

$$T_j = \sqrt{\frac{2\left(A + \sum_p {}^{a_p}/_{m_{pj}}\right)}{r \sum_p m_{pj} D_{pj} v_p}} \quad (18)$$

Repeat Steps 7–9 for all open depots.

Step 10. The annual inventory cost for each depot (IC_j) is calculated from Equation (19). The total inventory cost will be the sum of the inventory costs of all open depots.

$$IC_j = \frac{A + \sum_{p \in P} {}^{a_p}/_{m_{pj}}}{T_j} + \sum_{p \in P} \frac{D_{pj} m_{pj} T_j v_p r}{2} \quad (19)$$

Numerical Example and Computational Analysis

The above heuristic algorithm was coded in MATLAB R2012b on an Intel(R) Core(TM) i7-3770S CPU @ 3.10 GHz machine with 8.00 GB of RAM. A numerical example consisting of 100 customers, 10 depots and 5 products was solved using the proposed algorithm. The location and capacity of the depots and vehicles were obtained from the dataset by Prins et al. [29].

As the data set takes single products into consideration, the problem was broken down in order to represent multiple -product problems (five products). The input inventory assumptions were assumed as follows: 1) The major setup cost for the family of products, A, is \$1,000; 2) The annual inventory cost of one dollar of inventory, *r*, is \$0.25; and, 3) The minor setup cost, a_p, and the unit variable cost, v_p, for each product are shown in Table 1. Moreover, the volume/ size unit coefficient, α_p, which converts different product sizes to a standard unit volume, is shown in Table 1. As proposed, the algorithm consists of 10 steps of which Steps 1-6 solve the location-routing problem and Steps 7-10 take the inventory decision into account. Figure 2 plots the location-routing solution, indicating how the initial LRP solution would be improved from Step 1 to Step 6. The total demand for each product at each depot, D_{pj}, is shown in Table 2. Tables 3-6 indicate the inventory solution for the problem (output), which is the result of Steps 7-10 of the proposed heuristic algorithm.

Table 1. Minor Setup Cost and Unit Variable Cost (dollars)

Product	a_p(\$)	v_p(\$)	α_p
Product 1	200	4000	10
Product 2	240	500	6.67
Product 3	280	2500	2
Product 4	320	500	0.67
Product 5	360	3500	0.36

Table 2. Demand at Open Depots

Product	Depot 3	Depot 5	Depot 8	Depot 9
Product 1	6	9	9	8
Product 2	8	14	14	12
Product 3	28	46	46	42
Product 4	83	137	138	125
Product 5	152	252	253	229

Table 3. Basic Order Interval

Opened Depot	T_j , in years	T_j , in days
Depot 3	0.1439	53
Depot 5	0.1121	41
Depot 8	0.1119	41
Depot 9	0.1177	43

Table 4. Order Interval Multipliers

Product	m_{pj}
Product 1	2
Product 2	5
Product 3	1
Product 4	2
Product 5	1

Table 5. Order Interval Time and Inventory Cost

Product\Depot	Depot 3	Depot 5	Depot 8	Depot 9
Product 1	106	82	82	86
Product 2	265	205	205	215
Product 3	53	41	41	43
Product 4	106	82	82	86
Product 5	53	41	41	43
Inventory Cost (\$), ICj	27,082	34,767	34,830	33,109

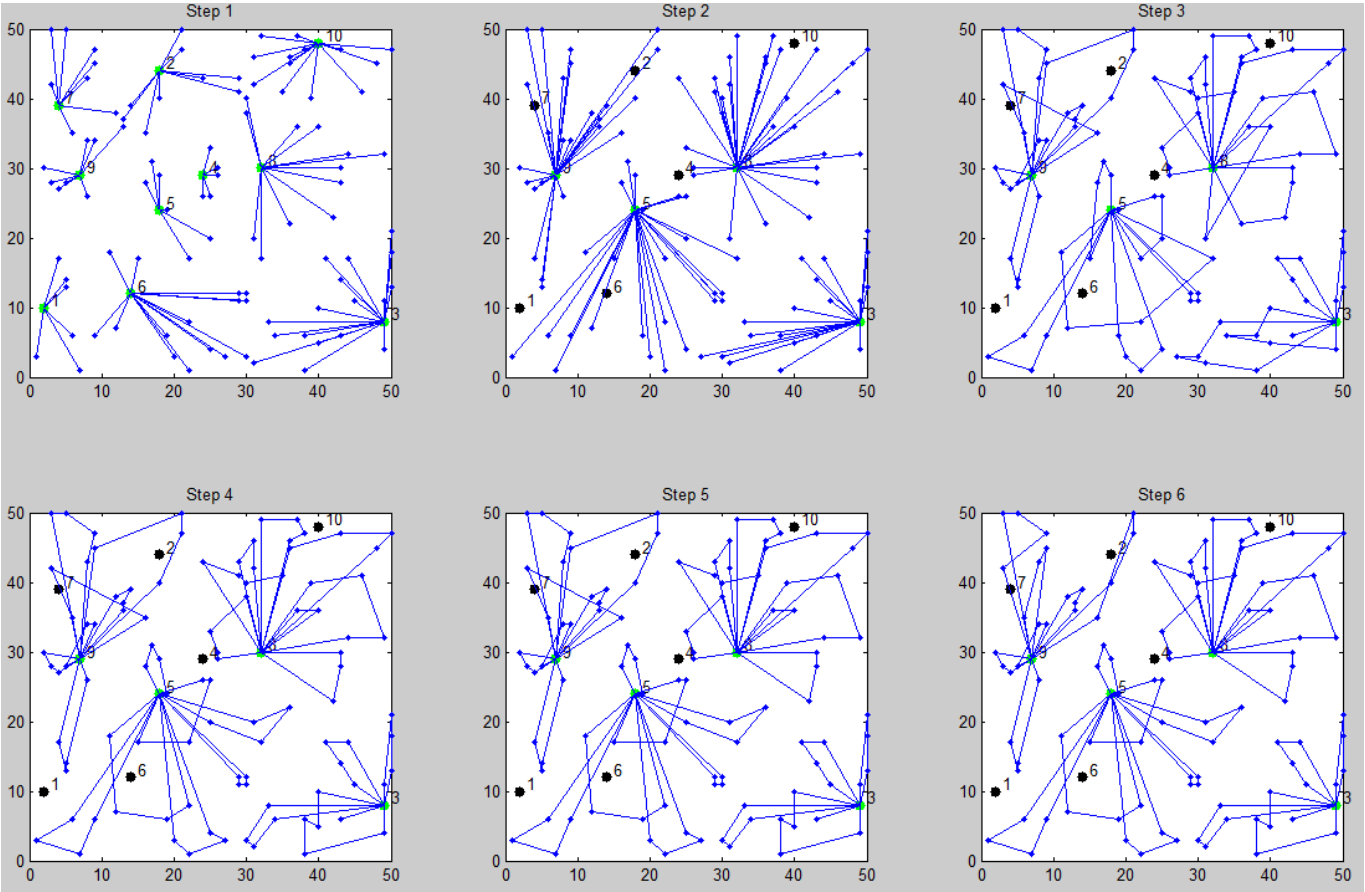

Figure 2. Location-Routing Solution for 100-10-1 Benchmark Problem

Table 6. Solution Results

Benchmark Problem	T_j , in days, at opened depots				Cost ($)		
					Location-Routing	Inventory	Total
20-5-1	74	112	82	-	55,908	49,201	105,109
20-5-2	111	80	77	-	49,403	48,944	98,347
50-5-1	56	57	53	-	92,484	77,462	169,946
50-5-2	58	61	47	-	92,501	77,948	170,449
100-5-1	56	33	35	-	281,820	109,485	391,305
100-5-2	32	31	-	-	199,159	90,697	289,856
100-10-1	53	41	41	43	323,577	129,788	453,365
100-10-2	39	40	37	-	249,332	110,272	359,604
200-10-1	25	32	26	-	485,749	155,837	641,586
200-10-2	29	25	28	-	456,304	156,383	612,687

The proposed algorithm determined the opening of depots 3, 5, 8 and 9 (Table 3). The basic order intervals, T_j, are presented in the table as well. The order interval multipliers of products at open depots, m_{pj}, are shown in Table 4. Also, the order interval times for each product at each depot, $m_{pj}*T_j$, and the inventory costs, IC_j, are presented in Table 5.

In addition to the numerical example, using the developed algorithm, two sets of problems were solved. First, in order to verify the accuracy of the algorithm, a small-size problem consisting of two depots, two products and three customers was solved and then the results were compared to the optimal solution obtained from the enumeration method. It was observed that the proposed algorithm is capable of achieving the optimal solution for the problem under study. Second, a set of problems with different sizes was solved. To form the problems, the inventory data (same as the numerical example) were added to a set of LRP benchmark problems obtained from the dataset by Prins et al. [29]. From each problem size in the dataset, two problems were solved. Similar to the numerical example, the number of product types was set to five.

Compared to the work by Silver et al. [27] and Sajjadi et al. [28], the proposed algorithm generates quality solutions for Steps 1-6 and Steps 7-8, respectively (see Table 6). Note also that the multipliers, m_{pj}, for each product at all depots in all problem sizes are the same (see Table 4). The reason is that the multiplier value is greatly affected by the inventory data, which were the same for all of the problems considered in this study. In each problem, the algorithm balanced the depots and tried to use as much capacity as possible from the open depots. Since the demands for each product at the open depots were not very far from each other, the algorithm computed the same multipliers at the open depots. However, as expected, T_j was more sensitive to demand levels than m_{pj}. That is why the T_j values, shown in Table 6, were different for each depot and in each problem. In fact, as demand increased, T_j decreased. For example, consider the T_j values for the 20-5-1 problem. The solution indicated that there should be three open depots in the network with T_j of 74, 112, and 82 days. Product 1, in open depot 1, should be ordered every 2*74 days, while product 2 should be ordered every 5*74 days, etc.

In order to show the capability of the proposed algorithm, the effect of using different order intervals for different products on the inventory, cost was considered in Table 7. If each depot wants to order all products at the same order interval (m_{pj}=1), as the classical order interval policy assumes, the inventory cost increases. It is indicated in Table 7 that for the benchmark problems, the inventory cost increases by almost 5%. This shows that the proposed algorithm is effective in decreasing the cost. Since the proposed model is novel, there is no exact benchmark problem that can be compared to this computational time. However, the computational time for the benchmark problems in this study were compared with the time obtained from the LRGTS algorithm proposed by Prins et al. [30]. Figure 3 shows the plots of the computational time for the considered problems. It was shown that the CPU time for the proposed algorithm was much less than that of the LRGTS.

Table 7. Classical versus Proposed Order Intervals Inventory Cost Effect

Benchmark Problem	Inventory Cost with *Different* Order Intervals	Inventory Cost with *One* Order Interval	Increase in Inventory Cost
20-5-1	49,201	51,662	5.00%
20-5-2	48,944	51,322	4.86%
50-5-1	77,462	81,217	4.85%
50-5-2	77,948	81,732	4.85%
100-5-1	109,485	114,837	4.89%
100-5-2	90,697	95,131	4.89%
100-10-1	129,788	136,158	4.91%
100-10-2	110,272	115,628	4.86%
200-10-1	155,837	163,427	4.87%
200-10-2	156,383	164,053	4.90%

Considering that the proposed algorithm in this study takes both the inventory decision and multiple product system into consideration, while the LRGTS only considers a CLRP model, it can be concluded that the solutions are generated in a reasonable amount of time.

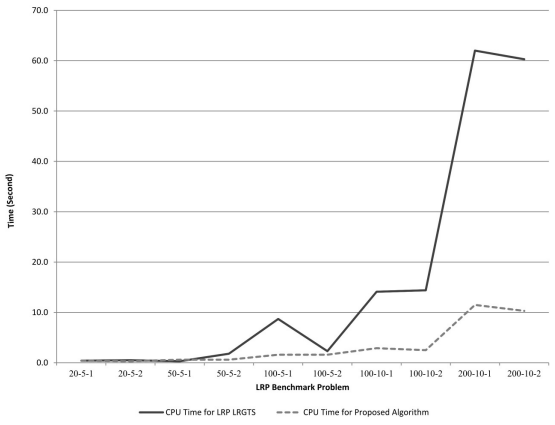

Figure 3. CPU-Time Comparison

Conclusion

A novel mathematical model for multiple-product capacitated location routing problems that takes into account inventory decisions was proposed in this study. The inventory procedure takes the time interval policy into account where the basic time interval is determined for each open depot, and computed multipliers indicate the time interval order for each product. Such a model is especially appropriate when demands for different products vary greatly, making a wide customer request range. A heuristic solution that combines a modified version of the work by Silver et al. [25] and Sajjadi et al. [26] was proposed as the solution approach. Benchmark problems obtained from the LRP literature were combined with inventory parameters set by the authors and then solved by the proposed algorithm. A numerical example was also solved to show how the proposed algorithm tackles the problem. Future research is needed to consider demand uncertainty in the model. Furthermore, heuristic solution approaches that consider inventory decision and location routing problems simultaneously rather than sequentially should also be considered in future studies.

References

[1] Melo, M.T., Nickel, S., & Saldanha-da-Gama, F. (2009). Facility location and supply chain management- A review. *European Journal of Operational Research*, *196*, 401-412.

[2] Chopra, S., & Meindl, P. (2007), *Supply chain management: Strategy, planning, and operation*, 3rd ed., Upper Saddle River, New Jersey.

[3] Srivastava, R. (1993). Alternate Solution Procedures for the Location-Routing Problem, *OMEGA: International Journal of Management Science*, *21*(4), 497-506.

[4] Miranda, P. A., & Garrido, R. A. (2006). A simultaneous Inventory Control and Facility Location Model with Stochastic Capacity Constraints, *Network and Spatial Economics, 6*(1), 39-53.

[5] Laporte, G., Nobert, Y., & Arpin, D. (1986). An exact algorithm for solving a capacitated location- routing problem, *Annals of Operations Research*. *6*(9), 293-310.

[6] Nagy, G., & Salhi, S. (2007). Location- routing: Issues, models and methods. *European Journal of Operational Research, 177*(2), 649-672.

[7] Kleywegt, A. J., Nori, V. S., & Savelsbergh, M. W. P. (2004). Dynamic programming approximation for a stochastic inventory routing problem. *Transportation Science, 38*(1), 42-70.

[8] Kleywegt, A. J., Nori, V. S., & Savelsbergh, M. W. P (2002). The stochastic inventory routing problem with direct deliveries, *Transportation Science, 36*(1), 94-118.

[9] Moin, N. H., & Salhi, S. (2007). Inventory routing problems: a logistical overview, *Journal of the Operational Research Society, 58*, 1185-1194.

[10] Shen, Z. J. M., Coullard, C., & Daskin, M. S. (2003). A Joint Location-Inventory Model. *Transportation Science, 37*(1), 40–55.

[11] Perl, J., & Daskin, M. S. (1985). A warehouse location-routing problem, *Transportation Research Part B: Methological, 19*(5), 381-396.

[12] Shen, Z. J. M. (2007). Integrated supply chain design models: a survey and future research direction. *Journal of Industrial and Management Operation, 3*(1), 1 -27.

[13] Erlebacher, S. J., & Meller R. D. (2000). The interaction of location and inventory in designing distribution systems. *IIE Transactions, 32*(2),155-166.

[14] Daskin, M. S., Coullard, C., & Shen, Z. J. M. (2002). An Inventory-Location Model: Formulation, Solution Algorithm, and Computational Results. *Annals of Operations Research, 110*, 83-106.

[15] Ghezavati, V. R., Jabal-Ameli, M. S., & Makui, A. (2009). A new heuristic method for distribution networks considering service level constraint and coverage radius. *Expert Systems with Application, 36*(3), 5620-5629.

[16] Sajjadi, S. R., & Cheraghi, S. H. (2011). Multi-products location-routing problem integrated with inventory under stochastic demand. *International Journal of Industrial and Systems Engineering, 7*(4), 454-476.

[17] Liu, S. C., & Lee, S. B. (2003). A two phase heuristic method for the multi depot location routing problem taking inventory control decision into consideration. *International Journal of Advanced Manufacturing Technology, 22*, 941-950.

[18] Liu, S. C., & Lin, C. C. (2005). A heuristic method for the combined location routing and inventory problem. *International Journal of Advanced Manufacturing Technology, 26*(4), 372-381.

[19] Ambrosino, D., & Scutella, M. G. (2005). Distribution network design: new problems and related models. *European Journal of Operational Research, 165* (3), 610-624.

[20] Forouzanfar, F., & Tavakkoli-Moghaddam, R. (2012).Using a genetic algorithm to optimize the total cost for a location-routing-inventory problem in a supply chain with risk pooling. *Journal of Applied Operational Research, 4*(1), 2–13.

[21] Klibi, W., Lasalle, F., Martel, A., & Ichoua, S. (2010). The Stochastic Multi-Period Location-Transportation Problem. *Transportation Science, 44* (2), 221-237.

[22] Javid, A. A, & Azad, N. (2010). Incorporating location, routing and inventory decisions in supply chain network design. *Transportation Research, Part E, 46* (5), 582–597.

[23] Yan, X., M, H., & Zhan, D. (2010). Research into ILRIP for Logistics Distribution Network of Deteriorating Item Based on JITD. *Proceeding of the Information Computing and Applications - International Conference, ICICA, Part I*,(pp.152-160), Tangshan, China.

[24] Xuefeng, W. (2010). An integrated multi-depot location-inventory-routing problem for logistics distribution system planning of a chain enterprise. *Proceeding of the international Conference on Logistics Systems and Intelligent Management* (vol.3, pp.1427 – 1431).

[25] Zhang, B., Ma, Z., & Jiang, S. (2008). Location-Routing-Inventory Problem with Stochastic Demand in Logistics Distribution Centers. Proceeding of the *4TH International Conference on Wireless Communication, Networking and Mobile C (pp.* 1-4).

[26] Liu, G-S, Wang, C-Y, & Chen Z-Y. (2009). A study of inventory-routing problem for the distribution system of a distribution center. *Proceeding of 7th IEEE International Conference on Industrial Informatics,* (pp. 847-852).

[27] Silver, E. A, Pyke, D. F., & Peterson, R. (1998). *Inventory Management and Production Planning and Scheduling*, 3rd ed., John Wiley & Sons, New York, USA.

[28] Sajjadi, S. R., Hamidi, M., Farahmand, K., & Khiabani, V. (2011). A greedy heuristic algorithm for the capacitated location-routing problem. *Proceedings of the 2011 Industrial Engineering Research Conference (IERC)*, Reno, NV, USA.

[29] Prins, C., Prodhon, C., & Wolfler-Calvo, R. (2004). Nouveaux algorithms pour le problème de localisation et routage sous contraintes de capacité. *Proceedings of the International Conference on Modeling, Optimization & SIMulation* (vol.2, pp.1115–1122), Lavoisier, Ecole des Mines de Nantes, France.

[30] Prins, C., Prodhon, P., Ruiz, A., Soriano, P., & Wolfler-Calvo, R. (2007). Solving the Capacitated LRP by a Cooperative Lagrangean Relaxation-Granular Tabu Search Heuristic, *Transportation Science, 41*(4), 470-483.

Biographies

S.REZA SAJJADI is an Associate in Transsolutions, LLC. He received his B.S., M.S., and Ph.D. in Industrial Engineering. He earned his Ph.D. from the Wichita State University in 2008 and currently develops simulation model for transportation systems. His research interests are applying Operations Research tools in real life applications. He may be reached at rsajjadi@transsolutions.com

MOHSEN HAMIDI is an Assistant Professor of Operations Research in Finance and Economics department at Utah Valley University. He earned his PhD in Industrial Engineering from North Dakota State University and received his BS and MS in Industrial Engineering from Sharif University of Technology. His research interests are optimization and operations research. Mohsen also has six years of working experience in industry. He can be reached at Mohsen.Hamidi@uvu.edu

S. HOSSEIN CHERAGHI is professor and Dean of the College of Engineering at Western New England University. He received his Ph.D. in Industrial Engineering from The Pennsylvania State University, University Park, Pennsylvania in 1992. His areas of interest include modeling, analysis and control of systems and processes, applied optimization, manufacturing error analysis, and tolerancing in design and manufacturing. He has been involved with funded projects from the FAA, Boeing, Cessna, and the NSF, and has published over 140 articles in internationally recognized journals and conference proceedings. He may be reached at cheraghi@wne.edu

DEFINITIONS OF PERSPECTIVE DIMINUTION FACTOR AND FORESHORTENING FACTOR: APPLICATIONS IN THE ANALYSIS OF PERSPECTIVE DISTORTION

Hongyu Guo, University of Houston–Victoria

Abstract

There has been considerable confusion about the terms perspective diminution and foreshortening in the literature. Foreshortening factor has been defined and investigated in computer graphics literature, but only for the case of parallel projections. The case for perspective projection does not appear to have been investigated. In this paper, these concepts are elucidated through rigorous quantitative definitions of the perspective diminution factor and foreshortening factor. The inverse law and inverse square law that govern the perspective diminution factor and the perspective foreshortening factor in relation to depth were investigated and applied to a quantitative analysis of perspective distortion.

Introduction

Depth Perception and Representation by Humans and Computers

Human perception of the three-dimensional (3D) world is accomplished via a central projection onto the 2D retina. Because the retina has fewer dimensions, after the projection, the depth information of the original 3D scene is lost. This creates two tasks of opposite nature. One is depth perception, which is the inference of a 3D scene out of a 2D image. The other is depth representation, which is to output an image onto 2D media, given a 3D model. Humans have learned to deal with both. Depth perception is acquired through subconscious learning. Depth representation on 2D media is the art of perspective drawing, which was discovered in early Renaissance. Today, computers must deal with these, too, and which represent research topics in computer vision (for depth perception) and computer graphics (for depth representation).

In most of the situations in everyday life, a human can cope with this loss of depth information by using depth cues [1-3]. For example, when one is driving on the highway and sees cars ahead, there is first a process of object recognition; the images are recognized as cars. Next, prior knowledge is called upon; that is, all of the cars have approximately the same size, so prior knowledge must be used as a depth cue. A bigger image of the car indicates a shorter distance in depth, while a smaller image indicates a greater depth. Objects that are farther away look smaller. This phenomenon is known as perspective diminution.

Occasionally, the eyes are deceived, as in the case of trompe l'œil art. One popular form of trompe l'œil art is the chalk art on street pavements, creating 3D illusions. Julian Beever is one of these popular street pavement artists [4]. When viewed from a certain angle, the chalk drawing on the pavement can be perceived as points on certain 3D objects with varying depth; but, in fact, those are just points with colors on the ground plane. This illusion is called depth ambiguity, which is caused by the central projection.

Perspective Diminution and Foreshortening

The perspective diminution was understood even in prehistory art. However, the precise representation of depth on 2D media was not discovered until the Renaissance, when the principles of perspectives were fully understood. Before and during early Renaissance, artists had struggled with perspective drawing and had made various mistakes in inaccurate diminution rate of objects in depth.

The terms perspective diminution and foreshortening have been widely used in fine art, computer graphics and computer vision. However, the definitions of these terms tend to be vague and confusing. These two terms are also often used interchangeably [5]. William Longfellow [6] pointed out:

> The distinction between mere diminution from distance, and foreshortening, which is diminution from obliquity of view, is not to be forgotten here. If we stand in front of a square or circle, its plane being at right angles to our line of vision, it looks like a square or circle at any distance; it may grow larger or smaller, but its proportions do not change. If we look at it obliquely, the farther parts diminish more than the nearer, the lines that are seen obliquely

more than those that are seen squarely, and the shape is distorted. This is foreshortening. (p.2)

However, to the best of the author's knowledge, a quantitative analysis of perspective diminution and foreshortening is still missing in the literature today. Figure 1 is a drawing by Jan Vredeman De Vries, a Dutch artist in the Renaissance, in his book *Perspective* [7], published in 1604. It illustrates perspective diminution and foreshortening. When a person stands vertically but moves back in the depth direction, his size diminishes (diminution) and the different parts of his body diminish proportionally. When a person is lying down on the ground along the depth direction, the different parts diminish disproportionately, with the part in greater depth diminishing much faster (foreshortening).

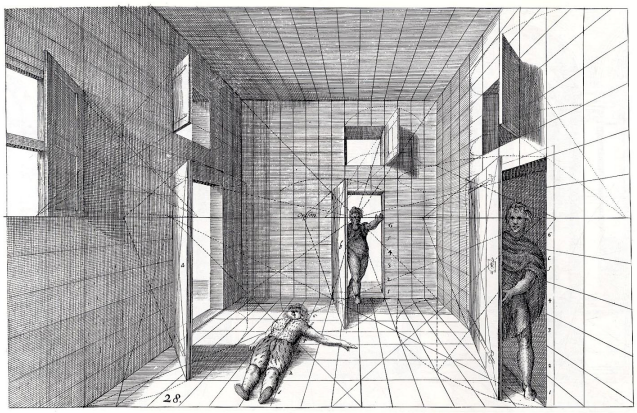

Figure 1. Perspective Diminution and Foreshortening [7]

In computer graphics literature, the foreshortening factor is defined for parallel projections, but not for central projections [8]. In parallel projections, the foreshortening factor is a constant, depending only on the angle of parallel projection lines to the image plane and the orientation of the line in 3D space relative to the image plane, but independent of depth. The computer graphics literature does not distinguish diminution from foreshortening either, because in parallel projection there is no diminution with depth. The diminution in depth in the central projection case has not been discussed.

The situation for central projection is more complicated because this factor also depends on the depth. The relationship between the length of the object in 3D space and its 2D projection is nonlinear if the object has a span in depth. It is even different along transverse directions and the depth direction. Because of this, two different factors, diminution and foreshortening, are defined in this paper; they are also defined locally in the differential sense for small-sized objects. The laws that govern the perspective diminution and foreshortening factors are investigated and applied to a quantitative analysis of perspective distortion.

Depth Inference from a Single Image in Machine Vision

Even with the loss of depth information in an image, humans can easily make inferences about 3D depth by examining a photograph in most situations, except for some exceptional cases like that of trompe l'œil art. Of course, such depth inference relies on object recognition and prior knowledge of the 3D objects, which are known as depth cues. One example of such depth cues is the known size of familiar objects like human figures or cars. Another example is the recognition of some planes and line segments and prior knowledge of their orientations; for example, the ground plane and the trunks of trees. It is known that the trunks of trees are in the vertical direction and, hence, all of the points on the same trunk have the same depth. The leaves connected to the trunk should have approximately the same depth, too. Since the bottom of the trunk is on the ground plane, this depth cue can be used to figure out the depth of the bottom of the trunk. Hence, the depth of the entire trunk and that of the leaves can be easily solved.

Finding space distance through measurements on the photographs has long been the effort in photogrammetry and machine vision. Accurate and fast depth calculation from images is important in machine vision and applications in unmanned vehicles [9-11] and robotics [12]. It is well understood that at least two photographs taken from different angles are needed in order to recover the depth information. Recently, there have been new efforts in depth inference from a single image [13-19]. Part of the reason is that stereopsis has its own drawbacks. In theory, stereopsis can find depth for any situation, though in practice it depends on the feature points extraction and registration of feature points in two images. When the depth is too large, the difference in the two images is too small, the uncertainty will be too big and in, general, will fail. This leads to an argument that a robot is better off being equipped with one eye than two [20].

However, depth inference from a single image is an ill-posed problem, and it makes sense only with prior knowledge and assumptions about the scene. For example, when a photograph of buildings and trees is given, it is possible that this is a photograph of the 3D scene with varying depth, but it is equally possible that this is a photograph of a photograph hanging on the wall, in which case all of the pixels have the same depth. Unavoidably, all of the depth inference from a single image relies on depth cues. Crankshaw [13] used computer-aided depth inference with appli-

cations in computer graphics to translate the photographic view of a building into the plan view. This process is known as reverse perspective analysis. Yu et al. [21] preprocessed the image in order to detect edges, extract straight lines, group the lines to form quadrilaterals and group them as planes. Saxena et al. [18] used supervised learning methods for depth inference. The results of these efforts was a depth map of the image, meaning a depth value was assigned to each pixel in the image. Experiments have been done with controlled scenes, the inferred results from which were compared with ground truth, which is a depth map obtained with a 3D laser scanner. The process is fully automated. However, this goal of fully automated and depth inference for each pixel seems too ambitious and the error rate is likely to be high [18].

A Model of the Camera and the Scene

The projective model for the camera and the scene are described next. The discussion in this paper is based on these assumptions of the camera model and the scene model. In the theory of optics, the subject distance μ (distance from the object to the center of the lens), the image distance v (distance from the image to the center of the lens) and the focal length f of the lens are related by

$$\frac{1}{u}+\frac{1}{v}=\frac{1}{f} \tag{1}$$

For different subject distance, μ, the image distance v is different. If the scene is non-planar in a 3D space, the image points of the scene do not lie in the same plane. A more precise definition of a scene will be presented shortly.

In practice, the film or image sensor of the camera is a plane. For each 3D scene point, a very small circular disk, called a circle of confusion, is recorded on the image sensor. When the scene point is within the depth of field, the circle of confusion is so small that it is indistinguishable from a point to the human eyes. This leads to the projective model, or geometric model, of a camera. It is also called the pinhole camera model. The image of the 3D world is the central projection on the image plane. The center of projection (COP) is the optical center of the lens.

Practically, with the cameras for photography, the image distance is slightly bigger than the focal length of the camera lens. When optics is not the concern, the term focal length and image distance are often used interchangeably in photography. The image plane (image sensor) of a camera is behind the lens and the image is upside down. With the geometric model of the camera, it does not hurt if the image plane is placed in front of the COP, just like the canvas of the artist. Everything in theory will be the same, but the image will be upright. In computer graphics, animation and video games, a virtual camera is employed. The image plane is the computer screen, which is the viewing window. The COP of the virtual camera is also called the viewpoint and is located in the position of the eye of the user of the computer. The virtual camera looks into this viewing window and sees the 3D virtual world, which is projected onto the computer screen. In the following discussion, the projective camera model is used.

A clarification of the scene is needed. A scene is defined to be a subset, S, of points in the 3D space. Some restrictions on subset S need to be imposed in order to be considered a scene. Let the origin of the coordinate system with $(x,y,z) = (0,0,0)$ coincide with the COP. The convention in some computer graphics applications (like DirectX) is to make the positive z pointing into the depth direction of the scene. It is assumed that all of the scene points are located in the half space $z > 0$. Imagine that all projection rays radiate into the half space, $z > 0$, starting from COP. It is further assumed that each ray intersects with S on at least one point. In general, the entire half space is not considered as a scene. It does not hurt but it is just not interesting or useful looking at a photograph of dense fog with a uniform gray color recorded on the image. Occlusion is allowed in the scene for the scene model to be general enough. If a ray intersects with S at more than one point, occlusion occurs. In such a case, the front-most point (with the lowest z value) will be projected onto the image plane, while other points on the same ray will be occluded and will not show up in the image.

A curved smooth surface is an example of a scene, but a scene is not limited to a single smooth surface. Surfaces with sharp edges, like a cube, can be part of a scene, where smoothness of the surface is not assumed. Occlusion in the scene in general is allowed. A sphere in front of a background surface is an example. In such cases, when the projection ray sweeps continuously across the scene, discontinuity in the z direction may occur. Buildings and trees, together with the ground surface, are an example of a scene. If any closed surface (like a cube or a sphere) has the interior as part of a scene, all of the interior points will be occluded and will not show on the image, no matter from what angle the image is taken. The back faces of the closed surface will be occluded as well. Only the front faces will show on the image.

In general, the scene points do not lie on the same plane. The terms 3D scene and non-planar scene are used inter-

changeably. A special case of a scene is when all of the scene points are located on a plane embedded in the 3D space. Such a scene is called a planar scene or 2D scene.

Perspective Diminution Factor and Perspective Foreshortening Factor

Coordinate Setup for Perspective Projection

A coordinate system (x,y,z) is set up with the origin O at the COP, as shown in Figure 2. The image plane is parallel to the x - y plane with an image distance f. Imagine a person is looking through this virtual camera. It is customary for the viewer to set positive x in the right direction, positive y in the upward direction and positive z in the forward or the depth direction. This way, all of the scene points that a viewer can see have positive z values that increase as a point moves forward, from the viewer's perspective. This convention of coordinate setup results in a left-handed coordinate system. In computer graphics applications, Microsoft DirectX adopts this left-handed coordinate system as its default for this viewer's convention. The x and y directions are called transverse directions, while the z direction is called the longitudinal or depth direction. On the image plane, an X - Y coordinate system is used. X is parallel to x and y is parallel to y, with C at the origin, where C is the principal vanishing point and is the intersection of the image plane and the z axis.

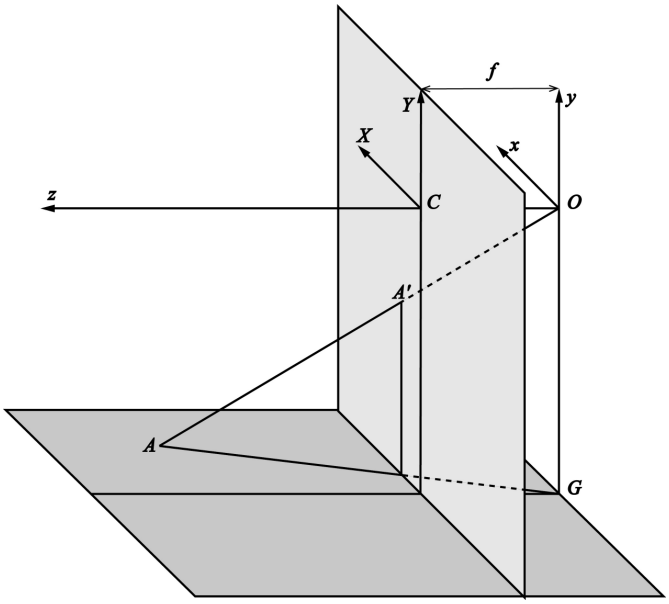

Figure 2. Camera Coordinate System Setup and Perspective Projection

With this coordinate system setup, for any scene point A with coordinates (x,y,z) in 3D space, the coordinates (X,Y) of the image point A' in the image plane are

$$X = f\frac{x}{z}$$
$$Y = f\frac{y}{z} \qquad (2)$$

Perspective Diminution Factor

For simplicity, a scene point, P , in the y - z plane ($x = 0$) is considered in Figure 3. However, this restriction of $x = 0$ is not necessary for the theory to hold; it simply makes the diagram easier to draw and easier to see. The definition of perspective diminution factor, perspective foreshortening factor, as well as the following theorems apply to any scene point with any x,y,z coordinate values.

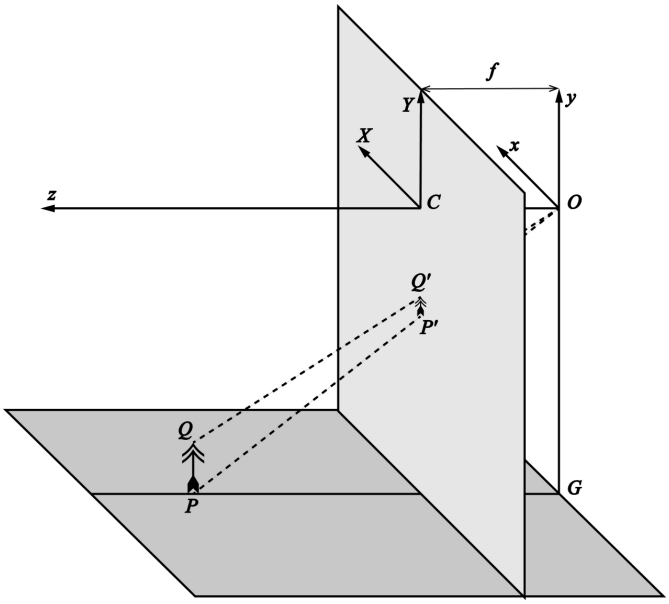

Figure 3. Perspective Diminution Factor

In perspective projection, the length in 3D space and the length of its projected image on the image plane have a nonlinear relationship. Locally, this nonlinear relationship can be approximated linearly using differential calculus. It is assumed that the object is a small line segment, PQ. Assume the line segment PQ is in the transverse y direction. After perspective projection with the center at O, the images of P and Q are P' and Q', respectively. If you imagine that PQ is a small tree on the ground, then $P'Q'$ is its image on the film of the camera.

Suppose point P has depth z and vertical coordinate y. Note that y is the vertical coordinate of point P, instead of the size of PQ. The size of the object is denoted by $\Delta y = PQ$. The size of the image is denoted by $\Delta Y = P'Q'$. From Equation (2), when z is kept constant but y is varied by a small amount (Δy), the image Y will change by ΔY:

$$\Delta Y = P'Q' = \frac{f}{z} PQ = \frac{f}{z} \Delta y \tag{3}$$

In the limit of $PQ \to 0$, the ratio

$$\lim_{PQ \to 0} \frac{P'Q'}{PQ}$$

is a constant, which shall be defined as the perspective diminution factor.

Definition 1. *Suppose a small object has coordinates* (x,y,z) *in 3D space and its image has coordinates* (X,Y) *in the image plane. The quantity*

$$M_{\parallel} = \left| \frac{\partial Y}{\partial y} \right| \tag{4}$$

is called the ***perspective diminution factor*** *at depth z.*

The symbol $M_{\parallel}$ is used because the transverse direction is parallel to the image plane. The diminution factor defined above is similar to the transverse magnification of optical systems, but here the projective model of the camera is used. It can easily be found that the diminution factor is completely determined by the depth z of the object in 3D space, and has nothing to do with optics.

It should be mentioned that it was assumed earlier that the object line segment PQ is oriented along the vertical y direction to intuitively motivate the definition but, in fact, Definition 1 applies to objects of any orientation (other than exactly parallel to the x - z plane, which has no variation in y). In this definition of the diminution factor, the key is to take the partial derivative of Y with respect to y. The object can be oriented in any direction, as long as there is a variation in y.

Theorem 1. *The perspective diminution factor* $M_{\parallel}$ *of an object located at* (x,y,z) *is inversely proportional to its depth z, as shown in Equation (5)*

$$M_{\parallel} = \frac{f}{z} \tag{5}$$

where f is the image distance, which is an intrinsic parameter of the camera.

The proof is straightforward by taking the partial derivative of Y with respect to y in Equation (2).

Meaning of the diminution factor. Suppose that PQ has unit length. When it is placed at a depth z and parallel to the y direction, $M_{\parallel}$ represents the size (height) of the image $P'Q'$. $M_{\parallel}$ is a function of depth z. The diminution factor in the x direction is similar to the y direction.

Corollary 1. *The perspective diminution factor can be equivalently defined as the magnification in the x direction. That is,*

$$M_{\parallel} = \left| \frac{\partial X}{\partial x} \right| = \frac{f}{z} \tag{6}$$

In most of the photographs in which the objects are far enough away (z big enough), $M_{\parallel} < 1$ holds, which means that the image is smaller in size than the object; although, under certain circumstances, when the depth z is small compared to the image distance, it is possible to have $M_{\parallel} > 1$, as in close-up photography and microscopic photography.

Perspective Foreshortening Factor

The magnification along the depth direction z (which is called foreshortening when the magnification is less than one) is quite different from the transverse magnification (diminution in y direction). In Figure 4, suppose that the segment PR is in the z direction with size $\Delta z = PR$, and the size of its image is $\Delta Y = P'R'$.

When y is kept constant but z is changed by a small amount (Δz), the image position Y will change by ΔY. In the limit of $PR \to 0$, the ratio

$$\lim_{PR \to 0} \frac{P'R'}{PR}$$

is a constant, which shall be defined as the perspective foreshortening factor.

Definition 2. *Suppose a small object has coordinates* (x,y,z) *in 3D space and its image has coordinates* (X,Y) *in the image plane. The quantity*

$$M_{\perp} = \left| \frac{\partial Y}{\partial z} \right| \tag{7}$$

is called the ***perspective foreshortening factor*** *at depth z.*

The symbol $M_{\perp}$ is used because the depth direction is perpendicular to the image plane. The perspective foreshortening factor defined above is similar to the longitudinal

magnification of optical systems, but again there are no optics involved here; it is completely determined by the physical location (*x,y,z*) of the object.

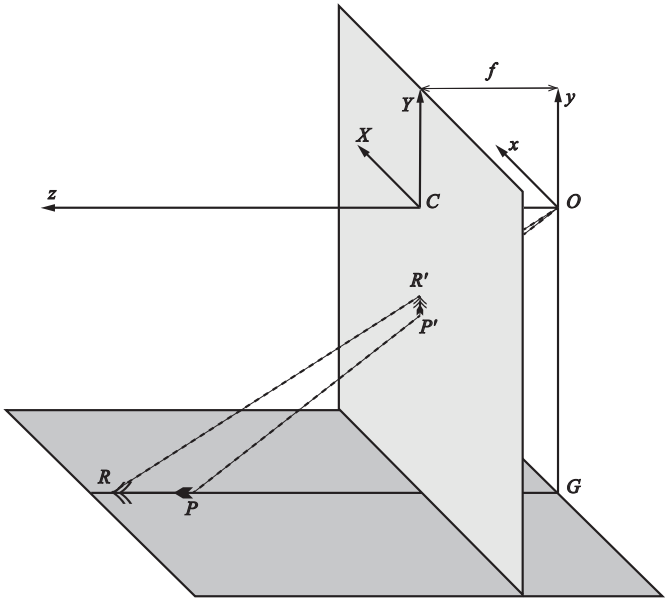

Figure 4. Perspective Foreshortening Factor

Theorem 2. *The perspective foreshortening factor* $M_{\perp}$ *of an object located at* (*x,y,z*) *is inversely proportional to the square of its depth z, but directly proportional to its vertical position* y, *as shown in Equation (8):*

$$M_{\perp} = \left| \frac{fy}{z^2} \right| \tag{8}$$

The proof is also straightforward by taking the partial derivative of *Y* with respect to *z* in Equation (2). The effect that the apparent size of an object in the depth direction diminishes according to the inverse square law in Equation (8) is called perspective foreshortening. The perspective foreshortening factor is also proportional to *y*. When *y* is smaller, $M_{\perp}$ is smaller, meaning that the foreshortening is more dramatic. Notice that *y*/*z* = tan *α*, where α = $\angle COP$ is the view angle of the segment *PR*. Equation (8) can also be written as

$$M_{\perp} = \left| \frac{f \tan \alpha}{z} \right| \tag{9}$$

This means that when *z* is fixed, the foreshortening factor is proportional to tan *α*. The closer the object is to the line of sight (*z*-axis), or the smaller the viewing angle *α* is, the more dramatic is the perspective foreshortening.

Similar to diminution, when the depth increases, the size of the image of object *PR* gets smaller as the effect of foreshortening. However, when the object *PR* is in the depth direction, the image diminishes, obeying an inverse square law, a rate much faster than diminution. The effect of foreshortening is more dramatic than diminution. Namely, the depth direction is shortened much faster than the transverse directions. When the depth is doubled, the apparent size of objects with transverse orientation shrinks to one half, while the apparent size of objects with longitudinal orientation shrinks to one quarter. This is also the reason that the photographs of 3D objects taken from different distances are not related by a similar transformation.

From Equation (8), when *z* is very small, $M_{\perp}$ and the image size can be very big, especially compared to the size of the objects in greater depth. Figure 5 shows two photographs of the foreshortening effect, where the length of the person is in the depth direction of the camera. The front part of the object (feet in the left picture, head in the right picture) is exaggeratedly magnified, while the far side is foreshortened dramatically. This effect is often associated with photographs shot with wide-angle lenses because one can shoot at very short subject distances with wide-angle lenses.

Quantitative Analysis of Perspective Distortion

Photographs are used in courtrooms and many other places as evidence. There is a saying "The camera does not lie." However, everyone has some experience of seeing quite different photographs of the same scene. Some photographs can be very misleading; they can cheat the eyes. For example, Figure 6 shows two photographs of the same scene. The depth perception from the two images is quite different. The foreground arch and pillars are about the same size in both photographs. Using this foreground as a reference, the arch and pillars in the background of Figure 6(a) look much smaller than those in Figure 6(b). This makes the background objects in Figure 6(a) look much farther away, while those in Figure 6(b) look much closer. The brick walkway in Figure 6(a) seems about twice as long as that in Figure 6 (b). This phenomenon is known as perspective distortion. They have the same cause as for perspective diminution and perspective foreshortening.

There is a common misconception held by some laypeople, including some photographers, about this perspective distortion: a wide-angle lens stretches distance, while a telephoto lens compresses distance. Some photographers have offered explanations: perspective distortion is not caused by the focal length of a camera, either wide angle or telephoto;

(a) **(b)**

Figure 5. Foreshortening Effects

rather, it is caused by subject distance (subject to camera distance). It is a coincidence that wide-angle lenses are often used for short subject distances, while telephoto lenses are often used for long subject distances. This explanation is correct. In fact, Figure 6(a) was taken with a wide-angle lens from five meters away. Figure 6(b) was taken with a telephoto lens from ten meters away.

Figure 7(a) is a duplicate of Figure 6(a), for easier comparison. If two photographs of the same scene are taken at the same position (same subject distance), using two different cameras, one telephoto and one wide angle, then the two photographs are related by a similar transformation. The objects appear bigger in the photograph shot with a telephoto lens but the field of view of the telephoto lens is smaller. Figures 6(b) and 7(b) were shot at the same position (10 meters); 6(b) with a telephoto lens and 7(b) with a wide-angle lens. It can easily be seen that Figure 6(b) is exactly the same as the central part of Figure 7(b) (in the rectangle) being cropped and enlarged. Telephoto lenses perform this cropping and enlargement mechanically and automatically.

In fact, resizing (proportionally enlarging or shrinking) of a photograph is the true culprit of perspective distortion. The pictures in Figures 5(a) and 5(b) are examples of perspective foreshortening. They are also examples of perspective distortion. The human body's proportion seems to be distorted in Figures 5(a) and 5(b). In Figure 5(a), the feet seem to be disproportionately big, the legs long and the head small. In Figure 5 (b), the head seems to be disproportionately big, while the legs are short and the feet are small.

Resizing of the photograph causes perspective distortion. If the major objects are oriented parallel to the image plane, resizing the photograph will not alter the proportion of the objects, but rather change the perception of distance – an enlarged picture causes a perception that the objects are closer, while a shrunken picture causes a perception that the objects are farther away. Also, resizing the image can alter the perception of spacing in depth direction between the objects. This is illustrated by comparing Figure 7(b) with Figure 6(b).

If the major objects are oriented along the depth direction of the lens, as in the case of Figures 5(a) and 5(b), resizing the pictures will cause the distortion of the relative size of the different parts of the same object along the depth direction. Figure 5(a) looks like a picture of a person with abnormal body proportions (extremely long legs). If fact, if the picture is enlarged enough, it does not seem to be abnormal any more. If the photographer looks with his own eyes at the model in the scene in Figure 5(a), when his eyes are very close to the feet of the model, the same position where the camera was placed when the photograph was shot, what he sees is the same as the enlarged photograph of Figure 5 (a). That is, if the human eye is placed at the same position as the camera, the eye sees exactly what the camera sees, which is the photograph. When the photograph is post-processed by shrinking it to a smaller size, as in Figure 5(a), the human brain interprets the model as being farther away. The human brain has been trained and has learned the laws of foreshortening factor $M_{\perp}$ in Equation (8) unconscious-

(a) Wide-Angle Lens, From a Short Distance (5 meters) **(b) Telephoto Lens, From a Long Distance (10 meters)**

Figure 6. Same Scene Shot with a Wide Angle Lens and a Telephoto Lens from Different Distances

(a) Wide-Angle Lens, From a Short Distance (5 meters) **(b) Wide-Angle Lens, From a Long Distance (10 meters)**

Figure 7. Same Scene Shot with the Same Lens (Wide Angle) from Different Distances

ly. When the foreshortening factor $M_{\perp}$ is applied to objects at larger depth, it results in an interpretation in the brain that the person is out of proportion and, hence, a perception of perspective distortion. Figures 5(a) and 5(b) are examples of perspective distortions caused by shrinking the images (taking close-up photographs with wide-angle lens, then shrinking the image), where distance in the depth direction appears to be longer than it actually is. Figure 6(b) is an example of perspective distortion caused by enlarging the image (taking far-away photographs, then enlarging the images), where distance in the depth direction (length of the walkway) appears to be shorter than it actually is. This enlargement can be done by cropping the central part of a wide-angle photograph (Figure 7b) and editing it with software, or by a telephoto lens mechanically and automatically at the time the picture is being shot (Figure 6b).

The perspective diminution factor and perspective foreshortening factor, which were defined earlier, will now be used to give a quantitative analysis of perspective distortion. The perspective foreshortening factor $M_{\perp}$ in Equation (8) is inversely proportional to z^2. $M_{\perp}$ is equal to the length of the image in the photograph corresponding to unit length in the depth direction in 3D space. The inverse of $M_{\perp}$,

$$\frac{1}{M_{\perp}} = \left| \frac{z^2}{fy} \right| \tag{10}$$

represents the real distance in depth in three dimensions corresponding to unit length measured on the photograph; for example, 1 mm. This is a magnifying process that our brains are trained for when interpreting the depth represented in photographs. This magnification is nonlinear in z. The closer to the center in the photograph (larger depth z), the greater this magnification is. Although the human brain does not use formulas to do the calculation, it is trained through experience. It uses relative size (transverse diminution, like height and width) as a depth cue to calculate depth subconsciously. When the photograph is enlarged, either manually or by a telephoto lens, the brain is cheated, thinking it is closer than it really is. The brain then uses this wrong distance to estimate the spacing in the depth dimension in space. As in the example from Figure 6(b), the photograph was shot with a telephoto lens; thus, the background objects are perceived as closer in depth than they actually are.

The telephoto lens works the same way as telescopes. They are all long focal length optical systems. The focal length of a telescope should be even longer (infinite in the ideal case). The only difference between a telephoto camera lens and a telescope is that a telephoto lens forms a real image on the image sensor, while a telescope forms a virtual image, which is observed by the eye. Some astronomical telescopes form real images and record the images as photographs, too. If you have the experience of watching a faraway person walking in the direction of the line of sight through a pair of binoculars, you should notice that although the person's arms and legs seem to be swinging, the person appears to be marking time without any apparent displacement in the depth direction. Often times, you are not able to see whether the person is facing you or away from you in binoculars. Because the depth does not seem to change, you cannot even tell whether the person is walking toward you or away from you. To explain this, look at how the diminution factor $M_{\parallel}$ changes with depth z in Equation (5). Taking the derivative of Equation (5) with respect to z, one can find

$$\frac{dM_{\parallel}}{dz} = -\frac{f}{z^2} \tag{11}$$

When z is very large, $dM_{\parallel} / dz$ is close to zero. This means that the height of the image of the person is almost constant when z changes. This also explains the two pictures of the same scene shot with a wide-angle lens and a telephoto lens from different distances, as in Figures 6(a) and 6(b). The distance Δz in 3D space between the foreground objects and background objects is the same in the two pictures. However, because the wide-angle photograph (Figure 6a) was shot at a closer distance (smaller z), the difference in image size between the foreground objects and the background objects is big (bigger $dM_{\parallel} / dz$), while in the photograph shot with the telephoto lens (Figure 6b), the difference in image size is smaller because of the larger depth z (smaller $dM_{\parallel} / dz$). Hence, Figure 6(b) gives the illusion that the walkway is shorter and the illusion that the telephoto lens compresses depth.

Conclusions

Perspective analysis and depth calculation and inference are very important in machine vision, unmanned vehicles and robotics. Precise definitions of perspective diminution factor and foreshortening factor were given in this paper. With these definitions, various perspective imaging situations and perspective distortions were analyzed. Applying perspective analysis in machine vision will be future research directions.

Image Credits

The drawing in Figure 1, by Jan Vredeman De Vries (1604), is in the public domain. The remaining photographs were taken by the author.

References

[1] Howard, I. (2012). *Perceiving in Depth, Volume 1: Basic Mechanisms*. Oxford University Press, New York.

[2] Mon-Williams, M., Tresilian, J. R., McIntosh, R. D., & Milner, A. D. (2001). Monocular and binocular distance cues: insights from visual form agnosia. *Experimental Brain Research*, *139*(2), 127-36.

[3] Schwartz, S. H. (2009). *Visual Perception*. (4th ed.). McGraw-Hill Medical.

[4] Beever, J. (2010). *Pavement Chalk Artist: The Three-Dimensional Drawings of Julian Beever*. Firefly Books.

[5] Forsyth, D., & Ponce, J. (2011). *Computer Vision: A Modern Approach*. (2nd ed.). Prentice Hall.

[6] Longfellow, W. P. P. (1901). *Applied Perspective for Architects and Painters*. Houghton Mifflin Company, The Riverside Press, Cambridge.

[7] Vredeman de Vries, J. (1968). *Perspective*. Dover Publications.

[8] Angel, E., & Shreiner, D. (2011). *Interactive Computer Graphics: A Top-down Approach with Shader-based OpenGL*. (6th ed.). Addison-Wesley.

[9] Thamma, R., Kesireddy, L.M., & Wang, H. (2012).

Centralized Vision-Based Controller for Unmanned Guided Vehicle Detection. *International Journal of Modern Engineering*, *12*(2), 58-65.

[10] Vargas-Clara, A., & Redkar, S. (2011). Dynamics of a Vertical Takeoff and Landing (VTOL) Unmanned Aerial Vehicle (UAV). *International Journal of Engineering Research Innovation*, *3*(1), 52-58.

[11] Eydgahi, A., Godaliyadda, D., & Falase, S. (2007). A Simulation Software for Autonomous Navigation of Unmanned Surface Vehicles Using MATLAB Environment. *International Journal of Modern Engineering*, *7*(2).

[12] Zhang, B., & Skaar, S.B. (2010). Laser-Assisted Uncalibrated Vision Guide Robotic De-palletizing. *International Journal of Engineering Research Innovation*, *2*(2), 17-24.

[13] Crankshaw, N. M. (1990). CARPA: Computer Aided Reverse Perspective Analysis. *APT Bulletin*, *22*(1-2), 117-129.

[14] Gao, X., Hou, X., Tang J., & Cheng, H. (2003). Complete Solution Classification for the Perspect-Three-Point Problem. *IEEE Trans PAMI*, *25*(8):930-943.

[15] Wu, B., Ooi, T. L., & He, Z. J. (2004). Perceiving Distance Accurately by a Directional Process of Integrating Ground Information. *Nature*, *428*(6978):73-77.

[16] Cao, Y., Xia, Y., & Wang, Z. (2010). A Close-Form Iterative Algorithm for Depth Inferring from a Single Image. *Proc. Perspectives in Neural Computing*, 729 -742.

[17] Saxena, A., Chung, S. H., & Ng, A. Y. (2005). Learning Depth from Single Monocular Images. *Neural Information Processing System*, *18*.

[18] Saxena, A., Sun, M., & Mg, A. Y. (2008). Make3d: Learning 3-d Scene Structure from a Single Still Image. *IEEE Tran. PAMI*, 31, 824-840.

[19] Saxena, A, Schulte, J., & Mg, A. Y. (2007). Depth Estimation Using Monocular and Stereo Cues. *International Joint Conference on Artificial Intelligence*.

[20] Biever, C. (2005). Why a robot is better with one eye than two. *New Scientist*, *188*(2530):30.

[21] Yu, S. X., Zhang H., & Malik, J. (2008). Inferring Spatial Layout form a Single Image via Depth-ordered Grouping. *Workshop on Perceptual Organization in Computer Vision*.

Biography

HONGYU GUO is an Assistant Professor of Computer Science at the University of Houston – Victoria. He received his Ph.D. degree in Computer Science from the University of Florida. His research interests are in computer graphics, computer vision, image processing and artificial intelligence. He can be reached at guoh@uhv.edu.

INSTRUCTIONS FOR AUTHORS: MANUSCRIPT REQUIREMENTS

The INTERNATIONAL JOURNAL OF MODERN ENGINEERING is an online/print publication, designed for Engineering, Engineering Technology, and Industrial Technology professionals. All submissions to this journal, submission of manuscripts, peer-reviews of submitted documents, requested editing changes, notification of acceptance or rejection, and final publication of accepted manuscripts will be handled electronically. The only exception is the submission of separate high-quality image files that are too large to send electronically.

All manuscript submissions must be prepared in Microsoft Word (.doc or .docx) and contain all figures, images and/or pictures embedded where you want them and appropriately captioned. Also, for all accepted manuscripts, each figure, image or picture that was imported into your Word document must be saved individually as a **300dpi or higher JPEG (.jpg)** file and submitted separately; your manuscript and figure numbers must be used in the title of the file (e.g., **M13-F-18 Figure 4**); that means one additional file for each image imported into your manuscript. These 300dpi images do NOT need to be embedded in your manuscript. For tables or graphs created directly in Word, you do not need to submit them as separate files.

Included below is a summary of the formatting instructions. You should, however, review the sample Word document on our website (www.ijme.us/formatting_guidelines) for details on how to correctly format your manuscript. The editorial staff reserves the right to edit and reformat any submitted document in order to meet publication standards of the journal.

The references included in the References section of your manuscript must follow APA-formatting guidelines. In order to help you, the sample Word document also includes numerous examples of how to format a variety of scenarios. Keep in mind that an incorrectly formatted manuscript will be returned to you, a delay that may cause it (if accepted) to be moved to a subsequent issue of the journal.

1. **Word Document Page Setup**: Two columns with ¼" spacing between columns; Top of page = ¾"; Bottom of page = 1" (from the top of the footer to bottom of page); Left margin = ¾"; Right margin = ¾".

2. **Paper Title**: Centered at the top of the first page with a 22-point Times New Roman (Bold), Small-Caps font.

3. **Page Breaks**: Do not use page breaks.

4. **Body Fonts**: Use 10-point Times New Roman (TNR) for body text throughout (1/8" paragraph indention); 9-point TNR for author names/affiliations under the paper title; 16-point TNR for major section titles; 14-point TNR for minor section titles; 9-point TNR BOLD for caption titles for tables and figures; other font sizes as noted in the sample document.

5. **In-text Referencing**: List and number each reference when referring to them in the body of your document (e.g., [1]). The first entry must be [1] followed by [2], [3], etc., continuing in numerical order to the final entry in your References section. Again, see the sample Word document for specifics. Do not use the End-Page Reference utility in Microsoft Word. You must manually place references in the body of the text.

6. **Tables and Figures**: Center all tables and figures. Captions for tables must be above the table, while captions for figures are below; all captions are left-justified.

7. **Page Limit**: Manuscripts should not be more than 15 pages (single-spaced, 2-column format).

8. **Page Numbering**: Do not use page numbers.

9. **Publication Charges:** Manuscripts accepted for publication are subject to mandatory publication charges.

10. **Copyright Agreement:** A Copyright Transfer Form must be signed and submitted by all authors on a given paper before that paper will be published.

11. **Submissions:** All manuscripts and associated files must be submitted electronically; the only exception would be if you wish to submit a CD with the individual files for your high-quality images, as noted above.

    MANUSCRIPTS should be submitted to Dr. Philip D. Weinsier, manuscript editor, at philipw@bgsu.edu along with a copy to editor@ijme.us.

    FILES containing your high-quality images should ONLY be submitted to philipw@bgsu.edu.

THE LEADING JOURNAL OF ENGINEERING, APPLIED SCIENCE, AND TECHNOLOGY

Print ISSN: 2157-8052
Online ISSN: 1930-6628

www.ijme.us

www.iajc.org

INTERNATIONAL JOURNAL OF MODERN ENGINEERING

ABOUT IJME:

- IJME was established in 2000 and is the first and official flagship journal of the International Association of Journal and Conferences (IAJC).
- IJME is a high-quality, independent journal steered by a distinguished board of directors and supported by an international review board representing many well-known universities, colleges and corporations in the U.S. and abroad.
- IJME has an impact factor of **1.63**, placing it among the top 100 engineering journals worldwide, and is the #1 visited engineering journal website (according to the National Science Digital Library).

OTHER IAJC JOURNALS:

- The International Journal of Engineering Research and Innovation (IJERI)
  For more information visit www.ijeri.org
- The Technology Interface International Journal (TIIJ).
  For more information visit www.tiij.org

IJME SUBMISSIONS:

- Manuscripts should be sent electronically to the manuscript editor, Dr. Philip Weinsier, at philipw@bgsu.edu.

  For submission guidelines visit
  www.ijme.us/submissions

TO JOIN THE REVIEW BOARD:

- Contact the chair of the International Review Board, Dr. Philip Weinsier, at philipw@bgsu.edu.

  For more information visit
  www.ijme.us/ijme_editorial.htm

INDEXING ORGANIZATIONS:

- IJME is currently indexed by 22 agencies. For a complete listing, please visit us at www.ijme.us.

Contact us:

Mark Rajai, Ph.D.

Editor-in-Chief
California State University-Northridge
College of Engineering and Computer Science
Room: JD 4510
Northridge, CA 91330
Office: (818) 677-5003
Email: mrajai@csun.edu

www.tiij.org

www.ijeri.org

IJME BEGINS ITS SECOND DECADE OF SERVICE

IJME IS THE OFFICAL AND FLAGSHIP JOURNAL OF THE INTERNATIONAL ASSOCATION OF JOURNALS AND CONFERENCE (IAJC)

www.iajc.org

The International Journal of Modern Engineering (IJME) is a highly-selective, peer-reviewed journal covering topics that appeal to a broad readership of various branches of engineering and related technologies. IJME is steered by the IAJC distinguished board of directors and is supported by an international review board consisting of prominent individuals representing many well-known universities, colleges, and corporations in the United States and abroad.

IJME Contact Information

General questions or inquiries about sponsorship of the journal should be directed to:

Mark Rajai, Ph.D.
Editor-in-Chief
Office: (818) 677-5003
Email: editor@ijme.us
Department of Manufacturing Systems Engineering & Management
California State University-Northridge
18111 Nordhoff St.
Northridge, CA 91330